THE STREAMING OF 1.3 - 2.3 MEV COSMIC-RAY PROTONS DURING PERIODS BETWEEN PROMPT SOLAR PARTICLE EVENTS

Thesis by

Francis E. Marshall

In Partial Fulfillment of the Requirements

for the Degree of

Doctor of Philosophy

California Institute of Technology

Pasadena, California

1977

(Submitted September 14, 1976)

ACKNOWLEDGMENTS

It is a pleasure to acknowledge the contributions of the many people who made this thesis possible. Invaluable contributions have been made by Dr. Edward Stone, both as principal investigator of the Caltech EIS experiment on IMP-7 and as my thesis advisor. The investment of his time and talents is deeply appreciated.

I am also grateful to Dr. Rochus Vogt for his interest in my work and his contributions to the experiment as co-investigator.

William Althouse, the project engineer, has made a substantial contribution to the successful operation of the EIS experiment.

This work has been greatly facilitated by previous studies using the IMP-7 experiment by Gordon Hurford, Dick Mewaldt, and Sol Vidor. Gordon also implemented the preliminary data analysis programs used for this work. Dick's comments during the course of this research and his knowledge of the experiment have been a great assistance. Contributions to this work by Dan Baker, Rick Cook, Alan Cummings, Tom Garrard, Steward Hartman, and Mark Wiedenbeck are gratefully acknowledged.

Much of this study uses data graciously provided by other experimenters. I am indebted to Drs. H. S. Bridge and J. D. Sullivan of the Massachusetts Institute of Technology for the solar wind data, to Dr. R. P. Lepping of the Goddard Space Flight Center for the magnetic field data used in a preliminary study, and to the National Space Science Data Center for the more comprehensive compilation of magnetic field data used in this thesis.

The excellent job of typing this thesis was done by Roberta Duffy.

I am grateful for the assistance provided by an N. D. E. A. Fellowship.

This research has been supported by the National Aeronautics and Space Administration under NAS 5-11066 and NGR 05-002-160.

ABSTRACT

The anisotropy of 1.3 - 2.3 MeV protons in interplanetary space has been measured using the Caltech Electron/Isotope Spectrometer aboard IMP-7 for 317 6-hour periods from 72/273 to 74/2. Periods dominated by prompt solar particle events are not included. The convective and diffusive anisotropies are determined from the observed anisotropy using concurrent solar wind speed measurements and observed energy spectra. The diffusive flow of particles is found to be typically toward the sun, indicating a positive radial gradient in the particle density. This anisotropy is inconsistent with previously proposed sources of low-energy proton increases seen at 1 AU which involve continual solar acceleration.

The typical properties of this new component of low-energy cosmic rays have been determined for this period which is near solar minimum. The particles have a median intensity of 0.06 protons/cm^2-sec-sr-MeV and a mean spectral index of -3.15. The amplitude of the diffusive anisotropy is approximately proportional to the solar wind speed. The rate at which particles are diffusing toward the sun is larger than the rate at which the solar wind is convecting the particles away from the sun. The 20 to 1 proton to alpha ratio typical of this new component has been reported by Mewaldt, et al. (1975b).

A propagation model with κ_{rr} assumed independent of radius and energy is used to show that the anisotropy could be due to increases similar to those found by McDonald, et al. (1975) at ~ 3 AU. The interplanetary Fermi-acceleration model proposed by Fisk

(1976) to explain the increases seen near 3 AU is not consistent with the $\sim$ 12 per cent diffusive anisotropy found.

The dependence of the diffusive anisotropy on various parameters is shown. A strong dependence of the direction of the diffusive anisotropy on the concurrently measured magnetic field direction is found, indicating a $\kappa_\perp$ less than $\kappa_\parallel$ to be typical for this large data set.

TABLE OF CONTENTS

I. INTRODUCTION

Observations of ~ 1 MeV protons in interplanetary space have revealed rich phenomena with the flux of these particles varying over many orders of magnitude and the time scales for these changes ranging from hours to days. It is to investigate the source of these particles and their variations that the present study has been undertaken.

McCracken and Rao (1970) have reviewed the observed characteristics of these particles. The authors group individual increases, or events, into two classes -- prompt events and delayed events. Prompt events, sometimes referred to as "classical" solar particle flares, have several distinct characteristics. They have short rise times, typically hours, and longer decay times, typically tens of hours. Velocity dispersion is observed during the onset of the event: the flux of higher velocity particles increases before the flux of lower velocity particles. The onset of the prompt event normally follows an enhancement of activity on the sun including optical flares, x-ray emission, and radio emission. A large directional dependence of the flux is observed early in these events with most of the particles streaming along the interplanetary magnetic field from the sun. These prompt events are generally thought to be due to nearly impulsive acceleration and injection of particles into the interplanetary medium by solar flares. Detailed studies of the anisotropies during prompt events have been done by McCracken, et al. (1971), Rao, et al. (1971), and Allum, et al. (1974). These studies have indicated the importance of anisotropy measurements for understanding

low-energy proton events. The present work will extend the work to periods between prompt events.

Increases that do not have the characteristics of prompt events have been termed delayed events by McCracken and Rao. These events typically have a longer rise time than prompt events, and no velocity dispersion is observed. Delayed events are also smaller than the larger prompt events.

Some delayed events occur during the decay phase of prompt events (Rao, et al, 1967a ; Lin, et al., 1968). The present work is restricted to periods between prompt solar events, so such delayed events are not included.

Other delayed events are not so clearly associated with prompt events. Bryant, et al. (1965) found events lasting several days that recurred every 27 days (one solar rotation period) for 7 successive solar rotations. The low-energy threshold was 3 MeV. These events were pictured as approximately steady-state streams of particles co-rotating with the sun, whose observed time development was caused by their rotation past the observer.

Periods of $\sim$ 1 MeV proton enhancements lasting $\sim$ 10 days have been reported by Fan, et al. (1968). Anisotropies were reported for two periods of $\sim$ 6 hours each, and the streaming was found to be coming from the sun's direction. These enhancements were interpreted as evidence of continual acceleration, near-sun storage in regions extending $\sim 180^{\circ}$ in solar longitude, and gradual injection into the interplanetary medium.

Anderson (1969) reported events not associated with prompt events similar to those found by Rao, et al. (1967a) during the decay of prompt events. Anderson proposed that these events were co-rotating with the sun and the particles were escaping from a storage region near the sun.

Further analysis of the events reported by Bryant, et al. (1965) was done by McDonald and Desai (1971) , who interpreted the events in terms of storage near the sun. An upper limit of 20 per cent was put on possible anisotropies.

Complex variations in the flux of protons at energies ≥ 0.3 MeV were reported by Krimigis, et al. (1971) with large ($\gtrsim 50$ per cent) anisotropies, indicating essentially continuous flow of particles from the sun. Roelof and Krimigis (1973) modelled these observations as scatter-free propagation from the sun to the earth with the variations caused by either connection to different regions on the sun or time variations in the rate of injection.

Although the delayed events discussed above have varied time developments, the models used to explain them are similar in many ways. Instead of the nearly impulsive acceleration and injection found in prompt events, the delayed events have been pictured as resulting from either continuous acceleration and injection or intermittent acceleration and storage between the sun and the earth. Thus, the sun is viewed as a continuing source of low-energy protons even during periods when prompt events are not observed. Anisotropies consistent with this solar source have been measured for some events, as indicated above.

A more comprehensive study that also suggested continuous acceleration was reported by Kinsey (1970), who examined proton fluxes in the energy interval 4 - 80 MeV during the time interval 24 May 1967 to 20 August 1968 and found a highly variable component at low energies. He suggested this component is due to a continuous, but variable, solar source. Thus, the sun is seen as a continuous source of particles whose flux is occasionally large enough to be observed as individual events.

The above observations present a rather consistent view, but there are two observations which do not fit. Rao, et al. (1967b), reported a nearly zero anisotropy for protons in the energy interval 7.5 - 45 MeV during extended periods of 1965 and 1966 when no events were observed. As discussed by Forman and Gleeson (1975), this result is difficult to interpret using contemporary propagation theory.

A recent observation by McDonald, et al. (1975) indicates the existence of at least some periods when flow back toward the sun might be expected. They report that larger delayed events were seen by Pioneer 11 between 2 and 5 AU than seen at earth during the same period. These events were interpreted as co-rotating streams populated by interplanetary acceleration of energetic particles.

The present study will report the observed anisotropy of 1.3 to 2.3 MeV protons during 317 6-hour periods for a time span from 72/273 to 74/2, omitting periods when prompt events are observed. The data will be interpreted in light of simultaneous measurements of the solar wind speed and the interplanetary magnetic field direction

using the propagation theory presented in Chapter II. These observations directly test the models discussed above that propose that the enhancements of the low-energy proton flux seen at 1 AU are caused by quasi-continuous injection of particles by the sun.

The present study differs from those discussed above in combining the following features. First, many periods from a long time span are used. Previous studies have typically been of a few events selected by the investigator. Second, for each period the anisotropy due to the effect of the solar wind has been subtracted from the observed anisotropy, leaving the anisotropy due to diffusion. For the first time, the dependence of this diffusive anisotropy on such parameters as the magnetic field direction is directly determined. Third, the background of the Caltech instrument makes a negligible contribution to the results reported in this work. Figure I-1 compares the fluxes used in the works cited above to those used in the present study. Because the observations have been taken at somewhat different energies, the differential flux at 1 MeV indicated by the observations has been used. An energy spectrum of $dj/dT = kT^{-3}$, where j is the differential intensity and T is the kinetic energy, typical of spectra observed at energies near 1 MeV, has been assumed for calculating the differential flux. Some of the previous studies were at fluxes much higher than those used in the current study. In addition, the quiet-time anisotropy measurement by Rao, et al. (1967b) is seen to have a higher equivalent flux than some of the periods used in this work. Thus, the current measurements are relevant to understanding this previous result.

Figure I-1

A comparison of proton fluxes for delayed events and quiet times for various experiments. The references for the designated experiments are:

UTD-1	Rao, et al., (1967a).
UCB-1	Lin, et al., (1968).
GSFC-1	Bryant, et al., (1965); McDonald and Desai (1971).
Chicago	Fan, et al., (1968).
UCB-2	Anderson, (1969).
JHU/APL	Krimigis, et al., (1971).
GSFC-2	Kinsey, (1970).
UTD-2	Rao, et al. (1967b).
Caltech	present work.

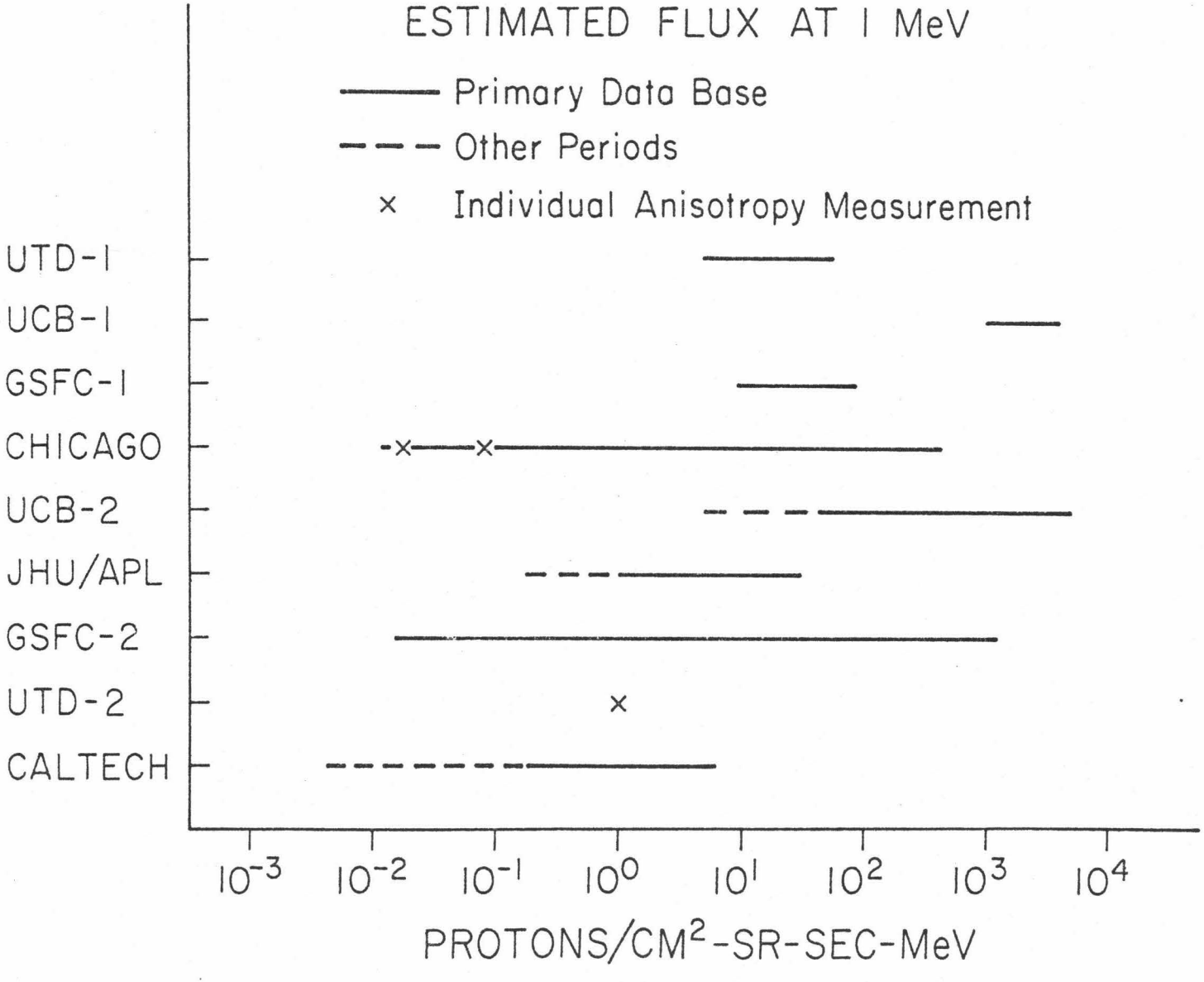
ESTIMATED FLUX AT 1 MeV
Primary Data Base
Other Periods
Individual Anisotropy Measurement
UTD-1
UCB-1
GSFC-1
CHICAGO
UCB-2
JHU/APL
GSFC-2
UTD-2
CALTECH
10^{-3}
10^{-2}
10^{-1}
10^{0}
10^{1}
10^{2}
10^{3}
10^{4}
PROTONS/CM^2-SR-SEC-MeV

II. EXPERIMENT

A. Spacecraft

The energetic particle data used in this study were obtained from the Caltech Electron/Isotope Spectrometer (EIS) experiment aboard the IMP-7 spacecraft. IMP-7 was launched into an orbit ranging from 32 to 36 earth radii in September, 1972. The orbit is inclined to the ecliptic by 28°. A rotation of this orbit into the ecliptic plane is shown in Figure II-1, along with the average position of the earth's magnetosphere (Behannon, 1968). The satellite is sunward of the earth's bow shock during the majority of its orbit. The spacecraft is spin stabilized with a rotation rate of ~ 45 rpm. The spin axis is within 2° of the South Ecliptic Pole; the Caltech EIS experiment is mounted so that it scans the ecliptic plane as the satellite rotates. Signals are generated by the spacecraft to indicate the current orientation of the satellite. Each rotation is divided into eight equal sectors as shown in Figure II-2. The signal for Sector 0 is initiated by the spacecraft's sun sensor detecting the sun. Because of the position of the Caltech experiment relative to the sun sensor, the Caltech experiment is not viewing the sun during Sector 0. The signals for Sectors 1 through 7 are determined by counting clock pulses after the sun-sensor pulse. The rate of the clock pulses is adjusted by the spacecraft so that the 8 sector signals are of equal length and include the entire rotation. Tests of the accuracy of the sectoring system are described in Chapter IV.

B. Instrument

A brief description of the aspects of the Caltech experiment

Figure II-1

The orbit of IMP-7 rotated into the ecliptic plane. Also shown are the average positions of the earth's bow shock and magnetopause as determined by Behannon (1968).

IMP-7 ORBIT

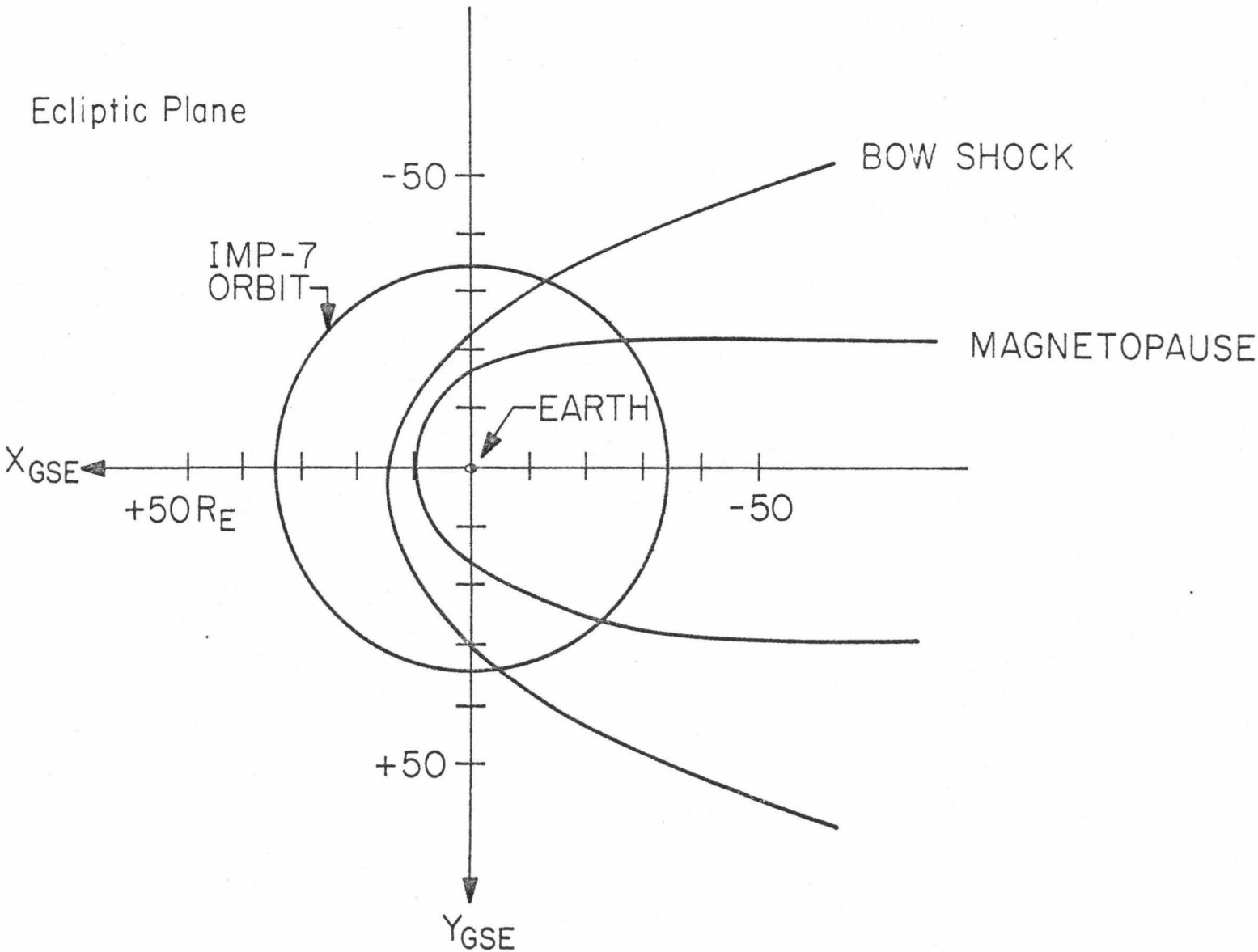
Ecliptic Plane
-50
BOW SHOCK
IMP-7
ORBIT
MAGNETOPAUSE
EARTH
X_{GSE}
+50 R_E
-50
+50
Y_{GSE}

Figure II-2

Diagram of the IMP-7 satellite as seen from the North Ecliptic Pole. The relative positions of the spacecraft sun sensor and the Caltech Electron/Isotope Spectrometer are shown. The average viewing angle is given for each of the 8 sectors.

IMP-7 SECTORING

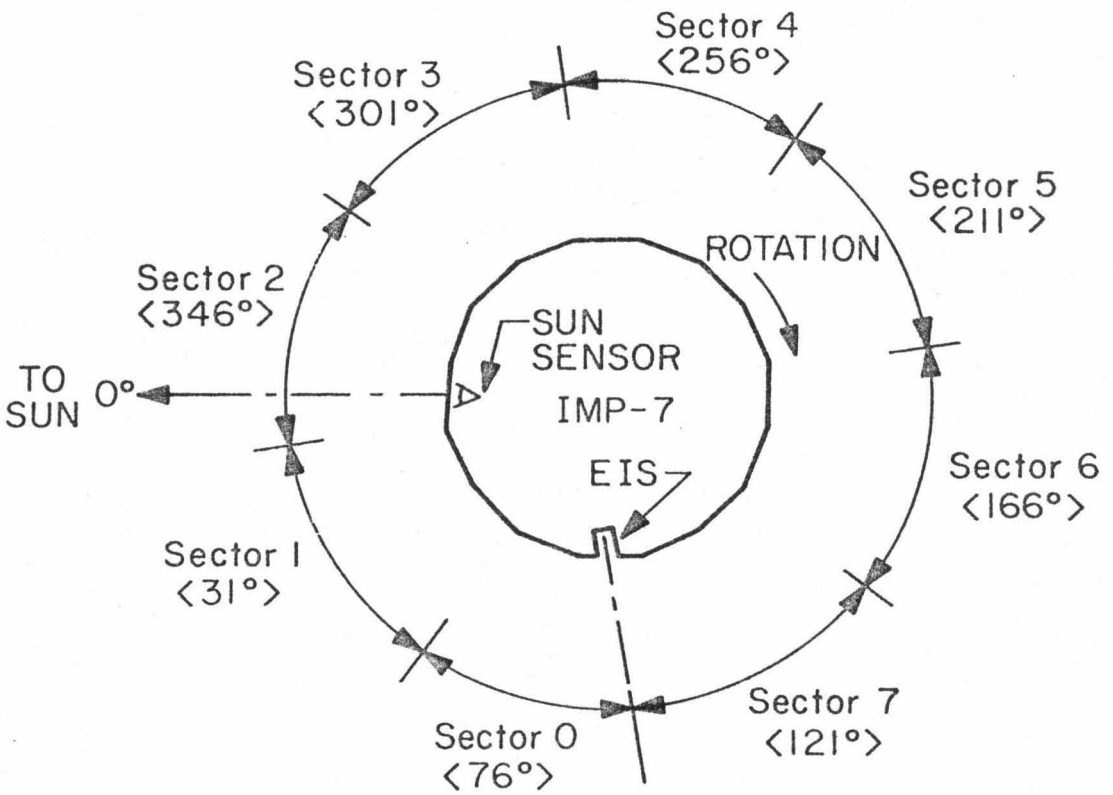

Solar Ecliptic Coordinate System

relevant to the current study is given here; more complete descriptions are available elsewhere (Hurford, et al., 1974; Mewaldt, et al., 1975a). A cross section of the Caltech EIS telescope on IMP-7 is shown in Figure II-3. The telescope consists of 11 fully-depleted silicon surface-barrier solid-state detectors and an anti-coincidence scintillator viewed by a photomultiplier tube. Each of the solid-state detectors except D10 has a pulse height analyzer and discriminator; D10 has only a discriminator. The solid-state detectors are all nominally 1000 microns thick with the exception of the 47 micron thick D2. The telescope is covered with a 2.4 mg/cm^2 aluminized mylar window.

The instrument has several modes of analysis. The data used in this work come from the narrow geometry mode in which detectors D0, D1, D3, D4, D10, and D11 are in anti-coincidence. An example of a narrow geometry signature is an event for which only D2 triggers. This work is concerned primarily with events of this signature, which have a geometric factor of 0.21 ± 0.01 cm^2-sr and an opening half-angle of $29^\circ \pm 1^\circ$ (Hartman, 1973).

Due to the limited telemetry rate available to the experiment, only part of the information produced by the particles which trigger the telescope is transmitted to earth and thus recorded. A more detailed description of the Caltech experiment is available elsewhere (Garrard, 1974). There are two types of transmitted information of interest to this work -- rate information and analyzed event information.

The rate information consists of the rates at which individual

Figure II-3

Cross Section of the IMP-7 Electron/Isotope Spectrometer Telescope.

IMP-7
CALTECH ELECTRON/ISOTOPE SPECTROMETER

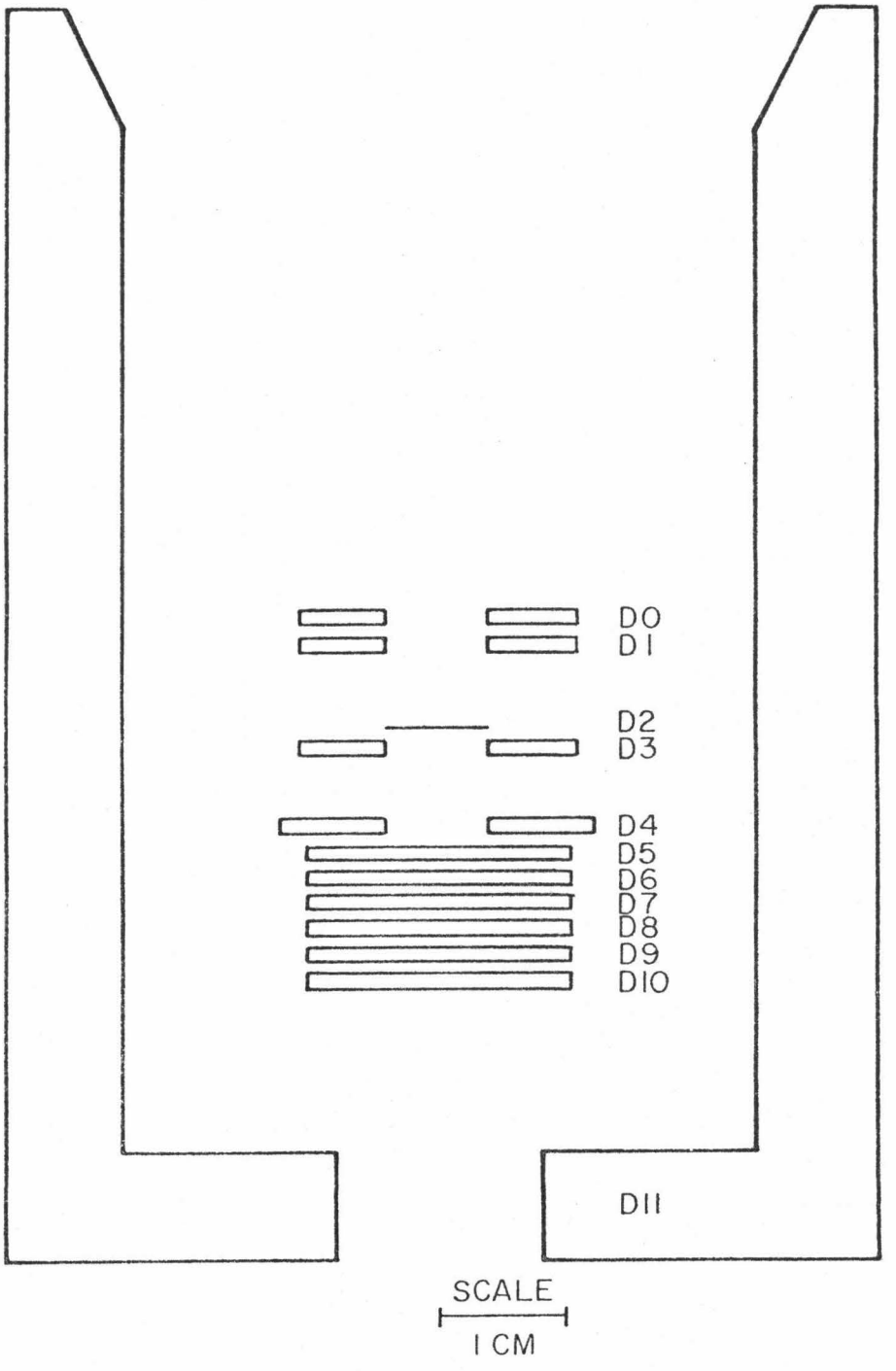

detectors trigger and selected combinations of detectors trigger. Table II-1 lists the available combinations and their mnemonics. The rates are determined by counting events for a known time interval; this accumulation is done in the satellite external to the Caltech experiment. The accumulation system and the Caltech experiment are connected by 9 rate lines labelled A, B, C, E, F1, F2, F3, F4, and F5. There are four states of this system, called subcommutation states, each lasting 20.48 seconds. During each state a selected set of 9 rates is accumulated. Table II-2 indicates which rates are accumulated during the four subcommutation states. The A, B, C, and E rates are accumulated separately for each of the 8 sectors using 4 sets of 8 accumulators. These rates are accumulated for only 14 spacecraft rotations ($\sim$ 18 seconds) out of the 20.48 seconds of the subcommutation state to insure that only complete rotations are used. The rotation period is measured so that the accumulation time is a known, but slowly varying, quantity. Because events are accumulated by sectors, anisotropies can be computed for these rates. An example of a sectored rate is PLO, which uses rate line A and is accumulated during subcommutation states 1 and 3. The PLO rate shares the accumulators associated with rate line A with the ELO rate. The remaining rate lines F1, F2, F3, F4, and F5 are not accumulated by sectors, and so require a total of 5 accumulators. Rates using these lines are accumulated continuously. The rates associated with lines F1 and F2 are read out twice every subcommutation state; the rates associated with lines F3, F4, and F5 are read out four times every subcommutation state.

Table II-1. Rates

Rate	Logic Requirement	Nominal Physical Significance
ELO	$N \cdot S \cdot \overline{d2h} \cdot D5 \cdot \overline{d5h} \cdot \overline{d6} \cdot \overline{d7} \cdot \overline{aip}$	Electrons, ∿0.2 to ∿1 MeV, including Compton recoils
EHI	$N \cdot S \cdot \overline{d2} \cdot D5 \cdot \overline{d5h} \cdot D6$	Electrons, ∿1 to ∿3 MeV, including Compton recoils
PLO	$N \cdot S \cdot D2H \cdot \overline{d5} \cdot \overline{d6} \cdot \overline{d7} \cdot \overline{aip}$	Nuclei, 1.2 to 2.4 MeV†
PHI	$N \cdot S \cdot D2 \cdot D5H \cdot \overline{d6}$	Nuclei, 4 to 13 MeV
D0*	$D0 \cdot S$	Electrons, ∿0.16 to ∿5 MeV, plus nuclei, 1 to 43 MeV
D01*	$D0 \cdot D1 \cdot S$	Electrons, ∿1 to ∿5 MeV, plus nuclei, 13 to 43 MeV
PEN	$N \cdot D5 \cdot D6 \cdot D10 \cdot \overline{d11}$	Electrons and nuclei that penetrate the telescope (electrons > 3 MeV, nuclei > 30 MeV)
NEUT	$N \cdot S \cdot \overline{d5} \cdot D7$	Neutral particles, such as γ-rays, whose Compton recoil electrons are detected in D7
ADC	D0+D1+...+D9	The logical OR of all pulse-height-analyzed detectors
HAZ		The rate at which the HAZARD flag is set
D0,D1,,,D11		Singles rates for individual detectors

$N = \overline{d0} \cdot \overline{d1} \cdot \overline{d3} \cdot \overline{d4}$

$S = \overline{d10} \cdot \overline{d11}$

AIP = analysis in progress

†Nuclei energy limits are for protons.

Table II-2. IMP-7 Rate Block

SCS	A	B	C	E	F1	F2	F3	F4	F5
1	ELO	PHI	D0	ADC	D1	D3	D4	NEUT	D0
2	PLO	EHI	D0*	D01*	D6	D7	D10	NEUT	D0*
3	ELO	PHI	D5	D11	D8	D9	D5H	NEUT	D5
4	PLO	EHI	D2H	PEN	HAZ	D2	D10	NEUT	D2H

The other type of information transmitted consists of analyzed events. The information for each analyzed event includes which detectors triggered, the sector during which the event occurred, and two pulse heights giving energy-loss information. The pulse heights transmitted depend on the signature of the events; the D2 and D5 pulse heights are transmitted for D25 events, for example. The data from one analyzed event are transmitted every 0.64 seconds. The selection of events transmitted is determined by a 5-level priority system. The equations determining an event's priority are given in Table II-3. Only events of the two highest priorities, P0 and P1, are used in this study. These events nominally consist of narrow geometry electrons and nuclei. If the previous event read out was a narrow geometry electron, the highest priority is assigned to narrow geometry nucleons. Otherwise, the highest priority is assigned to narrow geometry electrons.

Thus, both the D2 analyzed events and the PLO rate are a sample of D2 events. The live time for the PLO rate is $\sim$ 50 per cent of the elapsed time because the PLO rate is accumulated during 2 of the 4 subcommutation states. The live time for D2 analyzed events depends on the rates of the different types of narrow geometry events. Typically at PLO rates $\lesssim$ 0.5/second, there are more D2 analyzed events than events counted for the PLO rate, while the converse is true at higher rates.

Table II-3. Priority Levels

$$P0 = N \cdot S \cdot \overline{dh} \cdot \{\overline{d2h} \cdot D5 \cdot \overline{d5h} \cdot \overline{re} + (D2H + D5H) \cdot RE\} + N \cdot \overline{d11} \cdot \overline{dh} \cdot D5 \cdot D10 \cdot RE$$

$$P1 = N \cdot S \cdot \overline{dh} \cdot \{\overline{d2h} \cdot D5 \cdot \overline{d5h} \cdot RE + (D2H + D5H) \cdot \overline{re}\} + N \cdot \overline{d11} \cdot \overline{dh} \cdot D5 \cdot D10 \cdot \overline{re}$$

$$P2 = S \cdot \overline{dh} \cdot (D0 + N \cdot \overline{d5} \cdot D7)$$

$$P3 = N \cdot \overline{dh} \cdot (D2H + D5) \cdot D11$$

$$P4 = N \cdot (D2H + D5) \cdot DH$$

where

$N = \overline{d0} \cdot \overline{d1} \cdot \overline{d3} \cdot \overline{d4}$

$S = \overline{d10} \cdot \overline{d11}$

DH = hazard bit

RE = recent electron bit

III. COSMIC-RAY PROPAGATION

A. Diffusion - Convection Model

The basic principles of cosmic-ray propagation have been reviewed by Jokipii (1971). Propagation is controlled by the interplanetary medium which is a highly conductive plasma expanding nearly radially outward from the sun. This solar wind has a bulk velocity of $\sim$ 300 - 600 km/sec and a flow direction within $\sim 5^{\circ}$ of radial. Imbedded in the plasma is the interplanetary magnetic field which is carried out from the sun by the solar wind. Due to the sun's rotation, the average field direction forms an Archimedian spiral. The average field direction at 1 AU is about 45° from radial. The magnitude of the magnetic field is $\sim 5 \times 10^{-5}$ gauss at 1 AU; a $1\frac{1}{2}$ MeV proton has a Larmor radius of 3.4×10^{9} cm or 2.3×10^{-4} AU in this field.

Individual measurements of the interplanetary magnetic field fluctuate from the mean value. These fluctuations cause the cosmic rays to scatter from simple helical motion. After many such scatterings, propagation can be described as diffusion with a diffusion tensor $\underline{\underline{\kappa}}$. Because of the presence of the magnetic field, diffusion is in general not isotropic. Assuming that there is no difference in the two directions perpendicular to the field, the diffusion tensor has the form

$$\kappa_{ij} = \begin{pmatrix} \kappa_{\perp} & -\kappa_{T} & 0 \\ \kappa_{T} & \kappa_{\perp} & 0 \\ 0 & 0 & \kappa_{\parallel} \end{pmatrix}$$

where the z-axis is taken to be parallel to the direction of the magnetic field. $\kappa_{\parallel}$ and $\kappa_{\perp}$ characterize diffusion parallel to and per-

pendicular to the magnetic field, respectively. κ_T describes the streaming produced by density gradients perpendicular to the magnetic field.

No generally accepted theory exists for computing $\underline{\underline{\kappa}}$ from observed properties of the interplanetary magnetic field. The quasi-linear approach used by Jokipii (1966) to determine $\underline{\underline{\kappa}}$ from observable statistical properties of the magnetic field requires certain simplifying assumptions whose validity has been questioned (Fisk, et al., 1974; Birmingham and Jones, 1975). The results do suggest that the important quantity is the amount of power in the fluctuations of the magnetic field at wavelengths comparable to the Larmor radius of the particle being scattered. This resonant scattering theory indicates that $\kappa_\perp$ would be much smaller than $\kappa_\parallel$ if it weren't for an additional term contributing to $\kappa_\perp$ that has been interpreted as being due to the random walk of the field lines (Jokipii and Parker, 1969). That is, neighboring field lines at the sun can be separated at 1 AU allowing, for example, solar flare particles to have a larger azimuthal extent at 1 AU than at the sun without any scattering perpendicular to the field lines taking place. The relative size of $\kappa_\perp$ and $\kappa_\parallel$ remains unresolved. Values of $\kappa_\perp / \kappa_\parallel$ ranging from 0 (Wibberenz, 1974) to ~ 1 (Jokipii, 1971) have been suggested.

B. Anisotropies

The following picture of particle propagation emerges. The ~ 1 MeV cosmic-ray protons execute helical motion about the average magnetic field as they are being convected outward from the sun with the field at the bulk velocity of the solar wind. In addition, the cosmic

rays are scattered by the irregularities in the magnetic field. Forman and Gleeson (1975) have shown that the differential streaming is given by

$$\vec{S} = C\vec{V}U - \underline{\underline{\kappa}} \cdot \nabla U \ , \qquad (3\text{-}1)$$

where U is the differential number density, $\vec{V}$ is the solar wind velocity, and C is the Compton - Getting factor

$$C = (2-\alpha\gamma)/3 \ , \qquad (3\text{-}2)$$

where $\alpha = (T+2mc^2)/(T+mc^2)$ and γ is the spectral index given by

$$\gamma = \partial \ell n \, j / \partial \ell n \, T \qquad (3\text{-}3)$$

where j is the differential intensity, $j = wU/4\pi$, and w is the particle velocity. For the low energy protons relevant to this study, $\alpha \cong 2$. The vector anisotropy is dimensionless and indicates the relative amount of streaming toward different directions. It is defined by

$$\vec{\xi}_{OBS} = 3\vec{S}/Uw = \frac{3}{w}\left[C\vec{V} - (\underline{\underline{\kappa}} \cdot \nabla U)/U\right] \equiv \vec{\xi}_{CON} + \vec{\xi}_{DIF} \ . \qquad (3\text{-}4)$$

The anisotropy is the sum of two terms, a convective term and a diffusive term. The convective term is proportional to the solar wind velocity and is related to the energy spectrum of particles through the Compton - Getting factor. The diffusive term is determined by the product of the diffusion tensor and spatial gradients in the particle density. Thus, to learn about the spatial distribution, the convective term must be subtracted from the observed anisotropy. The typical size of the convection term is $\sim$ 20 per cent.

The diffusion - convection model has been used by McCracken, et al. (1971) to explain the observed time development of the anisotropy during prompt solar particle events. As discussed in Chapter I,

the prompt event consists of particles injected nearly impulsively into the interplanetary medium which then propagate past 1 AU. Hence, early in the event there are large spatial gradients, and the diffusive term dominates the convective term as shown in Figure III-1a. The streaming is along the field line indicating $\kappa_\perp$ to be smaller than $\kappa_\parallel$. Later in the event, the solar wind has convected the peak of the particle distribution out to 1 AU so that the spatial gradients are small. At this time the convective term dominates the observed anisotropy as shown in Figure III-1b. Finally, many days into the event, the peak of the distribution is beyond 1 AU so that particles are diffusing back toward the sun, and the observed anisotropy is as shown in Figure III-1c.

Observations by Allum, et al. (1974) have raised questions about the role of the magnetic field in low-energy cosmic-ray propagation. The authors report that late in the development of prompt events the direction of the observed anisotropy is independent of the local magnetic field direction. This contrasts with the strong dependence of the observed anisotropy direction on the magnetic field direction early in prompt events found by McCracken, et al. (1968). The understanding of these two observations is an important problem for cosmic-ray propagation work.

The present work extends the study of particle anisotropy and its dependence on various plasma parameters to periods between prompt solar particle events. Equation (3-4) indicates what quantities are understood to affect the observed anisotropies. As discussed in Chapter IV, many of these quantities are available for the present

Figure III-1

The model for the evolution of the anisotropy during a prompt solar particle event. Early times are periods $\lesssim$ 1 day after the onset of the event, late times are periods from $\sim$1 to $\sim$4 days after then onset, and very late times are periods $\gtrsim$4 days after onset. The figure is adapted from McCracken, et al., (1971).

ANISOTROPY DURING PROMPT EVENT

a. Early Times

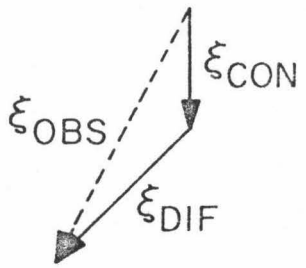

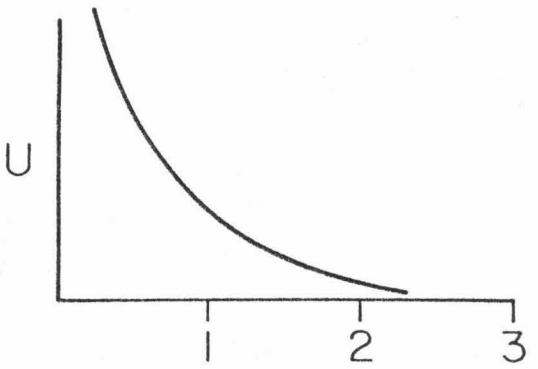

b. Late Times

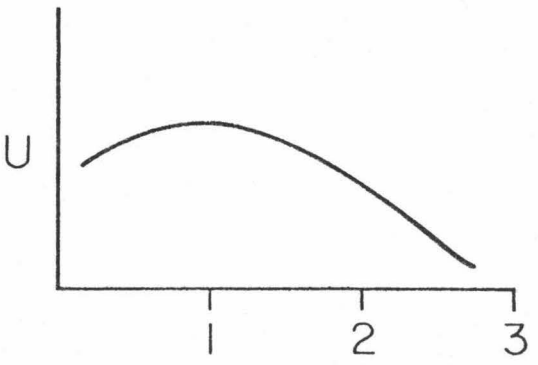

c. Very Late Times

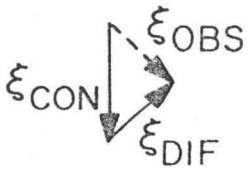

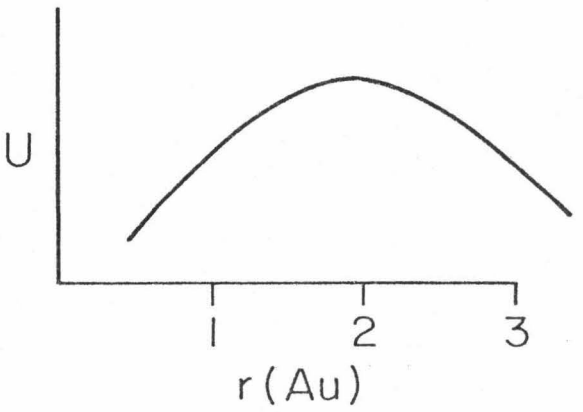

study. All the quantities affecting $\vec{\xi}_{CON}$ are known. This means $\vec{\xi}_{DIF}$ can be determined by subtracting $\vec{\xi}_{CON}$ from $\vec{\xi}_{OBS}$. The quantities in $\vec{\xi}_{DIF}$ are not as well known. Wibberenz (1974) has summarized the estimates of $\varkappa_{rr}$ determined from observed time-to-maximum-intensity for prompt solar events. A typical value for $\sim 1\frac{1}{2}$ MeV protons is 3×10^{20} cm^2/sec. Evidence of gradients sometimes as large as + 300 per cent/AU has been reported by McDonald, et al. (1975). Substituting these values into eq. (3-4) indicates diffusive anisotropies of $\sim$ 10 per cent toward the sun could be observed at least during certain periods.

IV. DATA ANALYSIS

A. Particle Selection

The anisotropy measurements are from the Caltech EIS experiment described in Chapter II. The anisotropies are computed using analyzed events which trigger only D2, which will be referred to as D2 analyzed events. Anisotropies using the PLO rate are used as a consistency check. The energy intervals of incident protons which produce the observations are:

	Nominal	73/86 - 73/154
D2 analyzed events	1.33 to 2.32 MeV	1.24 to 2.17 MeV
PLO	1.18 to 2.37 MeV	1.12 to 2.37 MeV

A change of $\sim$ 4 channels in the offset of the D2 pulse height analyzer lowered the nominal energies during the period 73/86 to 73/154. The upper limit for energy loss for D2 analyzed events is chosen to eliminate particles that lose too much energy in D2 to be protons. This limit eliminates $\sim$ 5 per cent of D2 events. An upper limit to the electron contribution to D2 events can be determined using the method presented by Lupton and Stone (1972) for determining electron detection efficiencies in solid-state detectors. The authors plot the maximum efficiency, that is, the efficiency at the incident electron energy at which the efficiency is highest, as a function of the energy threshold of a 50-micron detector. Using the energy threshold for D2 analyzed events, the maximum efficiency is $< 10^{-4}$ at all times. The flux of electrons is monitored by the ELO rate which has a geometric factor about one-fourth that for D2 events at incident electron energies $\sim \frac{1}{2}$ MeV. The ELO rate is $\lesssim$ 0.15/second for the periods used in this

study, so the electron contribution to D2 analyzed events is $\lesssim 4 \times 10^{-5}$/ second, or < 1 event in 6 hours. Thus, electron contributions to D2 analyzed events have essentially no effect on the computed anisotropies.

B. Anisotropy Determination

Anisotropies are computed from 6-hour averages of D2 analyzed events during the time interval 72/273 to 74/2. Six-hour averages are used to accumulate enough events so that statistical uncertainties will not be large compared to the measured anisotropy for a large fraction of the available periods. As shown in Figure IV-1, a typical PLO rate is ~ 0.02/second, which produces about 400 D2 analyzed events in 6 hours. An anisotropy measurement using 400 counts will have a statistical uncertainty of $\sim$ 7 per cent compared to a typical observed anisotropy of $\sim$ 10 per cent. The method used for calculating anisotropies and their statistical uncertainties is presented in detail in Appendix A; a brief account is given here.

The anisotropy is calculated by fitting in a least squares sense the observed number of counts by sector to the function:

$$f(\phi) = A + B \cos \phi + C \sin \phi \qquad (4\text{-}1)$$

The parameters of the fit A, B, and C are readily solved from linear equations. Anisotropies usually are expressed by an equivalent function, but one with different parameters:

$$f(\phi) = A_o(1 + \xi \cos(\phi - \phi_o)) \quad . \qquad (4\text{-}2)$$

A direct fit to this function leads to non-linear equations for the parameters. To avoid this, the parameters of eq. (4-2) are determined from the parameters fit to eq. (4-1). ξ is then multiplied by 1.079 to

Figure IV-1

The distribution of the 6-hour averages of the PLO rate observed by the Caltech EIS experiment aboard IMP-7. The flux of 1.2 to 2.4 MeV protons is computed by approximating the PLO rate as being due only to protons stopping in D2. Heavier nuclei and protons penetrating D2 typically produce $\sim$ 15% of the PLO rate.

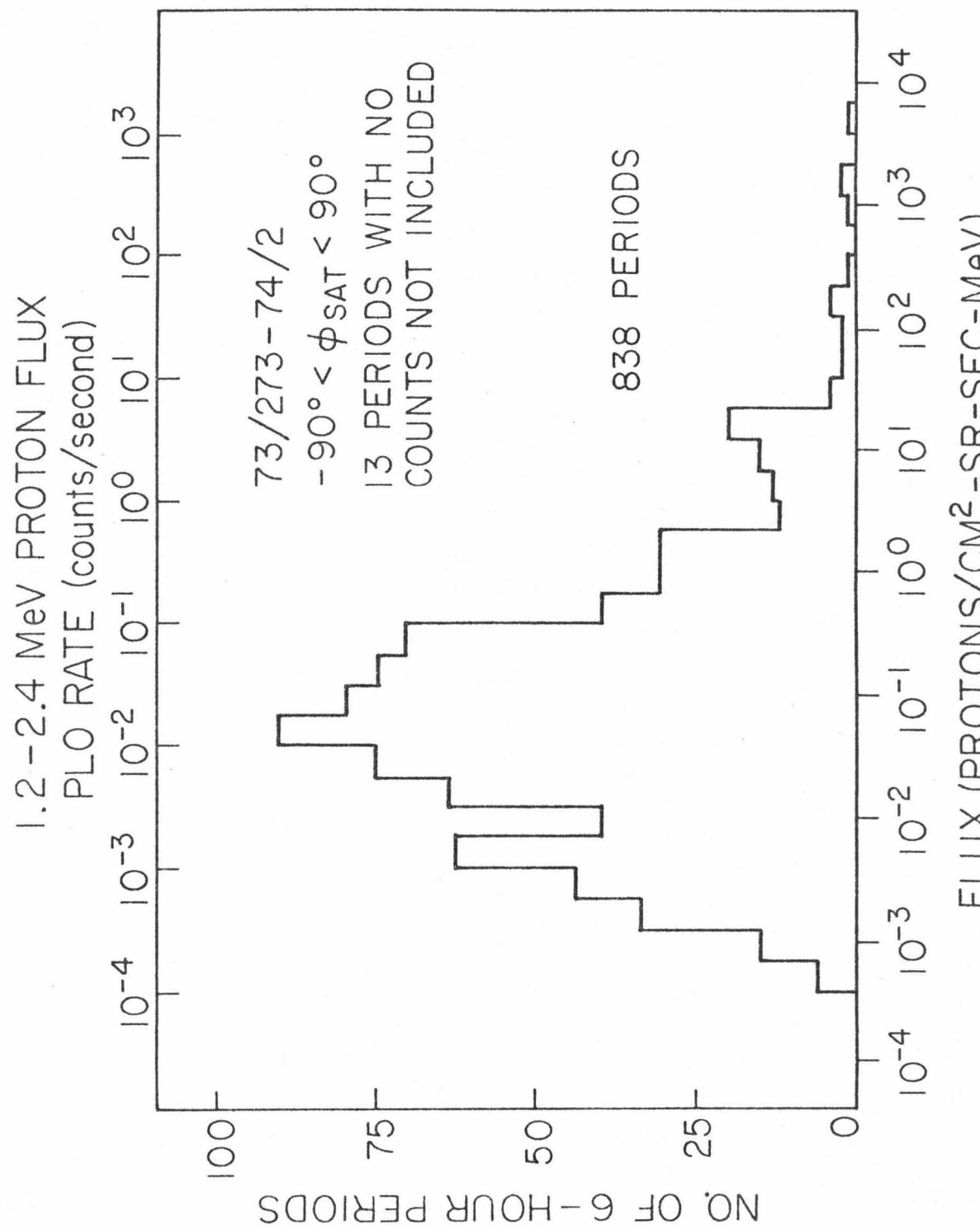
1.2-2.4 MeV PROTON FLUX
PLO RATE (counts/second)
73/273-74/2
-90° < ϕ_{SAT} < 90°
13 PERIODS WITH NO
COUNTS NOT INCLUDED
838 PERIODS
NO. OF 6-HOUR PERIODS
FLUX (PROTONS/CM^2-SR-SEC-MeV)

correct the smoothing effect due to the finite opening angle of the telescope and the finite number of sectors. Error bars on ξ and ϕ_o used in this work are defined by

$$\sigma_\xi = \frac{1.079}{2} \frac{\bar{\sigma}}{A_o} , \tag{4.3}$$

where $\bar{\sigma}$ is average uncertainty in counts in a sector,

$$\sigma_{\phi_o} = \frac{\sigma_\xi}{\xi} \cdot 57.296^o . \tag{4-4}$$

The determination of the probability distribution for the true value of ξ and ϕ_o given an observation is discussed in Appendix A. Let

$$z = \xi/\sigma_\xi .$$

For $z \gtrsim 2$, that is, for statistically significant observations, the probability distribution for the true ξ is approximately Gaussian, centered near the observed value with a standard deviation given by eq. (4-3). For $z \leq \sqrt{2}$, the most likely value of ξ is 0, and eq. (4-3) is only an estimate of the statistical uncertainty.

The observed ϕ_o is always the most likely value for the true ϕ_o. The σ_{ϕ_o} given in eq. (4-4) is the standard deviation of the probability distribution for the true ϕ_o in the limit of large z. For $z \lesssim 2$, σ_{ϕ_o} is only an indication of the uncertainty in the determination of ϕ_o.

For $\xi << 1$, eq. (4-2) describes a nearly isotropic distribution with a small anisotropy of amplitude ξ and a maximum flux observed when the telescope is pointing in the direction ϕ_o. The streaming direction ϕ_ξ is defined by

$$\phi_{\xi} = \phi_{o} + 180^{o} \quad .$$

The functional dependence given by eq. (4-2) is found to provide a good fit to nearly all the data used in this study. Define a goodness-of-fit parameter χ_{ν}^{2} using the data points y_i, their statistical uncertainties σ_i, and the fitting function $y(x_i)$ in the usual way:

$$\chi_{\nu}^{2} = [\sum_{i} (y_i - y(x_i))^2 / \sigma_i^2] / \nu \quad ,$$

where ν is the number of degrees of freedom. χ_{ν}^{2} is computed for each period. If the deviations of the observations from the fit are due only to statistical fluctuations, the mean χ_{ν}^{2} equals 1. Figure IV-2 presents the observed distribution of χ_{ν}^{2} and the distribution predicted due to statistical fluctuations. Periods when the PLO rate is larger than 0.3/second or smaller than 0.01/second, periods when the satellite is not on the sunward side of the earth, and periods near the beginning of prompt solar particle events are not included in the distribution. These periods are also not included in the final data set used in this study; the selection criteria for the final data set are discussed in Chapter V.

Both the observed and predicted distributions peak near 0.7 and fall to half maximum near 1.4, indicating eq. (4-2) provides a good fit to most of the periods. There are more periods with large χ_{ν}^{2} than predicted, but they comprise a small fraction of the total number of periods; only 3 per cent of the periods have $\chi_{\nu}^{2} \geq 4.0$. The mean χ_{ν}^{2} of 1.28 indicates that the average deviation from the fit is 1.13 times as large as that due to statistical fluctuations. Thus, deviations from the function fit to the observations are domi-

Figure IV-2

The distribution of the goodness-of-fit parameter χ^2_ν determined from the anisotropy fits to D2 analyzed events. The mean of this distribu- is indicated. The number of degrees of freedom ν for the fit is 5. The data set consists of periods from 72/273 to 74/2 when the average PLO rate is between 0.01/second and 0.3/second. In addition, the average longitude of the satellite in Geocentric Solar Ecliptic coordinates, ϕ_{SAT}, is required to be between -90^o and $+ 90^o$. Only periods for which the magnetic field B, the solar wind speed V, and spectral index γ are known are included in the data set. As discussed in the text, periods near the onset of identified prompt solar particle events are not included. Also shown is the distribution of χ^2_ν expected if the deviations from the anisotropy fits were due only to statistical fluctuations.

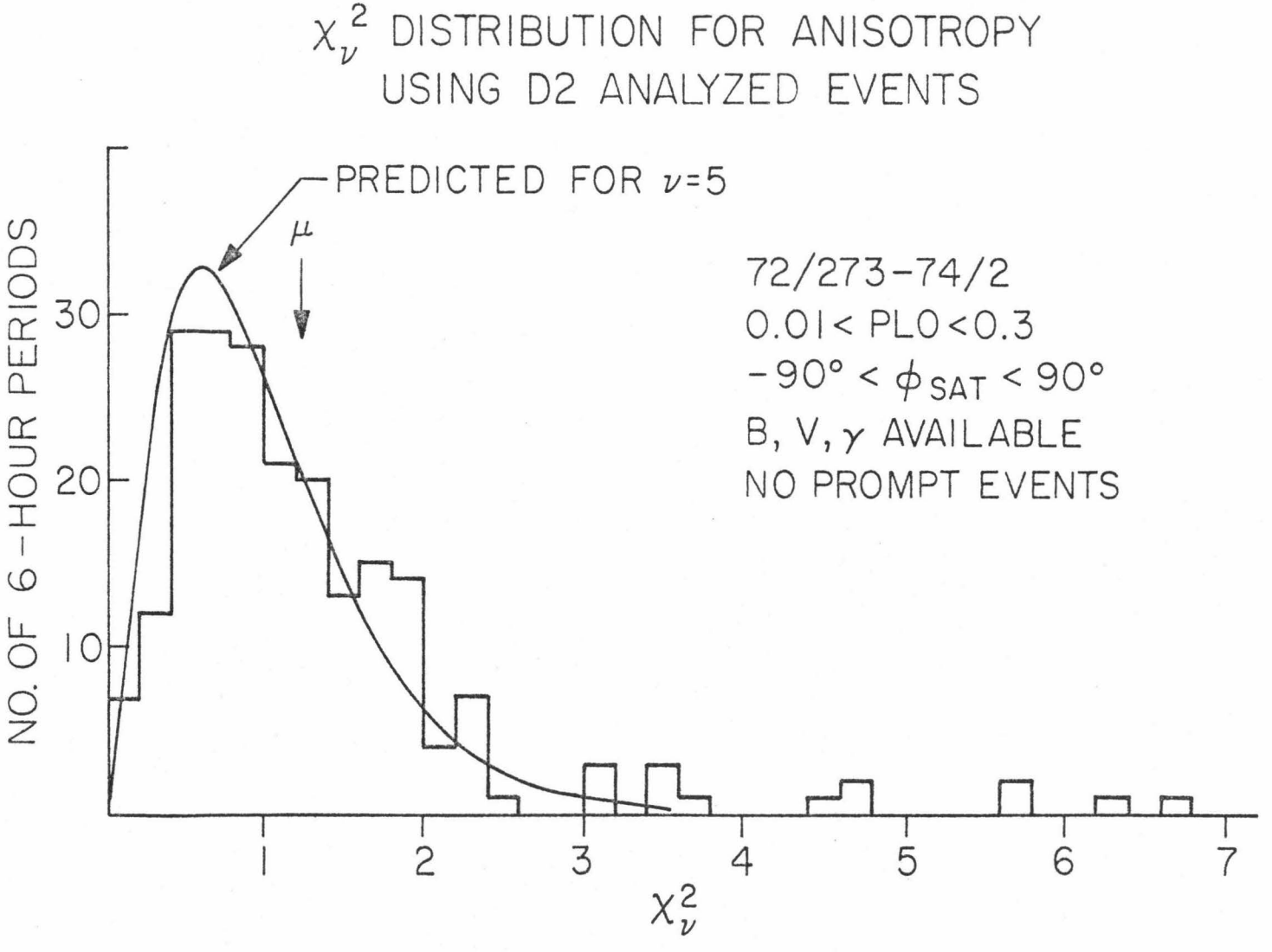
χ_ν^2 DISTRIBUTION FOR ANISOTROPY
USING D2 ANALYZED EVENTS
PREDICTED FOR ν=5
μ
72/273-74/2
0.01< PLO<0.3
$-90° < \phi_{SAT} < 90°$
B, V, γ AVAILABLE
NO PROMPT EVENTS
NO. OF 6-HOUR PERIODS
30
20
10
1
2
3
4
5
6
7
χ_ν^2

nated by statistical fluctuations due to the finite number of counts.

Tests have been made to determine that the sectoring system aboard IMP-7 is not malfunctioning and thereby introducing significant instrumental errors into the measured anisotropy. The first test uses background rates which are known to be nearly isotropic. As discussed by Hurford, et al. (1974), the ELO and EHI rates have a substantial background rate caused by gamma rays Compton scattering in the telescope and triggering D5 to simulate ELO events or D5 and D6 to simulate EHI events. During most of the time, this background rate is larger than the true electron rate as determined from D0 events. The gamma rays are produced by the interaction of relativistic cosmic-ray nucleons in the spacecraft. This process is largely independent of the spacecraft orientation, so the resultant ELO or EHI events are nearly isotropic. Consequently, if the instrument is working correctly, the anisotropy computed for these background rates should be nearly zero. Anisotropies are computed using data from 72/273 to 75/18, rejecting periods when the satellite is not sunward of the earth. Figure IV-3 has histograms of the ELO and EHI rates for this period. In order to avoid rates above background, ELO anisotropies include only periods when the ELO rate is less than 0.053/second, and EHI anisotropies include only periods when the EHI rate is less than 0.025/second. Periods near the beginning of prompt solar particle events are also excluded. The computed ELO anisotropy amplitude is consistent with 0 and is less than 0.67 per cent at a 95 per cent confidence level. The EHI anisotropy is also consistent with 0 and is less than 0.86 per cent at the 95 per cent

Figure IV-3

The distribution of the observed ELO and EHI rates. The arrows indicate the respective upper limits of rates for periods included in the calculation of the anisotropies of the backgrounds of ELO and EHI. There are 1599 periods in each panel.

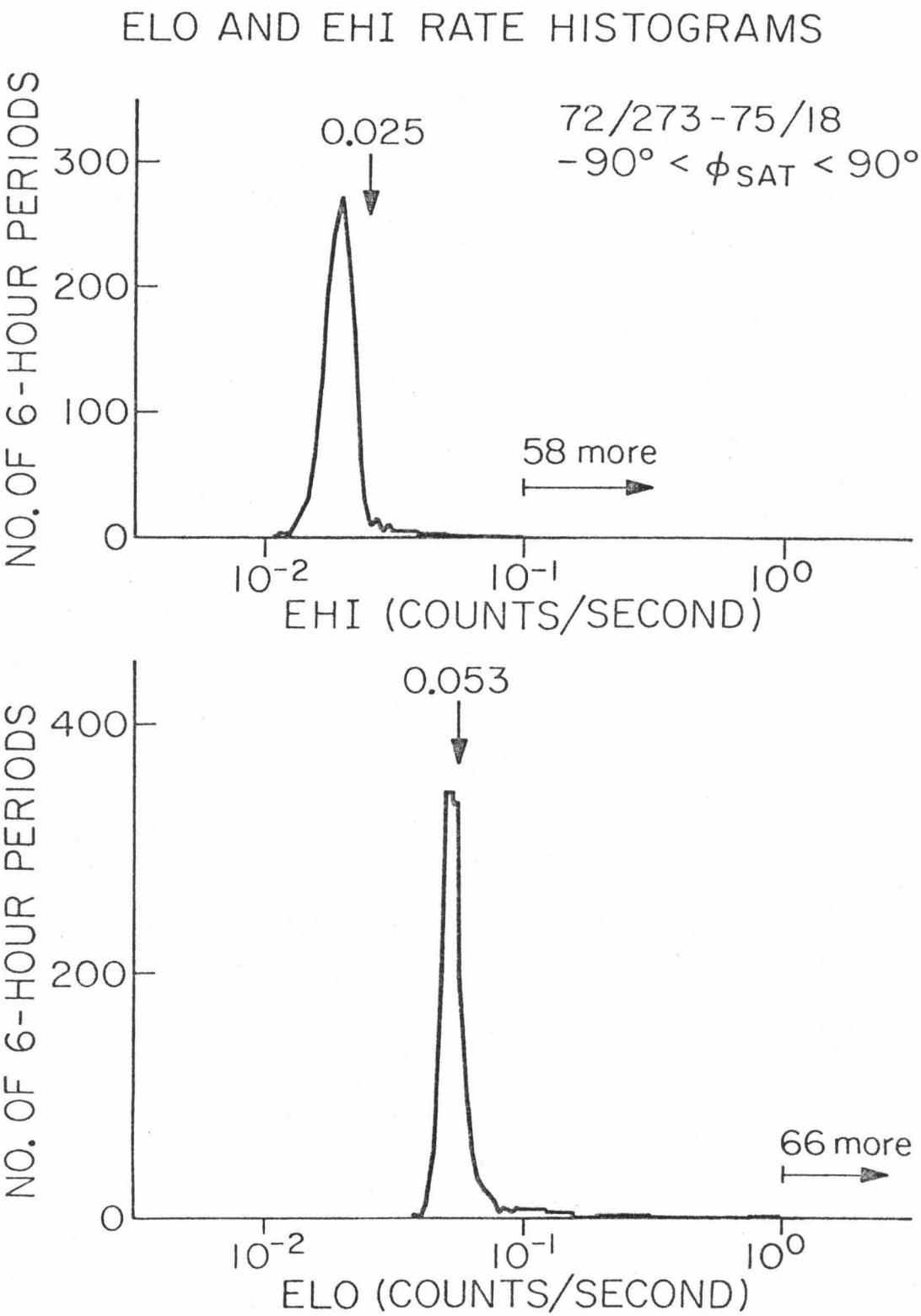
ELO AND EHI RATE HISTOGRAMS
72/273-75/18
-90° < φSAT < 90°
0.025
58 more
NO. OF 6-HOUR PERIODS
300
200
100
0
10-2
10-1
100
EHI (COUNTS/SECOND)
0.053
66 more
NO. OF 6-HOUR PERIODS
400
200
0
10-2
10-1
100
ELO (COUNTS/SECOND)

confidence level. Thus, any long-term bias affects these anisotropies by $\lesssim$ 1 per cent. As discussed in Chapter II, the rate accumulation system is shared by different rates through the use of 9 rate lines and 4 subcommutation states. Since ELO and PLO share the same rate line and EHI and PLO are accumulated during the same subcommutation states, any instrumental error in the PLO anisotropy should also be $\lesssim$ 1 per cent.

Although no large instrumental errors were found in the anisotropies using rate data, the instrument might introduce errors into the anisotropies of analyzed events. To check this, the second test compares the anisotropy for D2 analyzed events to the anisotropy for the PLO rate. As explained in Section A, these two event types are samples of D2 events with slightly different energy intervals. Thus, the two event types should measure approximately the same anisotropy if the instrument is functioning properly (except at high rates -- see Chapter V). The difference vector, $\vec{\xi}_{\mathrm{PLO,\,DIF}} - \vec{\xi}_{\mathrm{D2,\,DIF}}$, is plotted in Figure IV-4 for 6-hour periods when the PLO rate is between 0.03/second and 0.3 second, and the satellite is sunward of the earth. Periods near the beginning of prompt solar events have not been included. The mean differences in the x- and y-directions are -0.3 per cent and 0.5 per cent, respectively, with a statistical uncertainty of $\pm$ 0.5 per cent. The average particle velocity for D2 analyzed events is $\sim$ 1.04 times larger than the average velocity for PLO events. Thus, depending on how the spatial gradients and the diffusion coefficient vary with energy, there may be a systematic ratio between the anisotropies of $\sim$ 1.04; for a typical diffu-

Figure IV-4

The difference in $\vec{\xi}_{DIF}$ determined using the sectored PLO rate and $\vec{\xi}_{DIF}$ determined using D2 analyzed events. Each dot indicates one 6-hour period. A typical 1 σ error bar is indicated.

$\vec{\xi}_{PLO,\,DIFFUSIVE} - \vec{\xi}_{D2,\,DIFFUSIVE}$

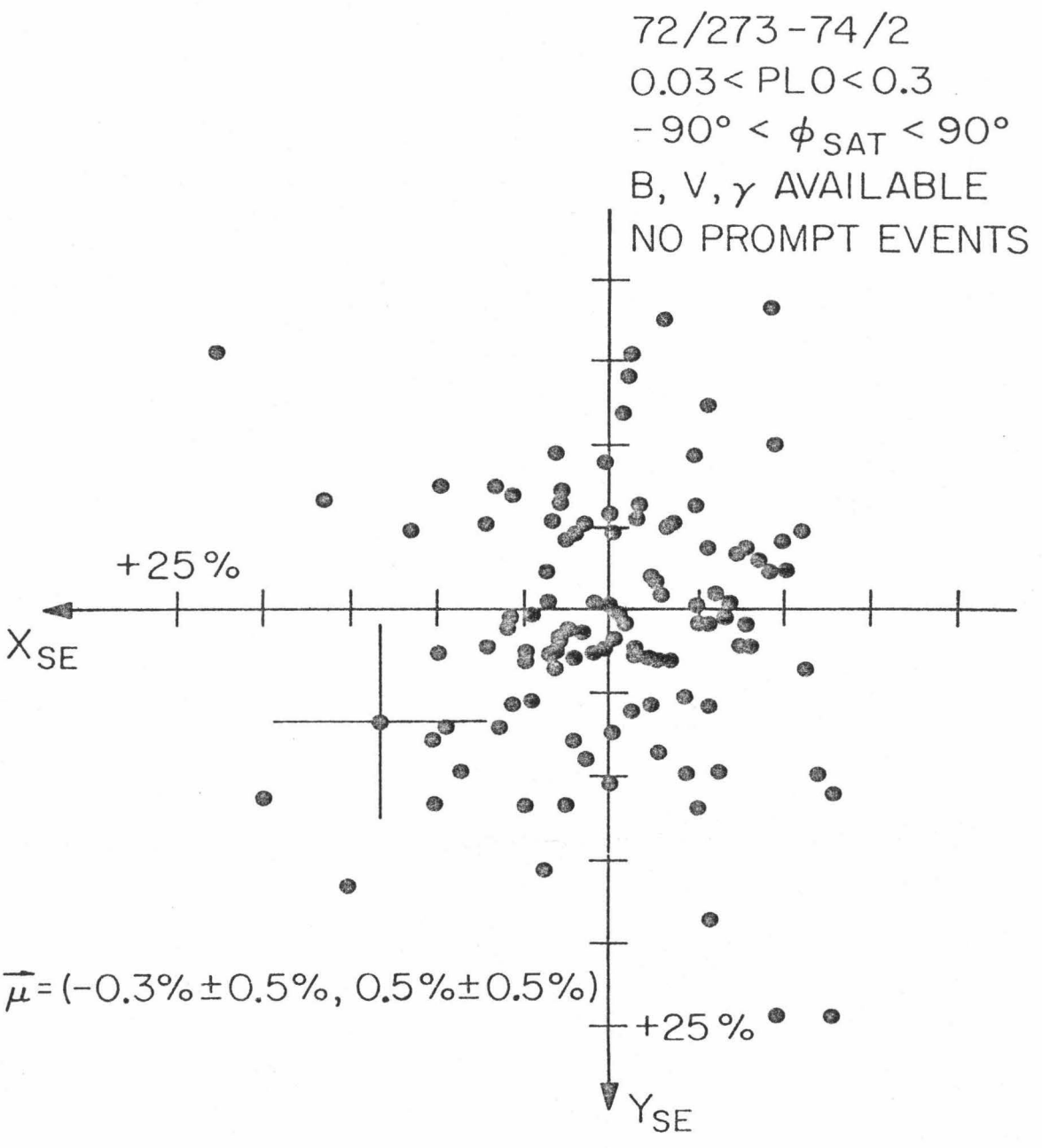

sive anisotropy of $\sim$ 15 per cent, this is a systematic error of $\sim$ 0.6 per cent -- comparable to the statistical uncertainties. The small mean differences found are consistent with no instrumental bias between the anisotropies of analyzed events and rates.

The two tests together indicate instrumental errors in the anisotropy of D2 analyzed events are $\lesssim$ 1 per cent.

As discussed above, the ELO rate is dominated by an isotropic background much of the time, producing a measured anisotropy insensitive to the true electron anisotropy. In contrast, D2 events are comparatively free of such background. During days 66 to 70, 1973, the average PLO rate was $3.5 \pm 0.4 \times 10^{-4}$/second, placing an upper limit on the background rate. This rate is $\sim$ 1 count/sector/6-hour period. The typical PLO rate limits for periods used in this study are 0.01/second to 0.3/second. If the lowest PLO rate observed were due entirely to background, a real 10 per cent anisotropy at a PLO rate of 0.01/second would be reduced to 9.7 per cent. Thus, any background contribution to D2 anisotropies will have at most a minimal effect.

C. Energy Spectrum

As discussed in Chapter III, part of the observed anisotropy is understood to be due to the Compton-Getting effect, whose size depends on the spectral index γ given by

$$\gamma = d\ell n\, j / d\ell n\, T$$

where j is the differential intensity, and T is the particle kinetic energy. The spectral index is determined from data from the Caltech EIS experiment. The function

$$dj/dT = A T^{\gamma} \qquad (4\text{-}5)$$

is fit in a least squares sense to the deduced omni-directional incident particle spectrum. A detailed description of this procedure is presented in Appendix B; a brief summary follows.

The observed energy losses in D2 due to stopping protons are grouped into 9 energy bins. The number of D2 events with these energy losses are summed over a 6-hour period. Not all of the energy losses observed in these energy bins are due to stopping protons. Stopping heavier nuclei, mostly alpha particles, make a small ($\sim 2\frac{1}{2}$ per cent) contribution. A correction for these heavy nuclei is made by extrapolating their observed spectrum at higher energies.

Some protons that do not stop in D2 also contribute to the D2 spectrum. Detectors 3, 4, and 5 are used to reject such protons, but a thin dead layer around the inside of D3 and D4 allows some protons which penetrate D2 to stop in but not trigger D3 or D4. The number of such protons is given by:

$$N = \int_{T_1}^{T_2} F(T)[1 - \varepsilon(T)]\,dT \ ,$$

where T is the proton's incident energy, protons with incident energies between T_1 and T_2 lose the appropriate amount of energy in D2, F is the fluence of protons, and ε is the efficiency with which D3, D4, and D5 detect penetrating protons. T_1 and T_2 are determined from range-energy tables, F(T) is determined from observed D25 events, and $\varepsilon(T)$ is estimated from results of an accelerator run and the instrument's response to large solar particle events. Pene-

trating protons typically contribute ~ 10 per cent to the total counts observed in D2.

After the corrections due to heavy nuclei and penetrating protons are made, the observed energy loss bins are corrected for the energy loss in the mylar window covering the telescope to determine the corresponding incident energy bins. Finally, the corrected counts and the incident energy bins are fit to the power law energy dependence given by eq. (4-5). The appropriateness of this dependence is investigated using the previously defined goodness-of-fit parameter χ^2_ν. Figure IV-5 presents the distribution of observed χ^2_ν and that predicted for 7 degrees of freedom. Periods when PLO is larger than 0.3/second or smaller than 0.01/second, when the satellite is not sunward of the earth, and periods near the beginning of a prompt solar particle event are not included. The closeness of the observed mean of 1.28 to 1. indicates that statistical fluctuations dominate observed deviations from a power law energy dependence.

Figure IV-6 shows the distribution of calculated γ's. The values range from -1 to -5 around a mean of -3.15. The finite number of counts used to calculate γ produces a statistical uncertainty in the result which produces a statistical uncertainty in the determination of the convective anisotropy: $\vec{\xi}_{CONV} = \frac{2}{w}(1-\gamma)\vec{V}$, so

$$\sigma_{\xi, CONV} = (2V/w)\sigma_\gamma$$

where V is the solar wind speed and w the average particle velocity. This uncertainty is typically 1/3 of the statistical uncertainty in the determination of the observed anisotropy using D2 analyzed events

Figure IV-5

The distribution of the goodness-of-fit parameter χ^2_ν determined from the energy-spectrum fits. The mean of the distribution is indicated. Also shown is the distribution expected if deviations from the fits were due only to statistical fluctuations.

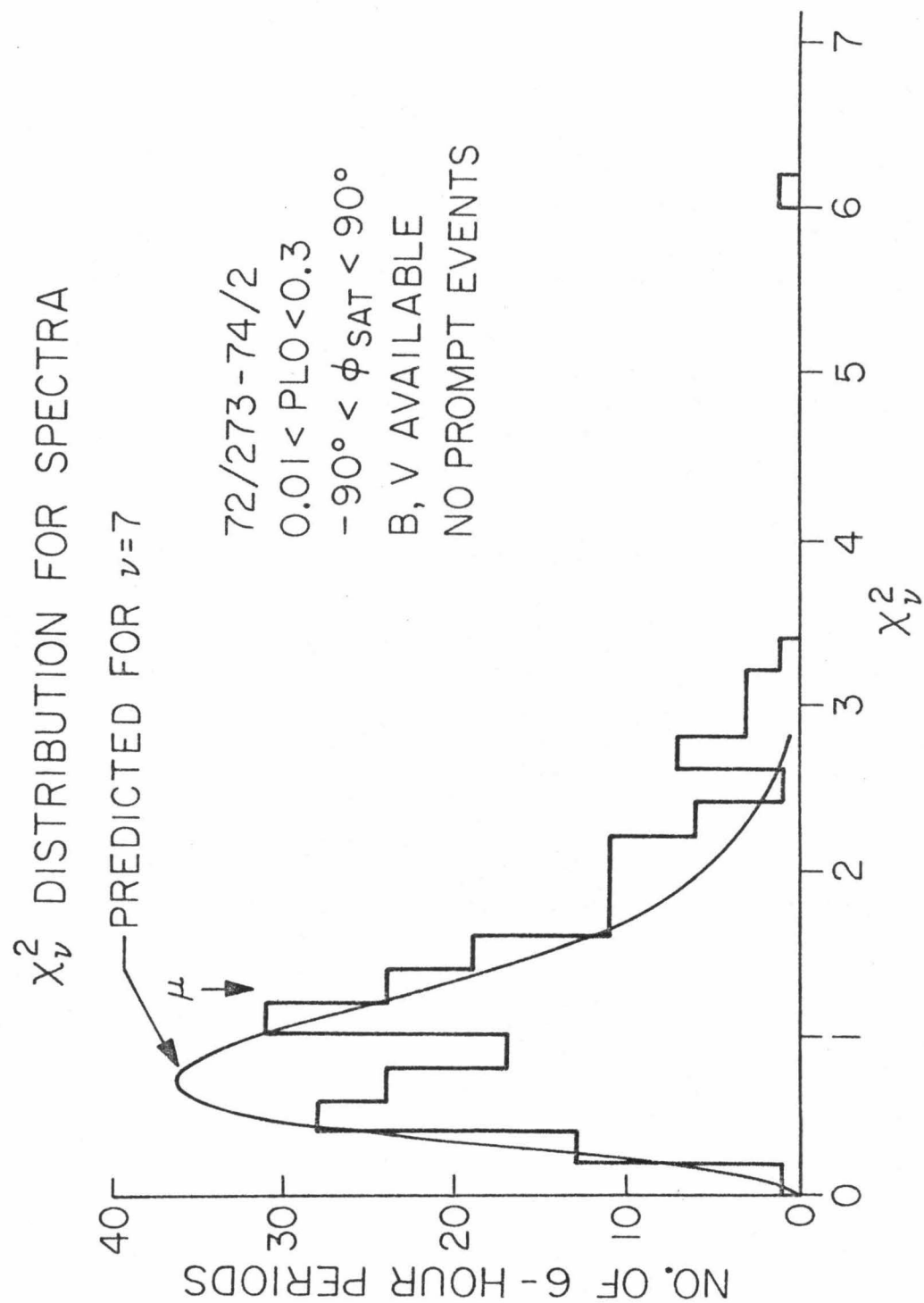
χ^2_ν DISTRIBUTION FOR SPECTRA
PREDICTED FOR $\nu=7$
μ
72/273-74/2
0.01 < PLO < 0.3
$-90° < \phi_{SAT} < 90°$
B, V AVAILABLE
NO PROMPT EVENTS
NO. OF 6-HOUR PERIODS
0
10
20
30
40
0
1
2
3
4
5
6
7
χ^2_ν

Figure IV-6

The distribution of the spectral index γ. Also shown are the mean and standard deviation of the ensemble as well as a typical 1 σ statistical uncertainty in the determination of an individual γ.

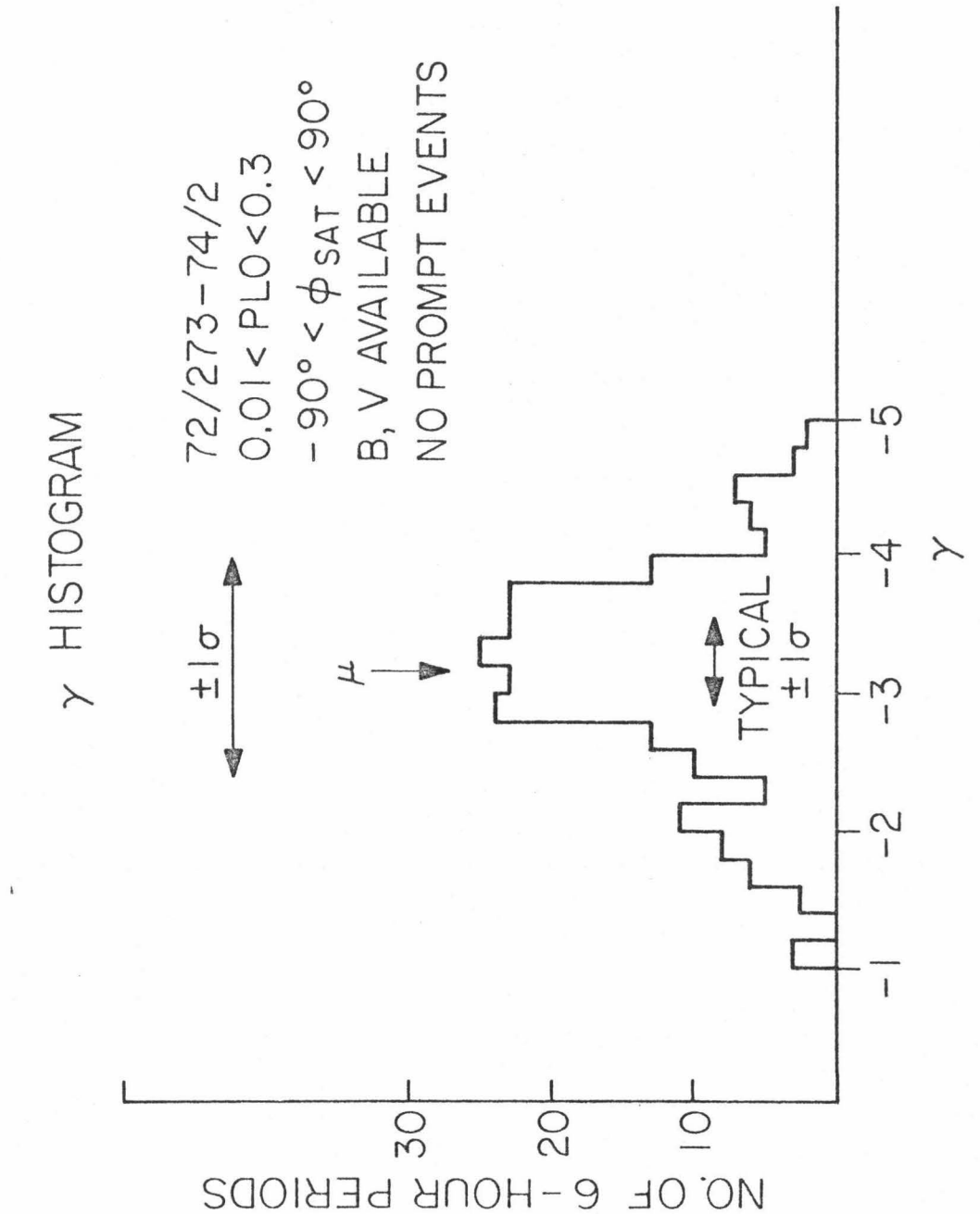
γ HISTOGRAM
72/273-74/2
0.01 < PLO < 0.3
-90° < φ SAT < 90°
B, V AVAILABLE
NO PROMPT EVENTS
±1σ
μ
TYPICAL ±1σ
NO. OF 6-HOUR PERIODS
30
20
10
-1
-2
-3
-4
-5
γ

and so contributes only ~ 10 per cent of the uncertainty in the determination of the diffusive anisotropy.

The average particle velocity used in anisotropy equations such as (3-4) is determined by:

$$\langle \frac{1}{w} \rangle = [\int_{T_1}^{T_2} T^{\gamma} T^{-\frac{1}{2}} dT] / [\int_{T_1}^{T_2} T^{\gamma} dT] \quad ,$$

where T_1 and T_2 define the energy interval contributing to the anisotropy. The resultant average particle velocity is rather insensitive to the value of γ ; a change of γ from -3 to -4 changes $\langle \frac{1}{w} \rangle$ by only 1 per cent for D2 analyzed events.

D. Solar Wind

As indicated by eq. (3-4), the solar wind speed and direction are needed to compute the convective anisotropy. Hourly averages of the solar wind speed measurements by the MIT plasma experiment on IMP-7 are combined into 6-hour averages for use in this study. The distribution of 6-hour averages is shown in Figure IV-7. The standard deviation in the measurements for each of these averages is also calculated. Figure IV-8 shows the distribution of the ratio of this standard deviation to the average. For 90 per cent of the periods the standard deviation is less than 5 per cent of the average for the 6-hour period, indicating that the average is a good approximation to the solar wind speed for the entire 6-hour period.

Solar wind speeds larger than 700 km/second have been indicated as possibly unreliable in the preliminary data set available. Consequently, the 134 6-hour periods having an hourly average speed greater than 700 km/second are omitted from this study.

Figure IV-7

The distribution of the 6-hour averages of the observed solar wind speed. The mean 6-hour average is indicated.

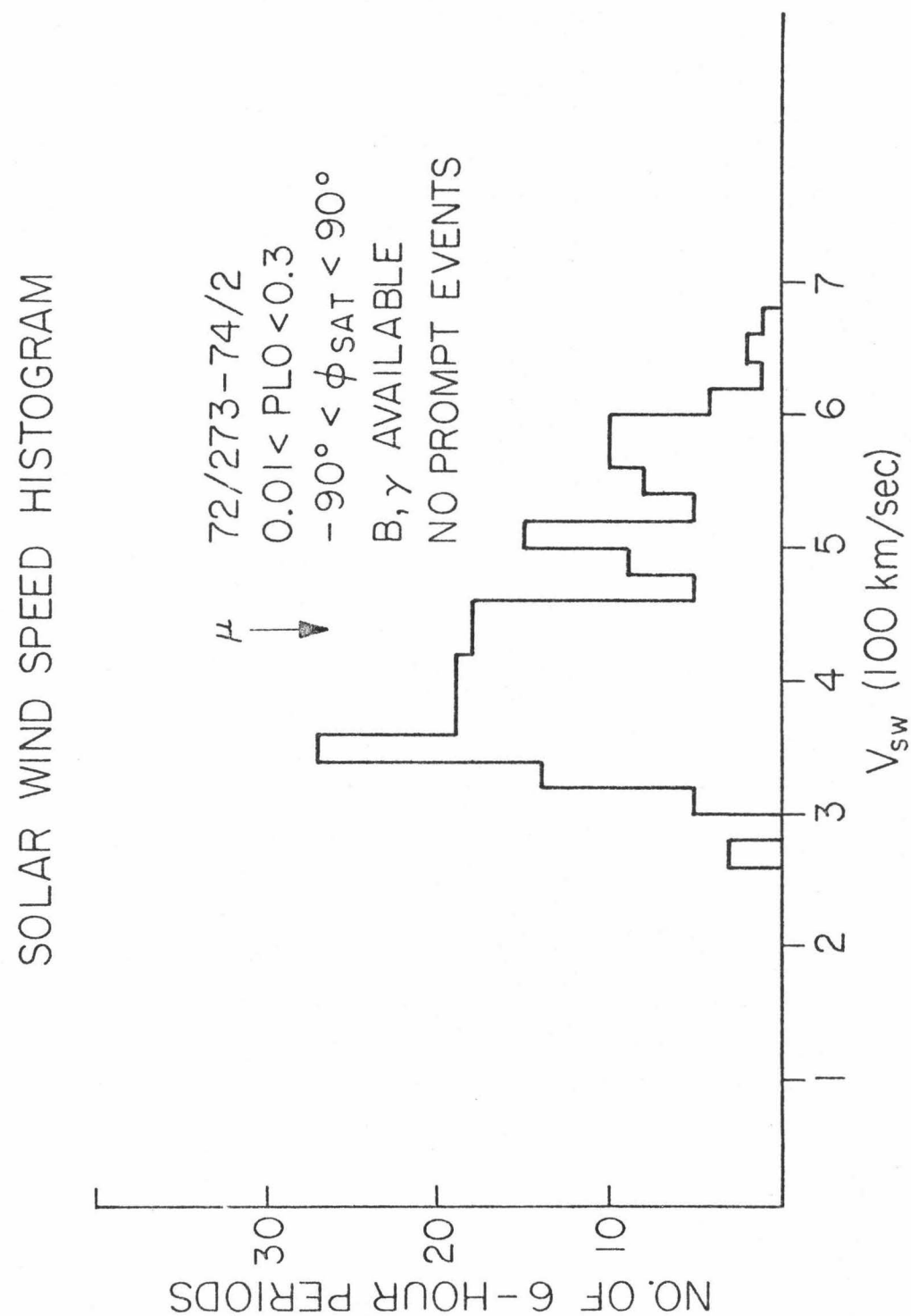
SOLAR WIND SPEED HISTOGRAM
72/273-74/2
0.01< PLO <0.3
-90° < φSAT < 90°
B, γ AVAILABLE
NO PROMPT EVENTS
μ
NO. OF 6-HOUR PERIODS
10
20
30
1
2
3
4
5
6
7
Vsw (100 km/sec)

Figure IV-8

The distribution of the ratio of the standard deviation and the mean of the ensemble of individual solar wind speed measurements used in computing the 6-hour average solar wind speeds.

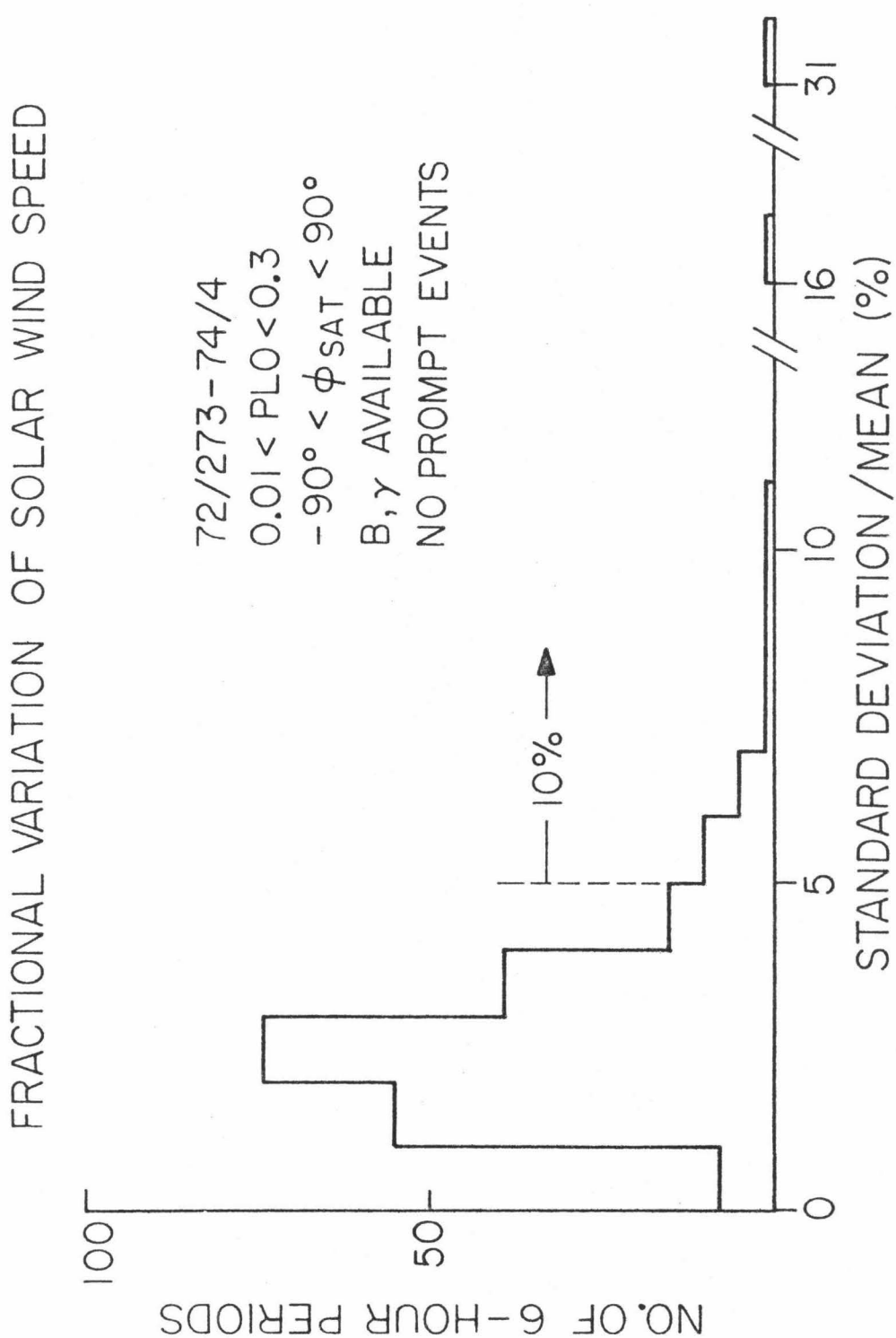
FRACTIONAL VARIATION OF SOLAR WIND SPEED
72/273-74/4
0.01 < PLO < 0.3
-90° < φSAT < 90°
B, γ AVAILABLE
NO PROMPT EVENTS
10%
NO. OF 6-HOUR PERIODS
100
50
0
5
10
16
31
STANDARD DEVIATION / MEAN (%)

The solar wind is assumed to be radial. Previous measurements of the azimuthal flow angle have been reviewed by Wolfe (1972). The mean direction found by different experiments varies from $+3.0^{\circ}$ to -2.52° from radial, although this variation may be due to systematic errors. A typical standard deviation in the observations of a single experiment is 3°. For a typical convective anisotropy amplitude of -20 per cent, a 3° error in the solar wind direction produces an error of ~ 1 per cent in the direction perpendicular to radial and a negligible error in the radial direction.

E. Magnetic Field

As discussed in Chapter III, the diffusion of low-energy protons in interplanetary space is understood to be controlled by the magnetic field. Hourly averages of the interplanetary magnetic field have been obtained from the National Space Science Data Center for the period 72/273 to 74/15. The primary source of these data is the Imperial College magnetometers aboard the earth-orbiting HEOS-1 and HEOS-2 satellites. The remainder of the data are from the GSFC magnetometer aboard IMP-8.

The field direction used for a 6-hour period is determined by computing

$$\vec{B}^{*}_{6\text{-hour}} = \left\langle \frac{\vec{B}_{1\text{-hour}}}{|\vec{B}_{1\text{-hour}}|} \right\rangle \quad .$$

The direction defined by the projection of this field onto the ecliptic plane is used as the 6-hour average field direction. The distribution of 6-hour average field directions is shown in Figure IV-9.

Significant variations are found within the 6-hour periods. A

Figure IV-9

The distribution of the 6-hour averages of the observed interplanetary magnetic field direction.

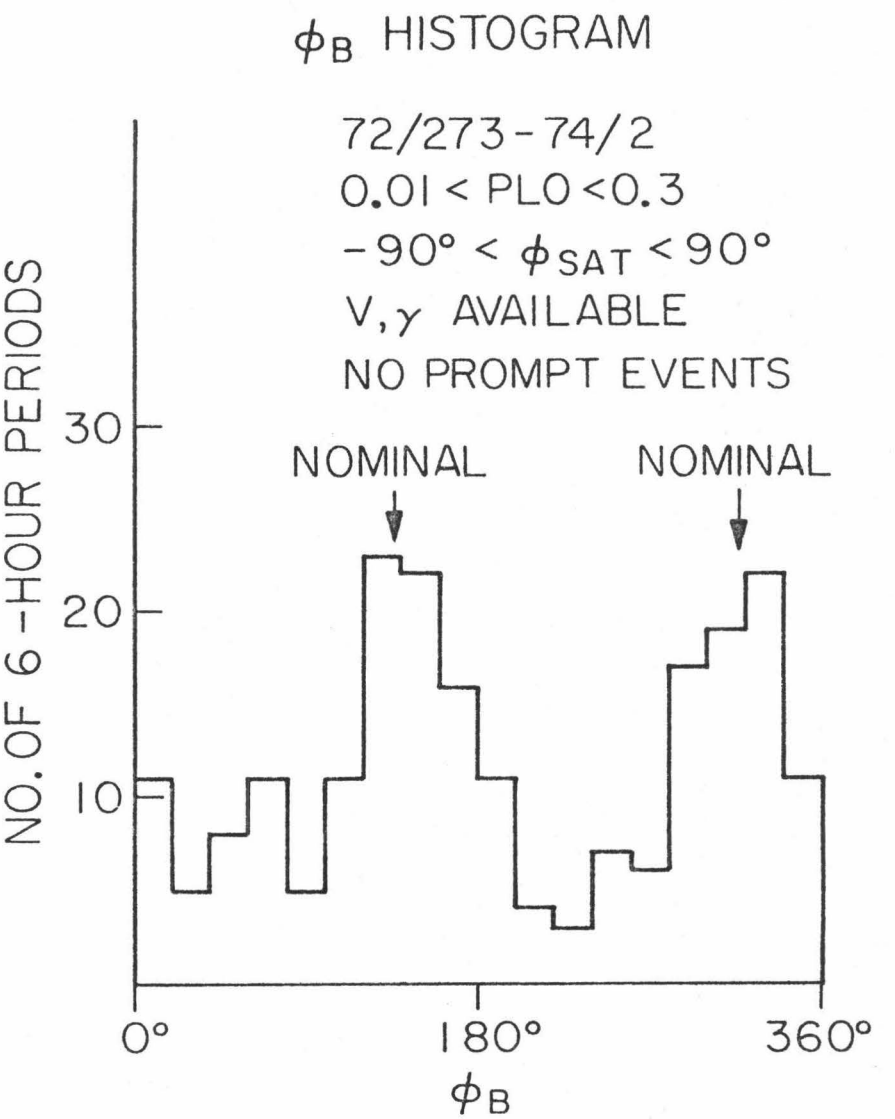
ϕ_B HISTOGRAM
72/273-74/2
0.01 < PLO < 0.3
$-90° < \phi_{SAT} < 90°$
V, γ AVAILABLE
NO PROMPT EVENTS
NOMINAL
NOMINAL
NO. OF 6-HOUR PERIODS
30
20
10
0°
180°
360°
ϕ_B

$\Delta\phi$ is defined for each hourly average field direction:

$$\Delta\phi = \phi_{1\text{-hour}} - \phi_{6\text{-hour}} ,$$

where the 1-hour period is included within the 6-hour period. Figure IV-10 is a histogram of $\Delta\phi$. The standard deviation, $\sigma_{\Delta\phi}$, of the distribution is 36°. This variation reduces measured field-aligned anisotropies. An estimate of the size of the reduction is obtained by approximating the distribution of $\Delta\phi$ as a Gaussian distribution with a standard deviation of 36°. Such a distribution of field directions reduces the measurement of field-aligned anisotropies by a factor of 0.82.

The 6-hour average magnetic field directions are later compared to the diffusive anisotropy direction. The variation in the magnetic field direction is a scale size for the root mean square difference between the computed field direction and the effective field direction seen by the average particle. For example, occasionally only 5 hourly averages are available to compute the 6-hour average field direction. The root mean square difference between the computed field direction and the direction that would have been computed had all 6 hourly averages been available is $\sim \sigma_{\Delta\phi}/6$ or $\sim 6^{\circ}$.

Figure IV-10

The lower panel is the distribution of the differences in the hourly average magnetic field direction ϕ and the 6-hour average field direction $\overline{\phi}$ in which the hourly average is included. The upper panel is a histogram of the number of hourly averages included in the 212 6-hour periods.

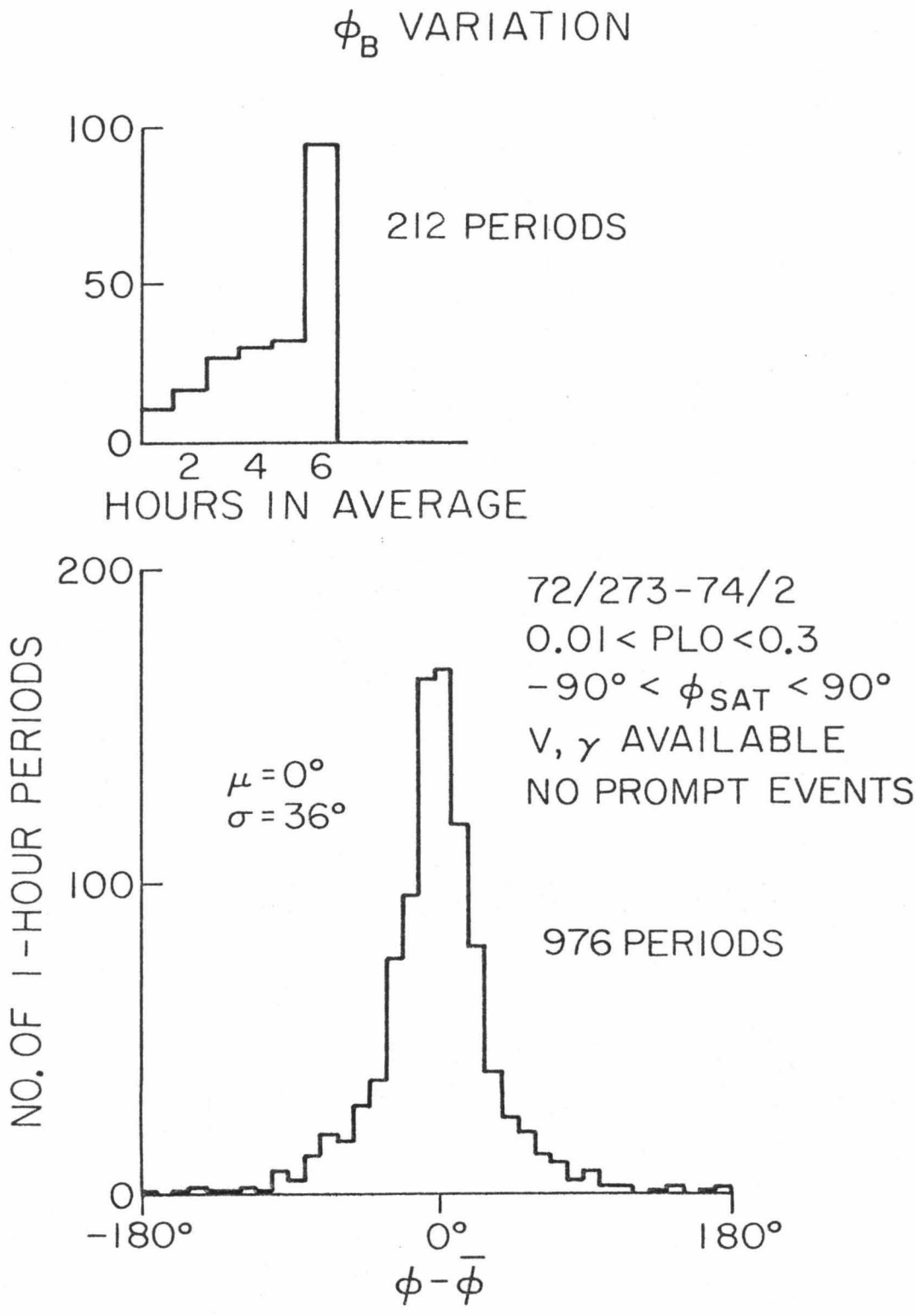
ϕ_B VARIATION
100
50
0
212 PERIODS
2 4 6
HOURS IN AVERAGE
200
100
0
NO. OF 1-HOUR PERIODS
72/273-74/2
0.01 < PLO < 0.3
$-90° < \phi_{SAT} < 90°$
V, γ AVAILABLE
NO PROMPT EVENTS
$\mu = 0°$
$\sigma = 36°$
976 PERIODS
-180°
0°
180°
$\phi - \bar{\phi}$

V. DATA SELECTION

A. Introduction

The primary data set for this study runs from 72/273 to 74/2. The set begins when the first useable information from the IMP-7 satellite was obtained; the end of the set is the last time for which simultaneous solar wind velocity and magnetic field direction have been obtained. Figure V-1 is a plot of the PLO rate for this time span. Those 6-hour periods used for the results of this study having a PLO rate ≥ 0.01/second are identified. Some periods are not used because either the proton or plasma data are not available, while others have been rejected in order to avoid possible sources of error. In addition, since the purpose of this study is to investigate streaming during periods between prompt events, periods dominated by prompt events are not included in the primary data set. For much of the analysis a minimum proton flux is required in order to avoid periods when computed anisotropies have large statistical uncertainties. An analysis of the selection process and of the possible sources of error that have been avoided follows.

As indicated in the previous chapter, 6-hour averages of the proton and plasma data are used. There are 1839 6-hour periods in the time span from 18:00 UT 72/273 to 12:00 UT 74/2. Proton fluxes and their associated anisotropies are available for 1720 (94 per cent) of these periods, magnetic field data for 1543 (84 per cent) periods, and solar wind data for 1586 (86 per cent) periods. There are 1264 (69 per cent) periods for which all these data are available.

Figure V-1

The 6-hour averages of the PLO rate for the time span used in this work. Periods when the satellite is sunward of the earth are indicated. Periods when the PLO rate is between 0.01/second and 0.3/second that are used in this work are also indicated.

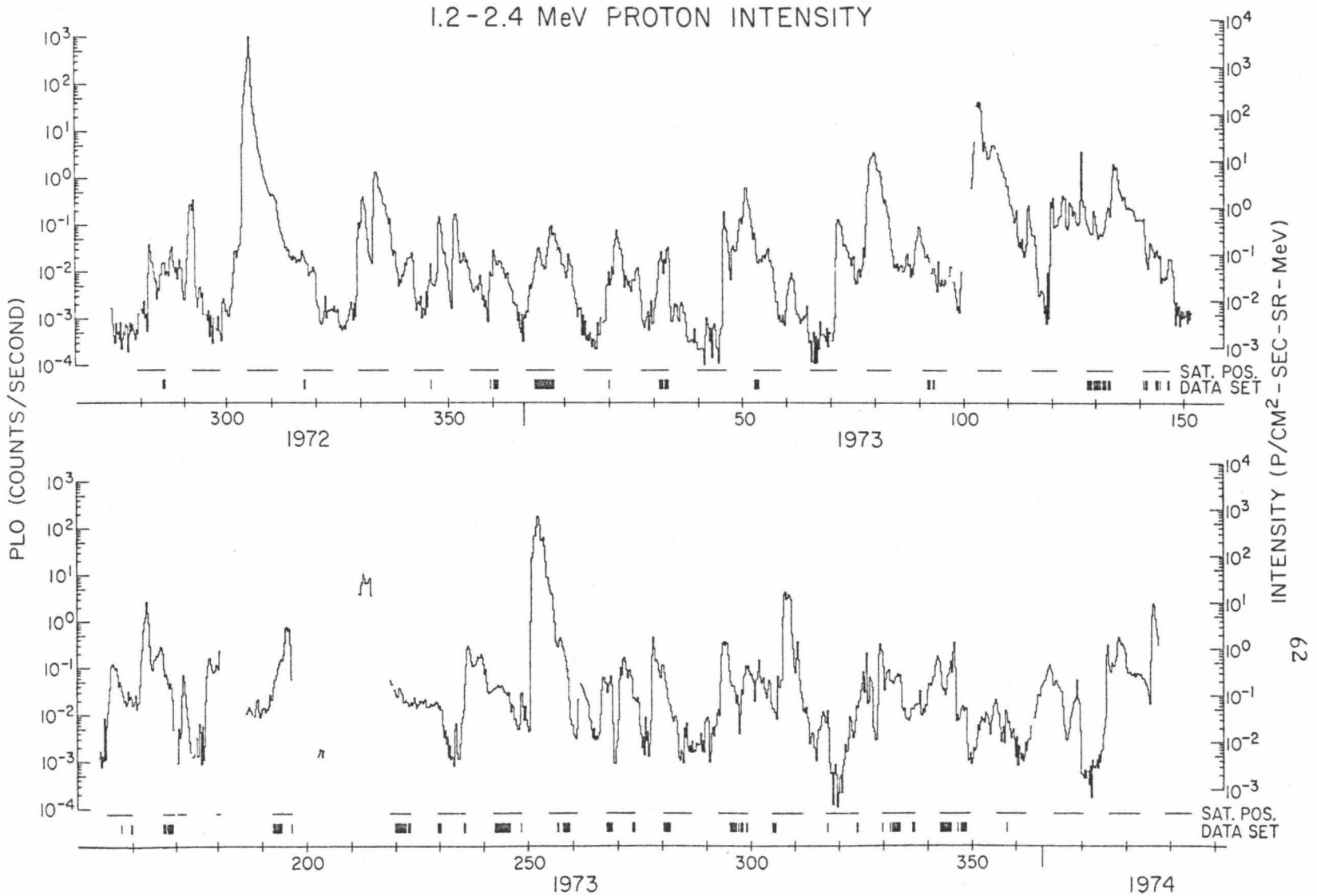
1.2-2.4 MeV PROTON INTENSITY
PLO (COUNTS/SECOND)
INTENSITY (P/CM2 - SEC - SR - MeV)
SAT. POS.
DATA SET
300
350
50
100
150
1972
1973
200
250
300
350
1973
1974

B. Instrumental Effects

Several possible instrumental sources of error were discussed in Chapter IV. Long term biases affecting the anisotropy of sectored rates were shown to be small by computing the anisotropy of two rates dominated by an isotropic background. It was shown that anisotropies using sectored rates and analyzed events are consistent. An upper limit was placed on the background rate for D2 events which indicated that the anisotropy of D2 events is negligibly affected by any such background. The effect of these possible sources of errors is sufficiently small so that no periods have been eliminated to avoid them. Very rarely an error is made in the sectored rate data that produces a very large number of counts in one sector. These periods have been identified by the poor fit made to the data when computing the anisotropy. There are nine such 6-hour periods, each having a goodness-of-fit parameter χ_ν greater than 200. There is no indication of any similar effect in the analyzed events or other sectored rates during these periods. Nevertheless, no data from these 9 periods when this malfunction occurred are used in this study.

Large fluxes can introduce errors into anisotropy measurements of sampled events such as D2 analyzed events. A bias is put into the anisotropy measurement because the instrument can transmit only one analyzed event every 0.64 seconds. Sectored rates are not affected by this problem and so can be used to estimate the size of errors. In the limit of large fluxes the analyzed events become isotropic. Roelof (1974) has made a theoretical study of the effect for a class of instruments similar to the Caltech experiment. The

major difference in the Caltech experiment is that the priority assigned to events during the current readout period depends on whether the most recent event read out was a narrow geometry electron-type event. However, this changing priority structure has a small effect on the measured anisotropy of D2 events during the periods used in this study. The previous readout is usually a narrow-geometry proton (rate $\sim$ PLO), a wide-geometry event (rate $\gtrsim 0.3$ second), or a neutral event (rate $\sim$ 0.1/second) rather than a narrow-geometry electron-type event (rate $\approx$ ELO + EHI $\approx$ 0.1/second). So to a first approximation, narrow-geometry electron events always have the highest priority. This reduces the live time for D2 analyzed events by the probability of getting a narrow-geometry electron-type event during a readout period -- $\sim$ 6 per cent. An anisotropy in the electron rate would make the live time depend on the spacecraft viewing angle and thus affect the anisotropy measured using D2 analyzed events. As discussed in Chapter IV, ELO and EHI are usually isotropic. The anisotropy for ELO + EHI rates summed over all periods used in this study with 0.01/second < PLO < 0.03/second is 0.5 per cent $\pm$ 0.4 per cent. Thus, the difference in live times introduces an error of $\sim$ (0.5 per cent)$\cdot$(6 per cent), or 0.02 per cent.

Since the history dependence of the priority system of the Caltech instrument has a minimal effect, the rate dependence of the anisotropy of D2 analyzed events is compared to the formulas derived by Roelof for small anisotropies:

$$r \equiv \frac{|\xi_{OBS}|}{|\xi_{true}|} = \frac{1}{1+n^2}\left[\left(1+n^2\,\frac{n\sin\gamma+\cos\gamma-1}{e^{n\gamma}-1}\right)^2+n^2\left(1-n\,\frac{\sin\gamma+n-n\cos\gamma}{e^{n\gamma}-1}\right)\right]^{\frac{1}{2}} \qquad (5-1)$$

$$\tan(\Delta\phi) \equiv \tan(\phi_{OBS} - \phi_{true}) = n \frac{e^{n\gamma} - 1 - n(\sin\gamma - n\cos\gamma + n)}{e^{n\gamma} - 1 + n^2(n\sin\gamma + \cos\gamma - 1)} \quad , \qquad (5\text{-}2)$$

n = mean event rate/radian

$\gamma = (\tau_o - \tau_1)\omega$

ω = rotation rate = 4.77 radians/sec

τ_o = read out period = 0.64 seconds

τ_1 = dead time for read out = 0.03 seconds

The anisotropy of the PLO rate is used as a measure of the true or unbiased anisotropy of D2 analyzed events. As noted in Chapter IV, PLO events have a slightly larger energy interval than D2 analyzed events, and so the anisotropies of the two event types may be only approximately equal.

The mean value of r and $\Delta\phi$ are plotted as a function of the PLO rate in Figures V-2 and V-3. The solid lines are the values predicted by eqs. (5-1) and (5-2) in the approximation that all priority 0 and 1 events are PLO events. Only periods when both anisotropies are statistically significant ($\xi/\sigma_\xi > 2.5$) are included.

The observed values of r and $\Delta\phi$ are consistent with the predicted values except r does not approach 1 for small PLO rates. However, r is essentially constant for PLO less than 0.3/second, indicating that the discrepancy is not a biasing effect caused by high rates. Consequently, only periods when the PLO rate is less than 0.3/second are included in the final data set of this study. At a PLO rate of 0.3/second, eqs. (5-1) and (5-2) give $r = 0.95$ and $\Delta\phi = 3^o$ with correspondingly smaller values for lower rates. Thus, any biasing effect caused by high rates will minimally affect the observed

Figure V-2

The mean of the ratio of the anisotropy amplitude determined using D2 analyzed events to the anisotropy amplitude determined using the sectored PLO rate as a function of the PLO rate. Only periods when the anisotropy amplitude ξ is more than 2.5 times the statistical uncertainty in the anisotropy amplitude σ_ξ for both D2 and PLO anisotropies are included. Periods when the average ELO rate is larger than 0.15/second are not used. The ratio calculated using eq. (5-1) is shown by the solid curve.

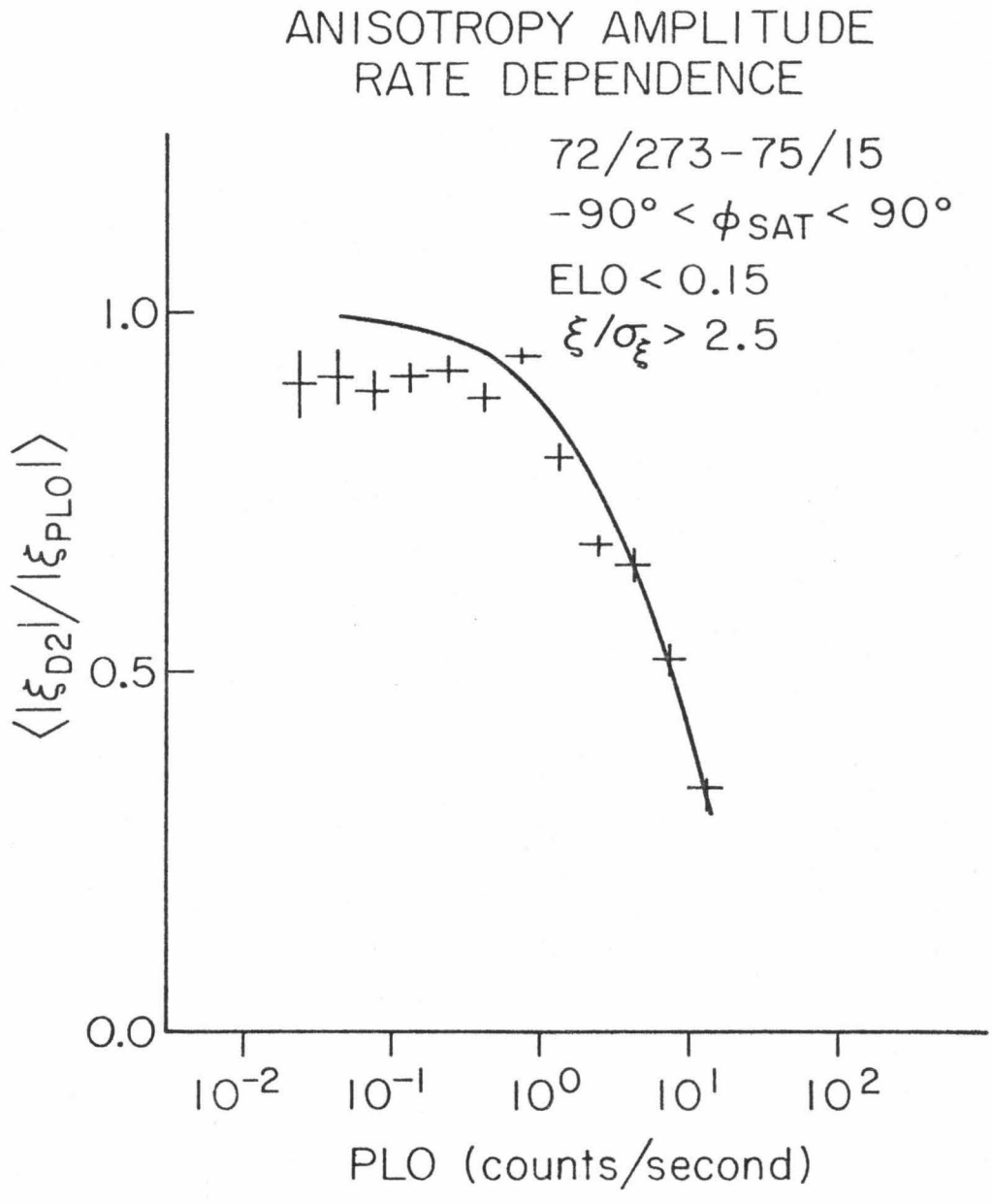
ANISOTROPY AMPLITUDE
RATE DEPENDENCE
72/273-75/15
-90° < φSAT < 90°
ELO < 0.15
ξ/σξ > 2.5
1.0
0.5
0.0
⟨|ξD2|/|ξPLO|⟩
10-2
10-1
100
101
102
PLO (counts/second)

Figure V-3

The mean difference in the direction of the anisotropy determined using D2 analyzed events and the direction of the anisotropy determined using the sectored PLO rate as a function of the PLO rate. The difference calculated using eq. (5-2) is shown by the solid curve.

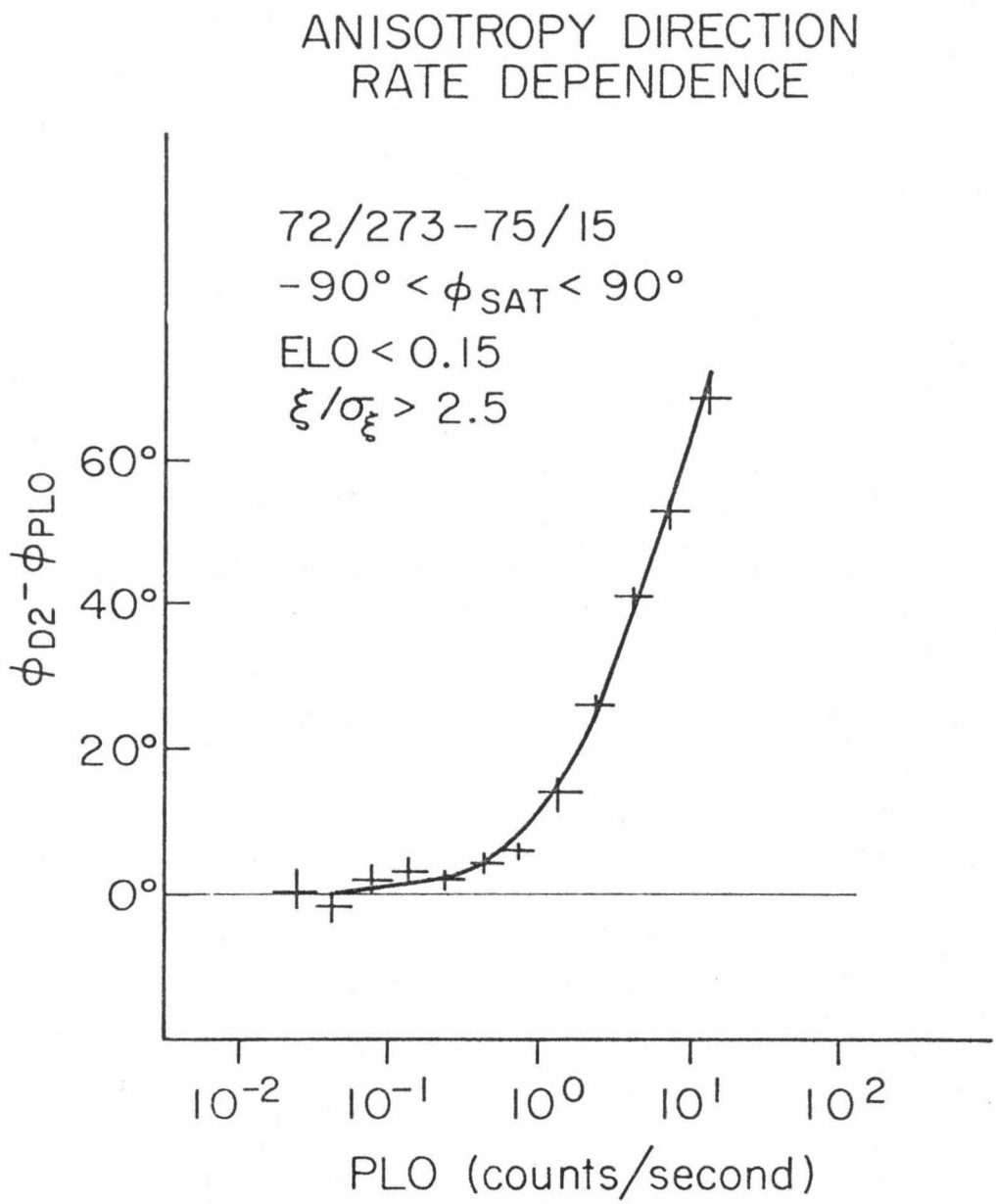
ANISOTROPY DIRECTION
RATE DEPENDENCE
72/273-75/15
-90° < φSAT < 90°
ELO < 0.15
ξ/σξ > 2.5
φD2 - φPLO
60°
40°
20°
0°
10-2
10-1
100
101
102
PLO (counts/second)

anisotropies for the periods used in this study.

Since $\vec{\xi} = 3\vec{S}/wU$, an estimate of the differences of anisotropies using PLO and D2 analyzed events is given by the ratio of the average particle velocities. The ratio of 0.96 for protons is not quite as small as the observed ratio of $\sim$ 0.91 at low rates. The remaining factor of $\sim$ 0.95 is not understood, but is a small effect. Typical anisotropies used in this study are $\sim$ 10 per cent. A correction factor of 0.95 would mean the true anisotropy is 10.5 per cent. Because the factor of $\sim$ 0.95 is not understood, the anisotropy of D2 analyzed events is used as measured.

No attempt has been made to correct the observed anisotropy of D2 analyzed events for high rates; instead, periods when the PLO rate is larger than 0.3/second are not included in this study. Equation (5-1) indicates that the measured anisotropy will be 0.95 of the true anisotropy at a PLO rate of 0.3/second. This typically is an absolute error of $\sim$ 0.5 per cent in the anisotropy measurement. Most periods used have smaller rates and so correspondingly smaller errors.

Anisotropies could be determined at higher fluxes using PLO sectored rates. This has not been done since periods with PLO rates $>$ 0.3/second are predominantly due to prompt solar events, while the purpose of this work is to study the periods between prompt events.

C. Magnetospheric Influence

The purpose of this work is to study the interplanetary streaming of protons. Consequently, only periods when the satellite is out-

side the earth's bow shock -- the first interaction of the earth's magnetic field with the solar wind -- are included in the final data set of this work. Data taken when the satellite is inside the bow shock are used only in this section for comparison with data taken in interplanetary space.

To limit the data set to interplanetary space, only periods when the satellite is sunward of the earth are included. This corresponds to a range from -90^{o} to $+90^{o}$ in the Geocentric Solar Ecliptic longitude of the satellite position. As indicated in Figure II-1, this is outside of the average position of the earth's bow shock as determined by Behannon (1968) during 1966.

The presence of the earth could influence observed anisotropies even when the satellite is outside the bow shock. The magnetosphere could be a source of low-energy protons or could distort the local flow of interplanetary protons. Krimigis, et al. (1975) have reported a highly anisotropic flow of 0.29 to 0.5 MeV protons from the direction of the earth using data from the JHU/APL experiment aboard IMP-7 while IMP-7 was in interplanetary space. Using the Caltech experiment on IMP-7, Mewaldt, et al. (1975b), looking at similar periods, did not find this streaming at the higher energy interval of 1.3 - 2.3 MeV -- the same energy interval used in the present study. The absence of streaming for particles > 1 MeV is consistent with the source of these particles proposed by Hovestadt and Scholer (1976) to explain the source of the lower energy fluxes.

The size of any possible magnetospheric effect on interplanetary particle streaming is determined by the interaction of the mag-

netosphere with the interplanetary medium as seen by ~ $1\frac{1}{2}$ MeV protons, which have a Larmor radius of ~ 5 earth radii. Due to the complexity and variability of this interaction, no attempt has been made to calculate theoretically the effect of the magnetosphere. Rather, the dependence of the observed anisotropy of the satellite position has been examined. A dependence of the anisotropy on satellite position would be expected if the earth blocked the flow of particles from beyond 1 AU. This blockage would be more effective when the satellite is near -45° when the field line connecting the satellite to regions beyond 1 AU must drape over the magnetosphere than when the satellite is near $+45^{\circ}$ when the corresponding field line usually will not encounter the magnetosphere.

Figure V-4 shows the anisotropy amplitude observed as a function of spacecraft position. To reduce statistical uncertainties in the individual points, 6-hour averages have been combined into daily averages. An outstanding feature of the plot is the comparatively small anisotropies seen when the satellite is near 180° -- roughly when the satellite is inside the magnetopause. Outside of ~ 140° to 210° the anisotropies are at least qualitatively independent of satellite position. For more quantitative comparisons, the data have been grouped into 3 regions:

Region 1	0° to 90°	interplanetary space
Region 2	-90° to 0°	interplanetary space
Region 3	140° to 210°	~ magnetotail

The final data set includes data from only Regions 1 and 2. If the magnetosphere has little influence on anisotropies in interplanetary

Figure V-4

The amplitude of the observed anisotropy as a function of the longitude of the IMP-7 satellite in Geocentric Solar Ecliptic coordinates. A typical $\pm 1\sigma$ error bar is indicated.

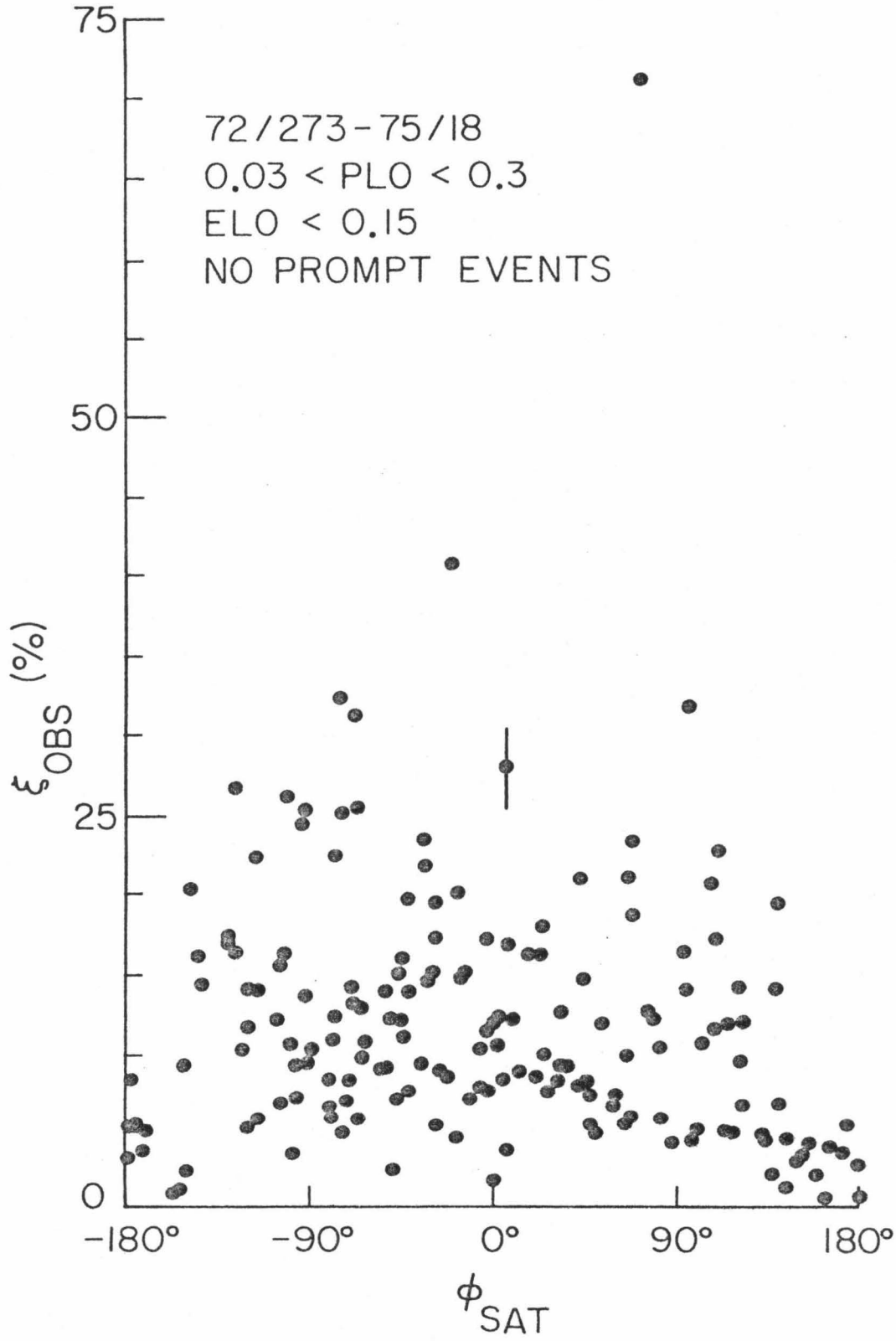
75
50
25
0
72/273-75/18
0.03 < PLO < 0.3
ELO < 0.15
NO PROMPT EVENTS
ξ_{OBS} (%)
-180°
-90°
0°
90°
180°
ϕ_{SAT}

space, Region 1 and Region 2 will have similar distributions. Histograms of the observed anisotropy amplitudes are shown in Figure V-5 for each of the above regions. The mean anisotropies for the regions are:

Region 1	12.6 per cent ± 1.7 per cent
Region 2	13.5 per cent ± 1.0 per cent
Region 3	3.8 per cent ± 0.5 per cent

The difference of the mean anisotropy of Regions 1 and 2 is not statistically significant; the Student's t-test indicates more than a 60 per cent probability of observing as large a difference due to chance alone. In contrast, the mean anisotropy for Region 3 is only 1.2 standard deviations above the mean amplitude of 3.2 per cent expected if the flux were isotropic. Thus, while the magnetosphere has a significant effect on anisotropy measurements when the satellite is in the magnetotail, there is no indication of magnetospheric influence on measurements taken in interplanetary space.

The magnetosphere could affect the observed anisotropy but still maintain the same average amplitude. Figures V-6 and V-7 plot the individual observed anisotropy vectors for Regions 1 and 2, respectively, using 6-hour averages. Again, the distributions for the two regions are similar. The characteristics of the distributions of the x- and y-components are:

	Region 1		Region 2	
No.	151		205	
Mean	-7.82 %	-2.15 %	-9.12 %	-3.90 %
Sigma	13.4 %	14.6 %	11.9 %	12.0 %
Median	-8.12 %	-3.49 %	-9.39 %	-4.63 %

Figure V-5

Histograms of the amplitude of the observed anisotropy for three intervals of the longitude of the IMP-7 satellite. The mean amplitude is indicated for each histogram.

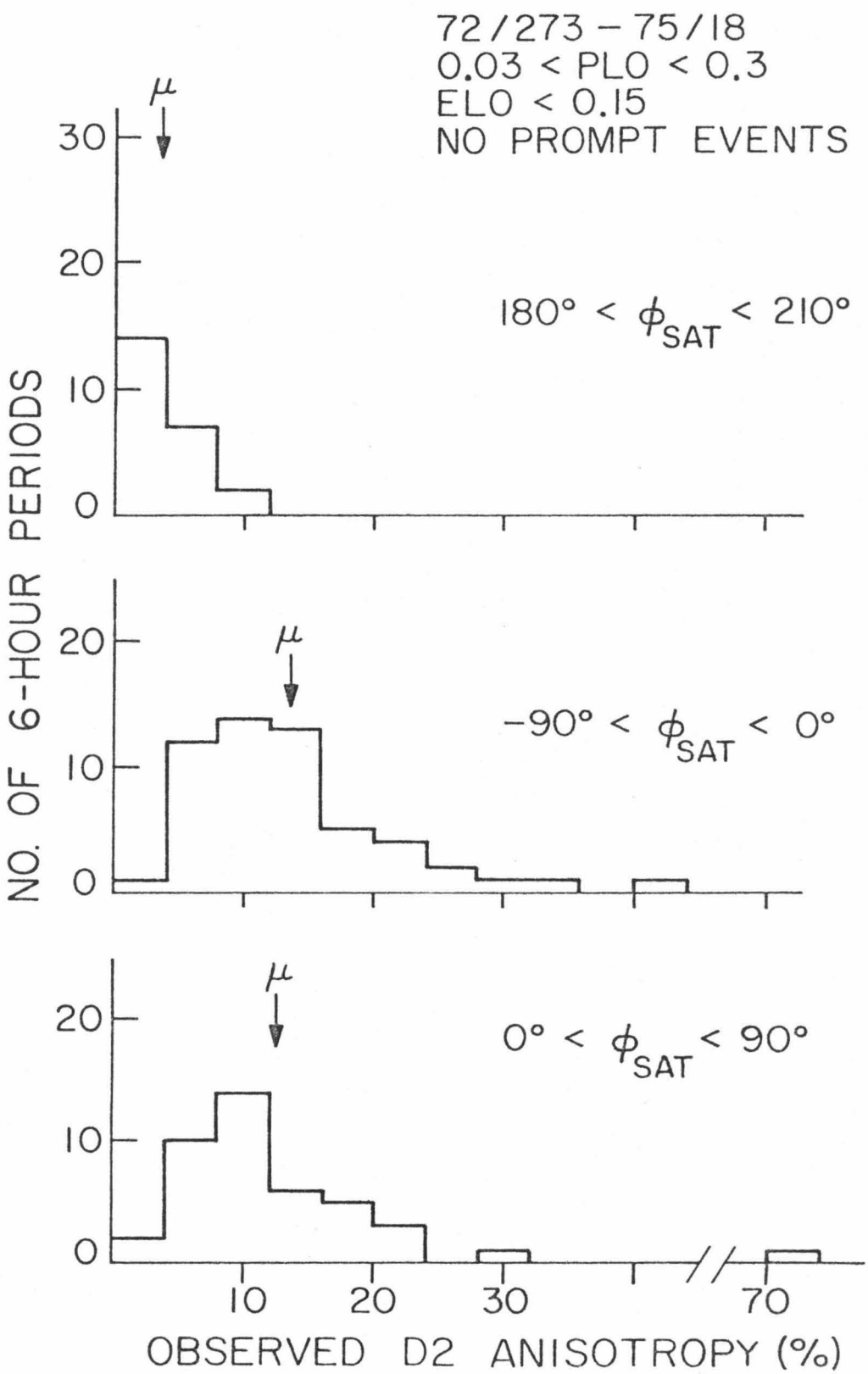
72/273 – 75/18
0.03 < PLO < 0.3
ELO < 0.15
NO PROMPT EVENTS
μ
180° < φSAT < 210°
−90° < φSAT < 0°
0° < φSAT < 90°
NO. OF 6-HOUR PERIODS
0
10
20
30
70
OBSERVED D2 ANISOTROPY (%)

Figure V-6

The observed anisotropy for periods when the longitude of IMP-7 is between -90^{o} and 0^{o}. The data are from 72/273 to 75/18. The means of the x- and y-components of the anisotropy are indicated.

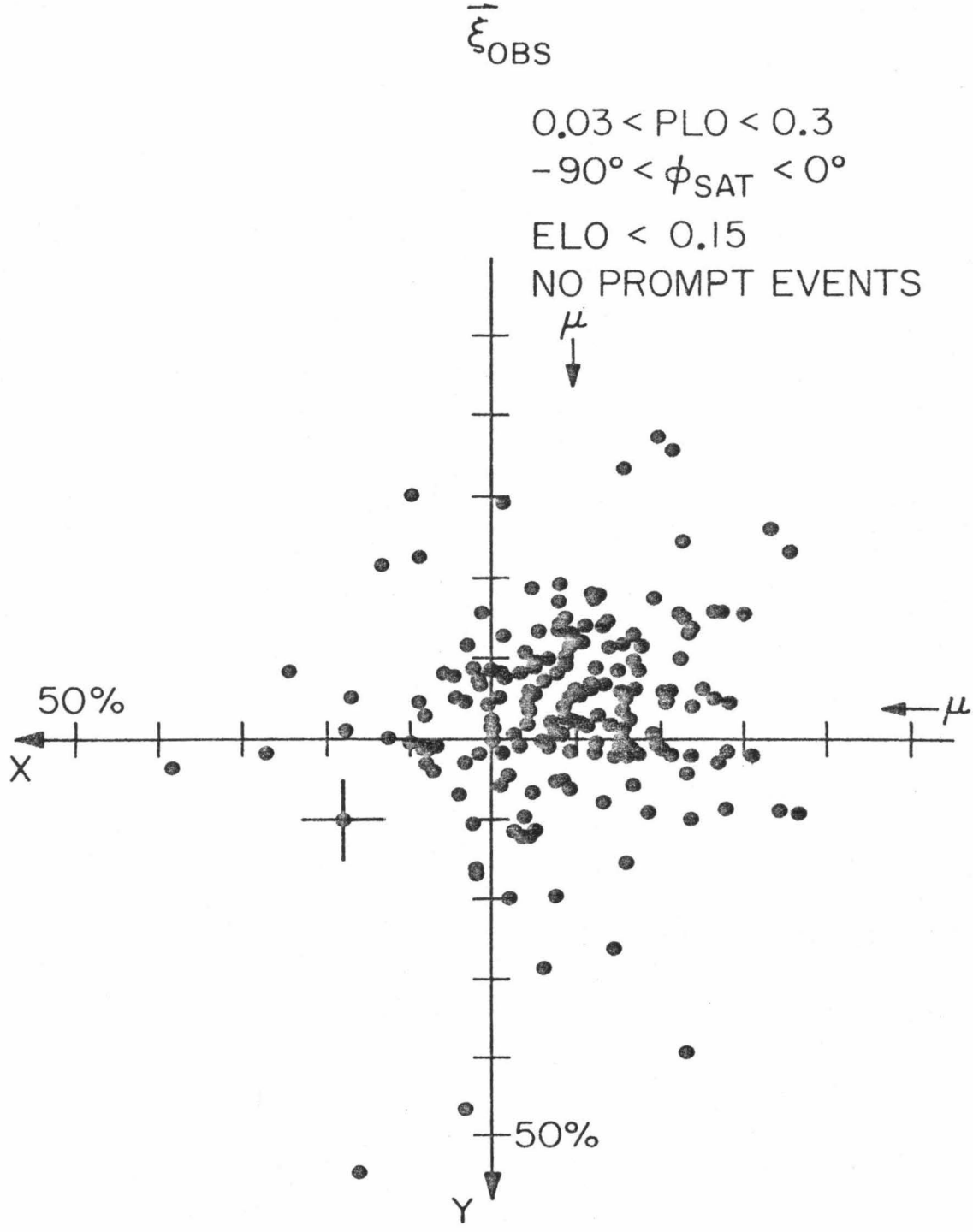
$\vec{\xi}_{OBS}$
0.03 < PLO < 0.3
$-90° < \phi_{SAT} < 0°$
ELO < 0.15
NO PROMPT EVENTS
μ
50%
X
μ
50%
Y

Figure V-7

The observed anisotropy for periods when the longitude of IMP-7 is between 0^{o} and $+90^{o}$. The data are from 72/273 to 75/18. The means of the x- and y-components of the anisotropy are indicated.

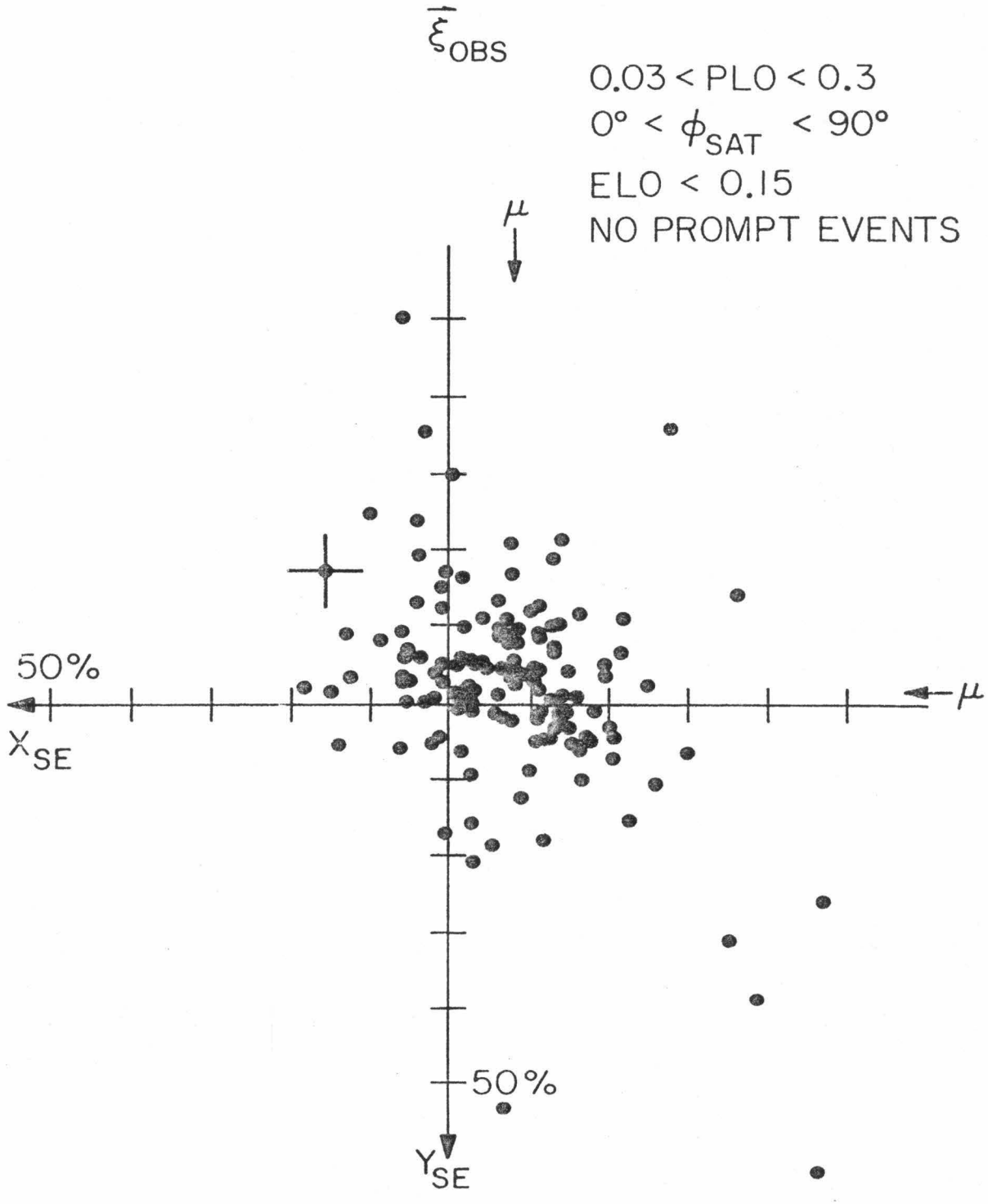
$\vec{\xi}_{OBS}$
0.03 < PLO < 0.3
0° < ϕ_{SAT} < 90°
ELO < 0.15
NO PROMPT EVENTS
μ
50%
X_{SE}
μ
50%
Y_{SE}

The result of applying the t-test to the differences in the means is that there is no significant difference in either component average at the 80 per cent confidence level. The difference in the sigmas can be compared using the F-test. The probability of finding differences as large as those observed due to random fluctuations is 5 per cent for the x-component and 1 per cent for the y-component.

The apparently significant difference in the spread of the distributions must be interpreted with caution. The difference reflects the existence of a few periods with anisotropies much larger than typically found. For example, removing two periods from Region 1 will make the sigma in the x-direction smaller than that found in Region 2. Thus, the estimate of the chance likelihood of such a difference using the F-test appears too small. This reflects the existence of non-Gaussian tails of the observed distributions.

In summary, the evidence indicates that any magnetospheric influence on the anisotropies observed in interplanetary space is small. No significant difference was found in either the mean amplitude, the mean x-component, or the mean y-component of the anisotropy when measured on both sides of the sun - earth line. A difference of about 2 per cent was found in the spread of observed anisotropy components, but this could be due to the chance occurrence of two periods of large anisotropies. Consequently, data from both Region 1 and Region 2 are included in the final data set.

D. Prompt Solar Events

In order to study periods between prompt events, prompt events must be identified and eliminated from the data set. This is done in

two ways. First, periods when the PLO rate is more than 0.3/second (a proton flux of 1.2/cm^2-sec-sr-MeV) are not included. This eliminates periods dominated by large prompt events. Second, individual prompt events are identified and days near the beginning of the observed increase are eliminated. Prompt events are identified by their sharp increases in flux, typically a factor of 10 in 12 hours. Corroborative characteristics are large peak fluxes, velocity dispersion, exponential decay, and an accompanying prompt electron event. Anisotropy data are not used. Table V-1 lists the 25 prompt events identified for the period 72/273 to 74/2. The day preceding the sharp increase, the day of the sharp increase, and the two days following the sharp increase are not used in this study. Only whole days are eliminated. Rejecting these periods eliminates the beginnings of prompt events even though the PLO rate may not have reached 0.3/second. Small prompt events are also eliminated. The day previous to the sharp increase is eliminated to avoid possible small injections preceding the main injection of particles at the sun.

Table V-1. Onsets of Prompt Events, 72/273 - 74/2.

YEAR	DAYS
1972	282, 291, 303, 329, 333, 348, 351.
1973	46, 71, 78, 89, 102, 114, 119, 154, 171, 180, 210, 250, 261, 270, 277, 292, 307, 310.

VI. RESULTS

A. Introduction

The observed anisotropy of D2 analyzed events has been determined according to the procedure discussed in Chapter IV. D2 analyzed events are nominally 1.3 to 2.3 MeV protons. The periods used have been selected according to the criteria discussed in Chapter V. The criteria eliminate periods dominated by prompt solar events.

Both observed and diffusive anisotropies are used. The diffusive anisotropy was defined in Chapter III:

$$\vec{\xi}_{DIF} = \vec{\xi}_{OBS} - \frac{3C\vec{V}}{w} .$$

For small anisotropies, the diffusive anisotropy is the anisotropy in the rest frame of the solar wind (Forman, 1970; Balogh, et al., 1973).

The observed anisotropy is displayed using the Solar Ecliptic coordinate system. The diffusive anisotropy is displayed using both the Solar Ecliptic coordinate system and what will be termed the Magnetic Ecliptic system. The Magnetic Ecliptic system is obtained by rotating the Solar Ecliptic system about its z-axis until the new x-axis is colinear with the direction of the projection of the observed magnetic field onto the ecliptic plane. The Magnetic Ecliptic system is used to display the importance of the magnetic field direction on the diffusive anisotropy. Because particle propagation is independent of the sense of the magnetic field, there is an arbitrary choice in the sense of the x-axis. The positive x-axis is defined to be within 90° of 315° (the long-term average magnetic field direction) in Solar Ecliptic coordinates. The y-axis is chosen to form a right-handed coordi-

nate system. The new x- and y- axes are referred to as $\varkappa_{\parallel}$ and $\varkappa_{\perp}$ respectively; the projection of the diffusive anisotropy onto these axes are designated $\xi_{\parallel}$ and $\xi_{\perp}$ (see Figure VI-1).

The Magnetic Ecliptic coordinate system is constructed so that particles flowing along the magnetic field lines toward the sun nominally produce a positive $\xi_{\parallel}$. However, when the observed field direction is nearly perpendicular to the long-term average field direction, it is not certain which direction along the field leads to the sun. The direction nearest is used, but may not be correct. If incorrect, a positive $\xi_{\parallel}$ would correspond to flow away from the sun. Of the periods used when PLO is between 0.01/second and 0.3/second, only 7 percent have field directions differing by more than 75^{o} from the long term average.

B. 6-Hour Average Anisotropy

The observed anisotropies are plotted in Figure VI-2. The diffusive anisotropies for the same 112 periods are shown in Figures VI-3 and VI-4 using the Solar Ecliptic and Magnetic Ecliptic coordinate systems respectively. The PLO rate for each period included is greater than 0.03/second and less than 0.3/second.

The mean values for each of the groups are:

	$\vec{\xi}_{OBS}$ (%)		$\vec{\xi}_{DIF}$ (%)			
	S.E.	χ_{ν}	S.E.	χ_{ν}	M.E.	χ_{ν}
$\langle\xi_x\rangle$	-7.0±0.5	2.4	13.6±0.5	2.5	10.7±0.5	3.2
$\langle\xi_y\rangle$	-1.7±0.5	2.2	-3.1±0.5	2.2	1.3±0.5	2.0

Weighted means are used -- each data point is weighted according to the statistical uncertainty in the anisotropy measurement. The error

Figure VI-1

The upper panel shows the ecliptic plane as viewed from the North Ecliptic Pole. The x-axis and the y-axis of the Solar Ecliptic coordinate system are shown. The bottom panel shows the rotation of the Solar Ecliptic coordinate system about the z-axis used to define the Magnetic Ecliptic coordinate system. The axes of the Magnetic Ecliptic system are parallel to and perpendicular to the projection of the magnetic field onto the ecliptic plane.

COORDINATE SYSTEMS

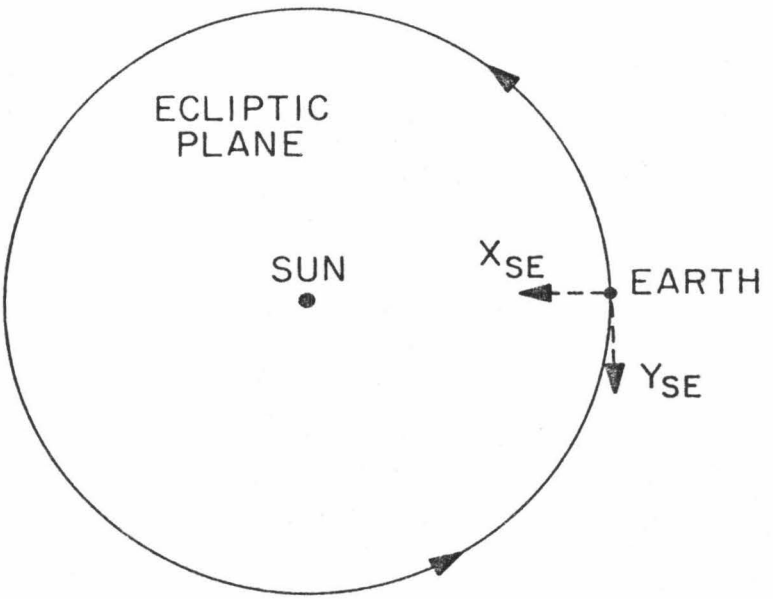

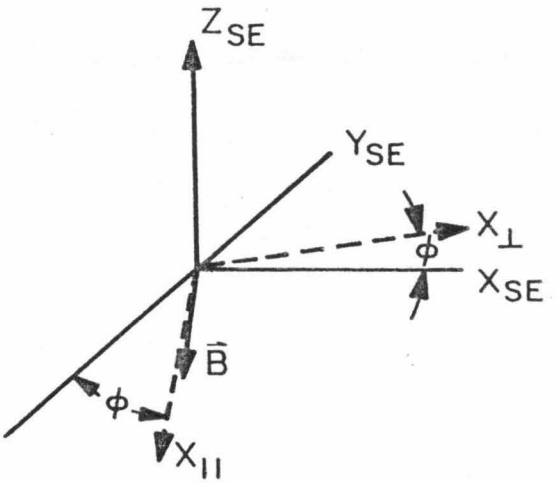

Figure VI-2

The observed anisotropy, $\vec{\xi}_{OBS}$, using Solar Ecliptic coordinates. Each dot represents one 6-hour period. A typical $\pm 1\sigma$ error bar is indicated as well as the means of the x- and y-components of the anisotropy.

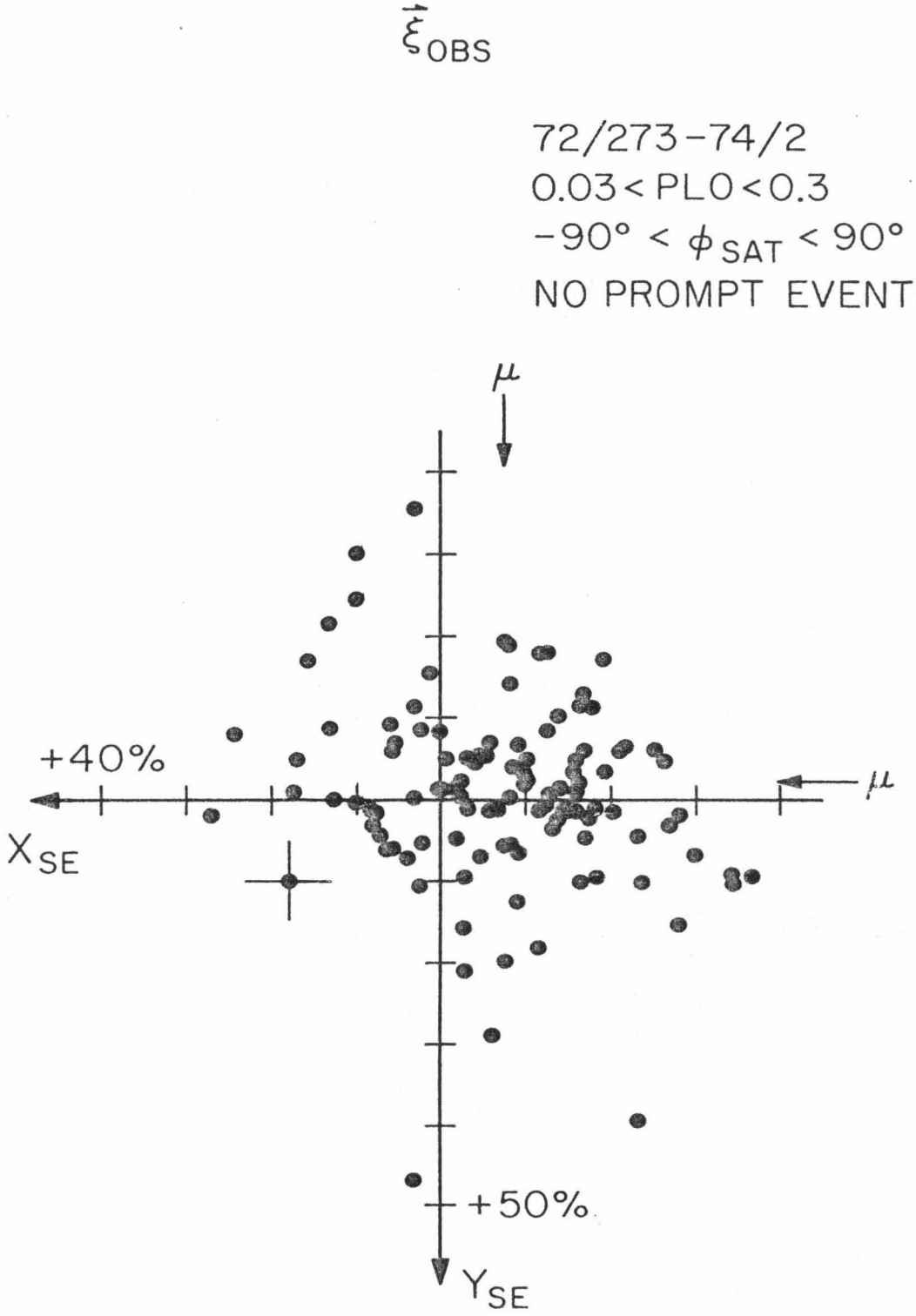
$\vec{\xi}_{OBS}$
72/273-74/2
0.03 < PLO < 0.3
$-90° < \phi_{SAT} < 90°$
NO PROMPT EVENTS
μ
+40%
μ
X_{SE}
+50%
Y_{SE}

Figure VI-3

The diffusive anisotropy, $\vec{\xi}_{DIF}$, using Solar Ecliptic coordinates. Each dot represents one 6-hour period. A typical $\pm 1\sigma$ error bar is indicated as well as the means of the x- and y-components of the anisotropy.

$\vec{\xi}_{DIF}$

72/273-74/2
$0.03 < PLO < 0.3$
$-90° < \phi_{SAT} < 90°$
NO PROMPT EVENTS

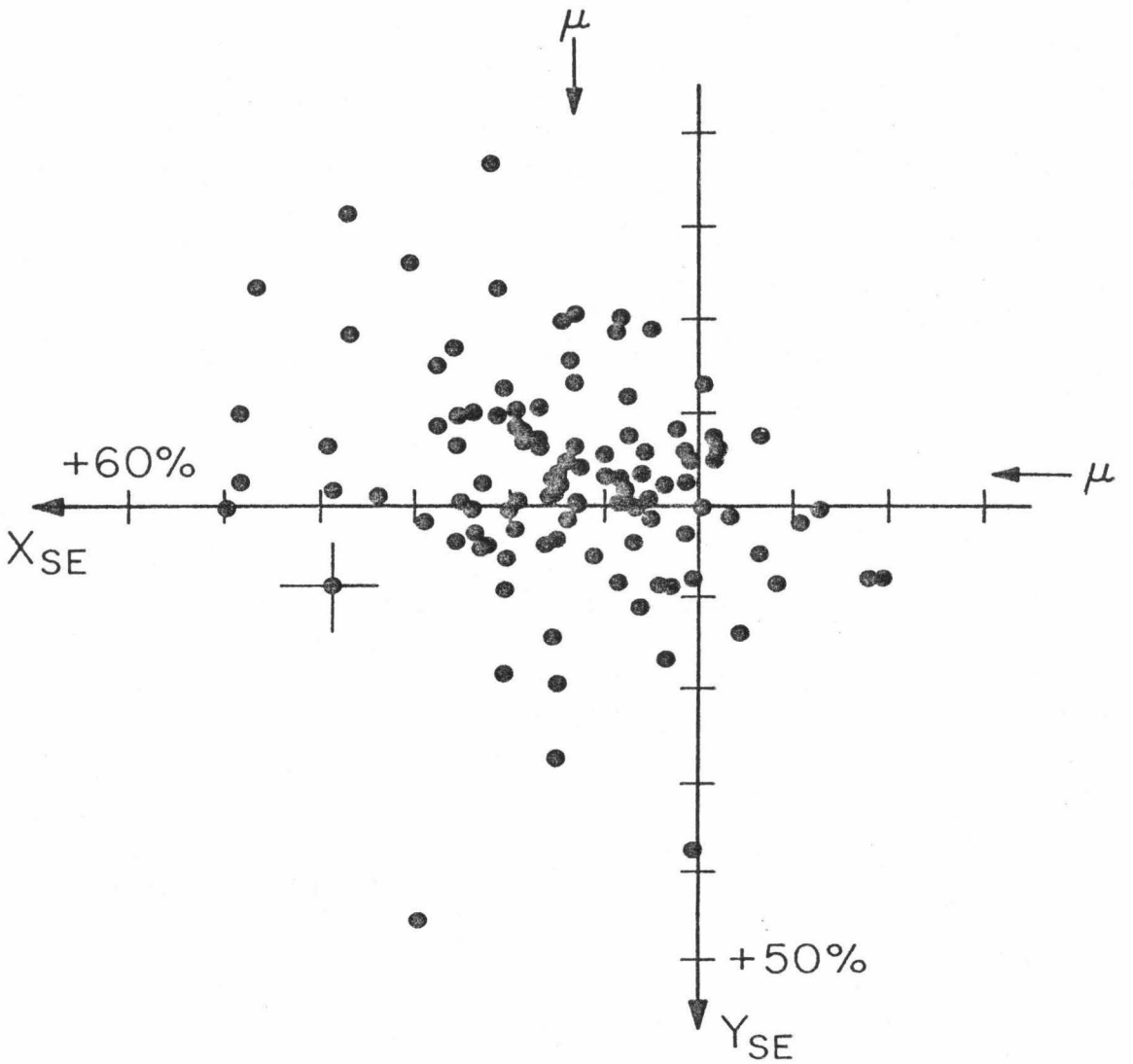

Figure VI-4

The diffusive anisotropy, $\vec{\xi}_{DIF}$, using Magnetic Ecliptic coordinates. Each dot represents one 6-hour period. A typical $\pm 1\sigma$ error bar is indicated as well as the means of $\xi_{\parallel}$ and $\xi_{\perp}$.

$\vec{\xi}_{DIF}$

72/273-74/2
$0.03 < PLO < 0.3$
$-90° < \phi_{SAT} < 90°$
NO PROMPT EVENTS

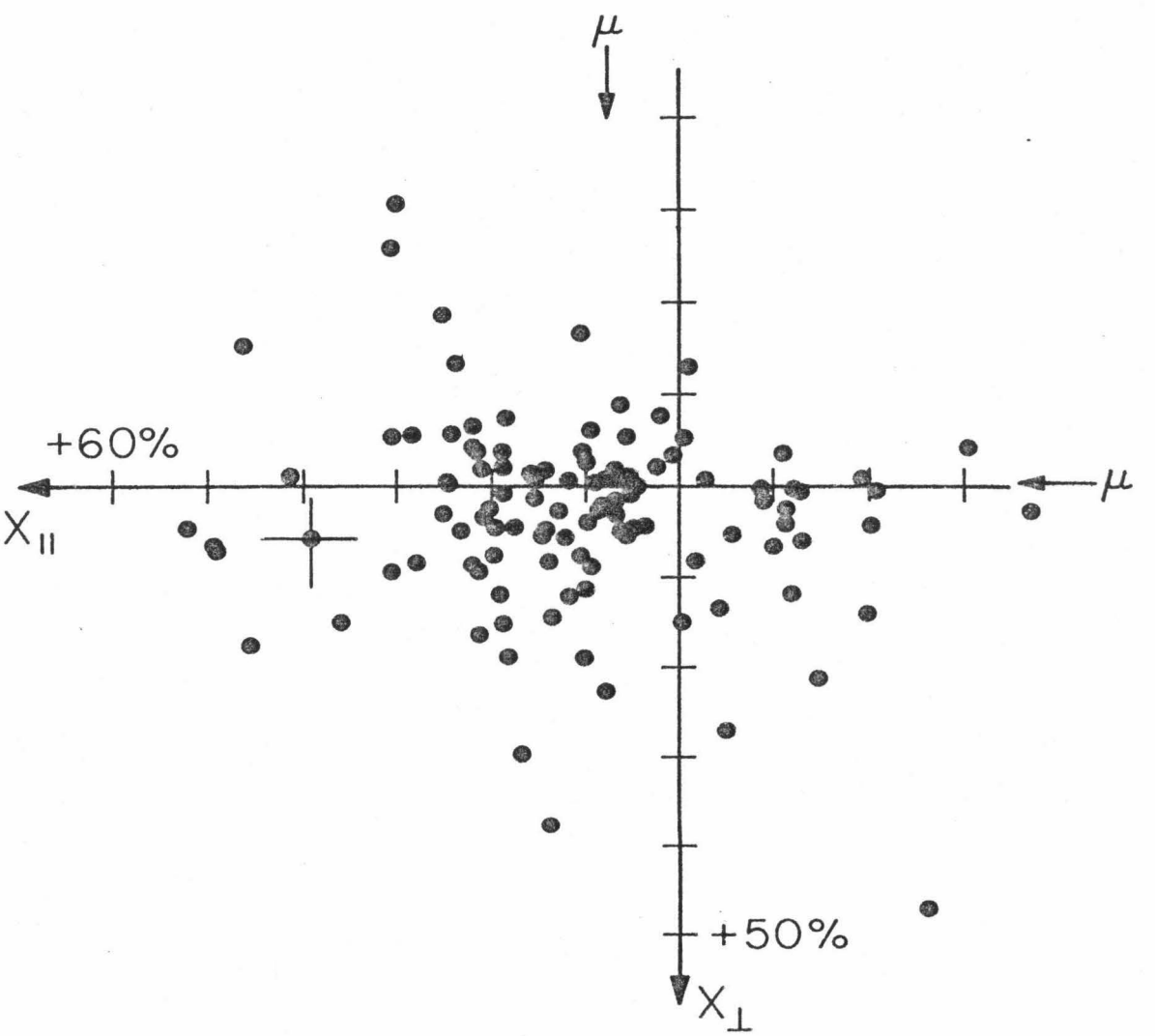

bars quoted on the means are determined from the statistical uncertainties in the individual measurements. The χ_ν's being larger than 1.0 indicates that the typical statistical uncertainty in each measurement of ~ 5 per cent is smaller than the real variation in the observations. Thus, a better estimate of the uncertainty in the mean is given by the product of the quoted error bars and χ_ν. The convention is adopted that unless the χ_ν of the fit is explicitly stated, quoted error bars will have been multiplied by χ_ν.

The typical $\vec{\xi}_{OBS}$ is away from the sun in a direction slightly counterclockwise from radial. The typical radial component is ~ 7 per cent. The diffusive anisotropy is qualitatively different from the observed anisotropy with the typical flow back toward the sun with a radial component of $\sim$ 14 per cent. The mean $\xi_\parallel$ is somewhat smaller than the mean $\xi_{DIF,x}$. This is due to the larger number of periods having a negative $\xi_\parallel$ than having a negative $\xi_{DIF,x}$.

Equation (3-4) relates the diffusive anisotropy to gradients in the particle density. The typical diffusive flow back toward the sun indicates that the typical radial gradient is positive -- a larger density beyond 1 AU than inside 1AU. In fact, 86 of the 112 periods (77 per cent) included in Figure VI-4 have a positive $\xi_\parallel$. Two effects could systematically bias this percentage. First, large statistical uncertainties in the individual measurements tend to make the periods evenly split between positive and negative $\xi_\parallel$. However, if the distribution of values around the mean of 10.7 per cent were all due to the typically 5 per cent statistical uncertainty in the individual measurements, only 2 of the periods would have a negative $\xi_\parallel$. The other

possible effect is the mis-identification of which direction along the magnetic field leads toward the sun. Such a mis-identification assigns the wrong sign to $\xi_{\parallel}$. This mis-identification is most likely when the field is far from its long-term average direction. A larger fraction of the periods with negative $\xi_{\parallel}$ than those with positive $\xi_{\parallel}$ have magnetic field directions more than 45^{o} from the long-term average direction. Sixteen of the 26 periods with flow away from the sun have such a field, and 16 of the 86 periods with flow toward the sun have such a field. Of the 32 periods with a magnetic field direction more than 45^{o} from the long-term average direction, 12 either are associated with magnetic field sector boundaries or have field directions opposite the current sector's prevailing field direction. Eliminating these 12 periods from consideration increases the 77 per cent quoted above to 82 per cent. A nominal value of 80 per cent will be used in Chapter VII. Eliminating these 12 periods also increases $\langle \xi_{\parallel} \rangle$ and $\langle \xi_{\perp} \rangle$ to 12.1 per cent and 1.8 per cent, respectively. These increases are comparable to the statistical uncertainties in these values.

C. The Diffusive Anisotropy

The dependence of the diffusive anisotropy on various parameters is now investigated. From eq. (3-4),

$$\vec{\xi}_{DIF} = (-\frac{3}{w}) \underline{\underline{\kappa}} \cdot (\nabla U/U) \quad . \tag{6-1}$$

Although $\underline{\underline{\kappa}}$ and ∇U are not known, eq. (6-1) does suggest what quantities might affect $\vec{\xi}_{DIF}$.

1. Flux Dependence. Figure VI-5 contains histograms of $\xi_{\parallel}$ for 4 groups of data selected by the PLO rate. PLO rates from 0.003/second to 0.3 second are included. The weighted means of the distributions are:

PLO	periods	$\langle \xi_{\parallel} \rangle$ (%)	± (%)
0.1 - 0.3	24	5.4	2.8
0.03 - 0.1	88	11.9	1.9
0.01 - 0.03	100	10.0	1.7
0.003 - 0.01	105	15.4	2.6

The weighted mean for the 4 groups is 10.8 per cent. There is a 5 to 10 per cent chance of the variations from the mean being as large as observed due to statistical fluctuations. Thus, there may be a statistically significant flux dependence to the anisotropy. However, the typical diffusive streaming is back toward the sun for all the groups, indicating streaming toward the sun to be typical for a wide range of low-energy proton intensity.

2. Time Since Most Recent Prompt Event. Prompt solar events can dominate low-energy proton fluxes at 1 AU for several days. Periods dominated by prompt events have been eliminated from this study by the criteria discussed in Chapter V. Prompt events could have some influence on gradients and thus diffusive anisotropies for longer periods. For example, McKibben (1972) has reported decay times as long as 87 hours late in some prompt events after an initial decay time of $\sim$ 24 hours.

To investigate possible influence, $\xi_{\parallel}$ is plotted in Figure VI-6 as a function of the elapsed time, Δt, since the onset of the most recent identified prompt event. The onset times of prompt events have

Figure VI-5

The distributions of $\xi_{\|}$ for four intervals of the PLO rate. The typical $\pm 1\sigma$ error bar for an individual measurement is indicated for each group. The mean $\xi_{\|}$ for each group is also indicated.

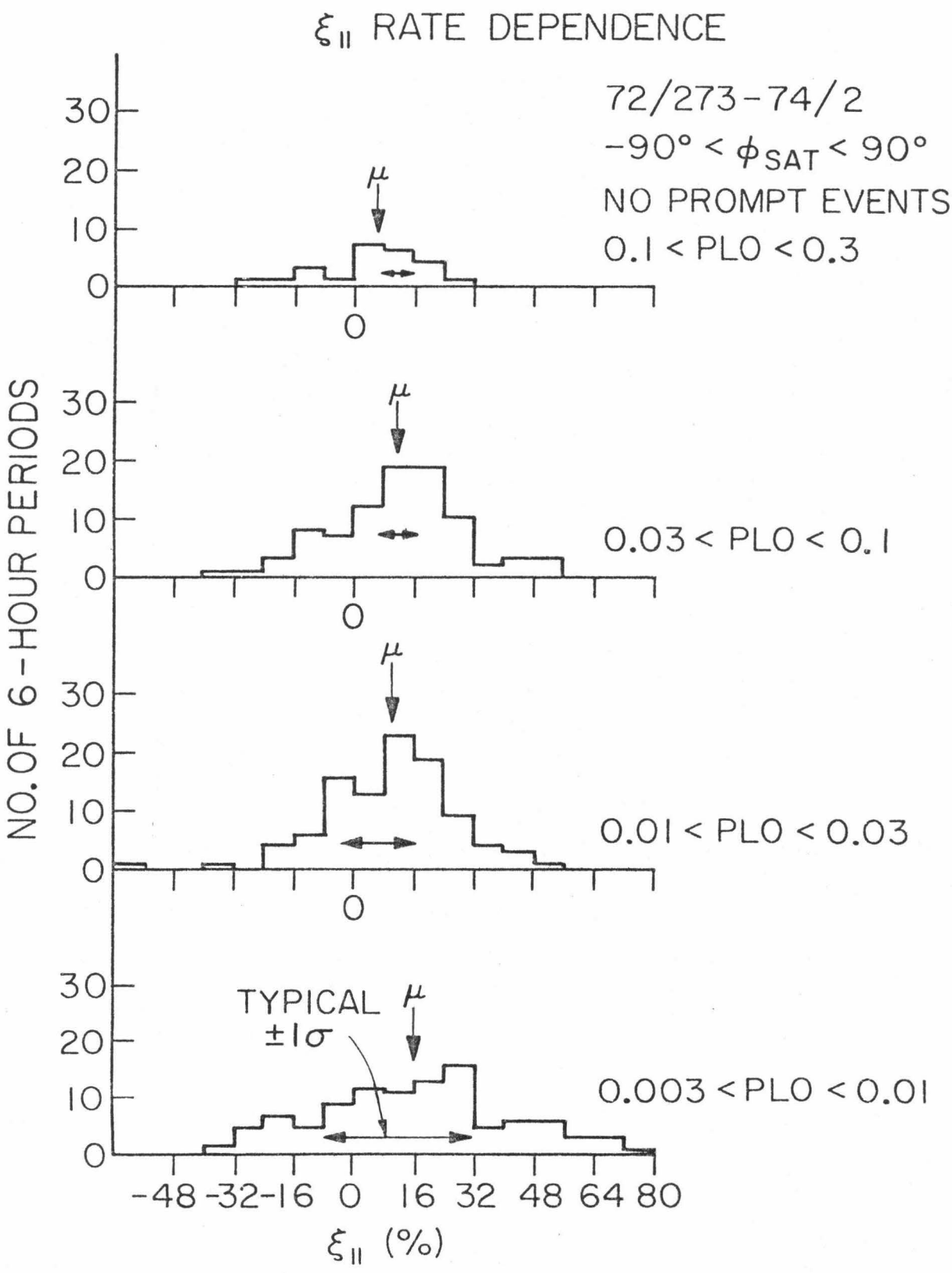
ξ_{11} RATE DEPENDENCE
72/273-74/2
$-90° < \phi_{SAT} < 90°$
NO PROMPT EVENTS
0.1 < PLO < 0.3
0.03 < PLO < 0.1
0.01 < PLO < 0.03
0.003 < PLO < 0.01
TYPICAL ±1σ
μ
NO. OF 6-HOUR PERIODS
30
20
10
0
-48 -32 -16 0 16 32 48 64 80
ξ_{11} (%)

Figure VI-6

The dependence of $\xi_{\parallel}$ on the number of days since the onset of the most recent identified prompt event. A typical $\pm 1\sigma$ error bar is shown. The dashed line is the least squares fit to the data.

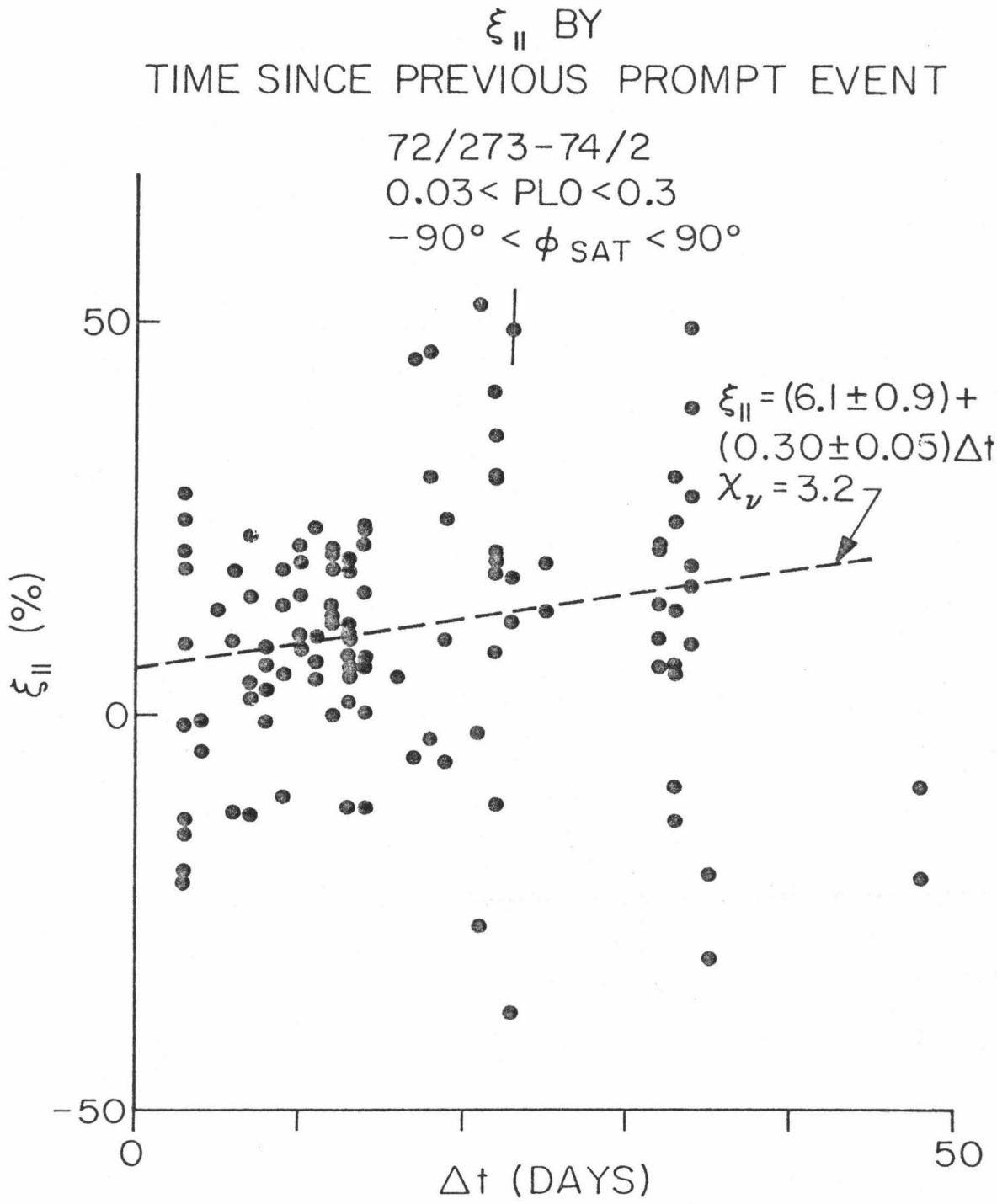
$\xi_{\parallel}$ BY
TIME SINCE PREVIOUS PROMPT EVENT
72/273-74/2
0.03< PLO <0.3
$-90° < \phi_{SAT} < 90°$
$\xi_{\parallel} = (6.1 \pm 0.9) +$
$(0.30 \pm 0.05)\Delta t$
$\chi_\nu = 3.2$
50
0
-50
$\xi_{\parallel}$ (%)
0
50
Δt (DAYS)

been listed in Table V-1. The scatter in the data appears larger than any trend, indicating that Δt is not a dominant factor in determining $\xi_{\parallel}$. A linear fit to the data:

$$\xi_{\parallel}(\%) = (6.1 \pm 0.9) + (0.30 \pm 0.05)\Delta t \qquad \chi_{\nu} = 3.2 \qquad (6\text{-}2)$$

where Δt is in days, shows a small trend toward a larger anisotropy for larger Δt, although the large χ_{ν} means the fit is poor. The line determined by eq. (6-2) is positive for all values of Δt greater than 0, indicating that the typical diffusive anisotropy is toward the sun for all Δt included in the data set.

3. Magnetic Field Direction. As discussed in Chapter III, the magnetic field is understood to control the diffusion of particles in interplanetary space and thus affect $\vec{\xi}_{DIF}$. For example, if $(\varkappa_{\perp}/\varkappa_{\parallel}) \ll 1$, then $\vec{\xi}_{DIF}$ will be parallel to the magnetic field direction, ϕ_B. On the other hand, if $\varkappa_{\perp} = \varkappa_{\parallel}$ (isotropic diffusion), then $\vec{\xi}_{DIF}$ should be independent of ϕ_B.

To investigate the relative size of $\varkappa_{\perp}$ and $\varkappa_{\parallel}$, the direction of the diffusive anisotropy, ϕ_{DIF}, has been plotted as a function of ϕ_B and a linear fit made to the data. Both the field and the anisotropy are 6-hour averages. The fit is complicated by the independence of the streaming on the sense of the field direction. Consequently, ϕ_B has been restricted to a 180° range by the following mapping:

$$\phi_B = \begin{cases} \phi_{OBS} & \text{for} \quad -90^{\circ} < \phi_{OBS} < 90^{\circ} \\ \phi_{OBS} + 180^{\circ} & \text{for} \quad \phi_{OBS} < -90^{\circ} \\ \phi_{OBS} - 180^{\circ} & \text{for} \quad \phi_{OBS} > 90^{\circ} \end{cases}$$

where ϕ_{OBS} is the observed field direction.

A linear relationship between ϕ_{DIF} and ϕ_B is assumed:

$$\phi_{DIF} = a + b\,\phi_B \equiv f(\phi_B) \ .$$

If diffusion is isotropic, b is expected to be consistent with 0. For field-aligned $\vec{\xi}_{DIF}$, a = 0 and b = 1. The parameters of the fit -- a and b -- are determined by minimizing

$$\chi^2 = \Sigma\left[\frac{\mathrm{DIST}\left(\phi_{DIF,\,i},\ f(\phi_{B,\,i})\right)}{\sigma_{\phi_{DIF,\,i}}}\right]^2 \ ,$$

where i indexes the individual data points and the distance measure is given by

$$\mathrm{DIST}(\phi_1, \phi_2) = (\phi_1 - \phi_2)_{\bmod 180^\circ} \qquad (6\text{-}3)$$

and the range of DIST is $[-90^\circ, +90^\circ)$. The statistical errors in the parameters are estimated by the change required to increase χ^2 by 1. The optimal parameters were determined by a grid search technique. The best fit is

$$\phi_{DIF} = (-10.2^\circ \pm 1.3^\circ) + (0.71 \pm 0.03)\,\phi_B \qquad (6\text{-}4)$$

$$\text{with } \chi_\nu = 2.2$$

Figure VI-7 contains two panels. One panel is of ϕ_{DIF} versus ϕ_B; in the other panel, the diffusive anisotropy directions have been replotted to show their distances [eq. (6-3)] from the best fit [eq. (6-4)].

The strong dependence of the diffusive anisotropy direction on the magnetic field direction shown by eq. (6-4) indicates that diffusion is not isotropic, so that $\varkappa_\perp$ is less than $\varkappa_\parallel$. The slope of the line determined by eq. (6-4) being less than 1 suggests that $\varkappa_\perp$ is not negligibly small. The value of $(\varkappa_\perp/\varkappa_\parallel)$ consistent with the data depends on the relative gradients parallel to and perpendicular to the field lines.

Figure VI-7

The left panel shows the direction of the diffusive anisotropy as a function of the magnetic field direction. The data are replotted in the right panel and the least squares fit is indicated by the dashed line. Points which would have been plotted outside the solid lines have had $+180^{o}$ or -180^{o} added to their anisotropy direction. A typical $\pm 1\sigma$ error bar in the anisotropy direction is indicated.

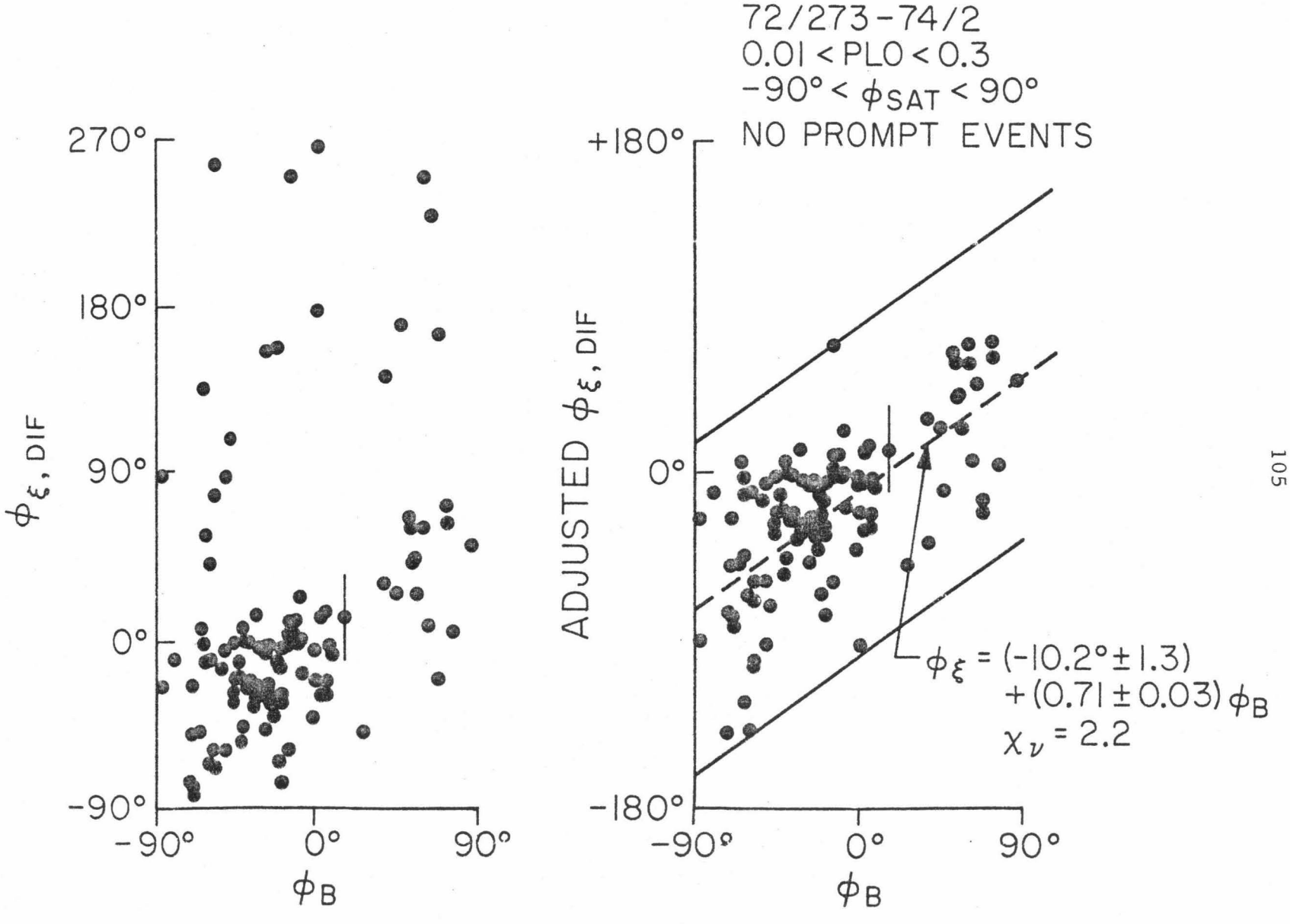
72/273-74/2
0.01 < PLO < 0.3
-90° < φSAT < 90°
NO PROMPT EVENTS
270°
180°
90°
0°
-90°
φε, DIF
-90°
0°
90°
φB
+180°
0°
-180°
ADJUSTED φε, DIF
φε = (-10.2° ± 1.3)
+ (0.71 ± 0.03) φB
χν = 2.2
-90°
0°
90°
φB

The determination of the value will require further study.

4. Magnetic Field Fluctuations. As seen in eq. (6-1), the size of the diffusion tensor could affect $\vec{\xi}_{DIF}$. The work of Jokipii (1966) relates $\underline{\underline{\kappa}}$ to fluctuations in the magnetic field with wavelengths comparable to the particle's Larmor radius. As discussed in Chapter III, the exact relationship is still a subject of controversy. This study has sufficient information only to estimate the amount of turbulence in the magnetic field over a wide range of frequencies. The magnetic field data used in this work are based on hourly averages provided by the National Space Science Data Center. These hourly averages are in turn derived from averages of even finer time scales which range from 1.3 to 48 seconds, depending on which experimenter's data are used. The standard deviation σ_B in the fine time scale averages used to determine the hourly average field is a measure of the fluctuations in the magnetic field with frequencies between $\sim(1\ \text{sec})^{-1}$ to $\sim(1\ \text{hour})^{-1}$. The frequency appropriate for $1\frac{1}{2}$ MeV protons is $\sim(70\ \text{sec})^{-1}$. A dimensionless variable is given by B/σ_B for each hour. Figure VI-8 is a plot of the average of the hourly B/σ_B versus the amplitude of the diffusive anisotropy, and the best linear fit to the data. In view of the large χ_ν, the difference of the slope from 0 is not considered significant.

This result is consistent with a diffusive anisotropy independent of the magnitude $\underline{\underline{\kappa}}$, but the necessarily crude method for estimating $\underline{\underline{\kappa}}$ prevents any definitive determination.

5. Solar Wind Velocity. The solar wind velocity is an important parameter in particle propagation, so changes in the velocity

Figure VI-8

The dependence of the amplitude of the diffusive anisotropy on the relative fluctuations in the magnetic field. A typical $\pm 1\sigma$ error bar in the amplitude of the anisotropy is indicated. The dashed line is the least squares fit to the data.

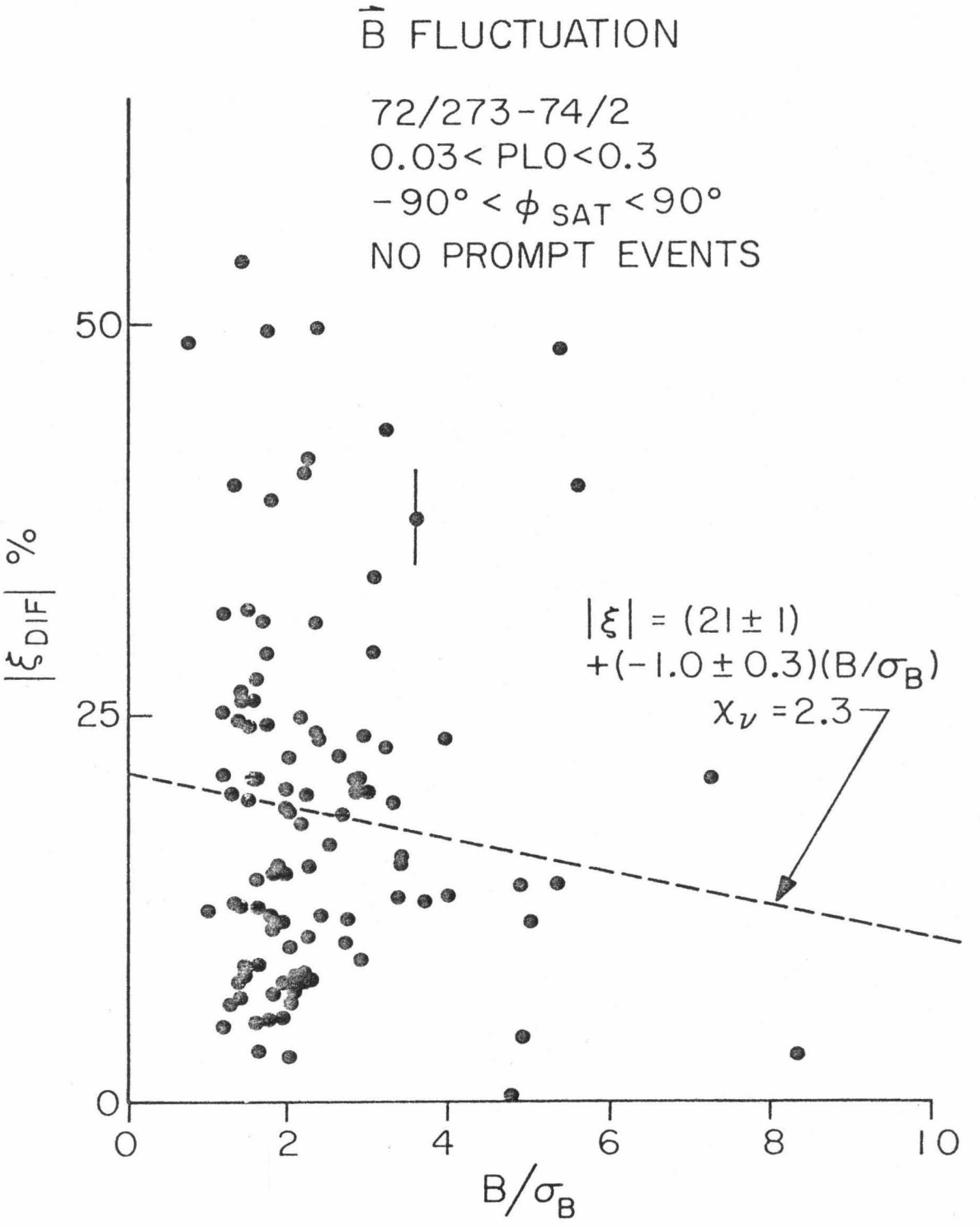
$\vec{B}$ FLUCTUATION
72/273-74/2
0.03< PLO<0.3
$-90° < \phi_{SAT} < 90°$
NO PROMPT EVENTS
$|\xi| = (21 \pm 1)$
$+(-1.0 \pm 0.3)(B/\sigma_B)$
$\chi_\nu = 2.3$
$|\xi_{DIF}|$ %
50
25
0
0
2
4
6
8
10
B/σ_B

could alter spatial gradients and thus the diffusive anisotropy. Figure VI-9 plots $\vec{\xi}_{DIF}$ for 4 groups of solar wind velocity. The components are:

V_{SW} (km/sec)	Periods	$\langle \xi_x \rangle$ (%)
< 400	87	7.8 ± 1.5
400 - 500	69	15.7 ± 1.5
500 - 600	48	14.7 ± 1.6
> 600	8	17.8 ± 3.8

The extreme velocities used are 270 km/sec and 660 km/sec. The variation in the mean is statistically significant for the x-component, indicating an increased streaming toward the sun for periods with large solar wind velocities. A model consistent with such a correlation will be presented in Chapter VII.

D. Particle Flow

As noted in Section VI-A, the diffusive anisotropy is the anisotropy in the rest frame of the solar wind for small anisotropies. The particles are also being convected with the solar wind, so the anisotropy determined by the actual particle flow is given by

$$\vec{\xi}_{part} = \vec{\xi}_{DIF} + \frac{3\vec{V}}{w} \quad .$$

This differs from the observed anisotropy in that the convective term is not multiplied by the Compton - Getting factor. The Compton-Getting factor corrects for the difference in energy as a function of direction and so is not appropriate for the actual flow of particles.

Figure VI-10 is a histogram of the x-component of $\vec{\xi}_{part}$. The mean value, weighted by the intensity PLO, is

Figure VI-9

The diffusive anisotropy, $\vec{\xi}_{DIF}$, using Solar Ecliptic coordinates for periods grouped by the solar wind speed. Typical $\pm 1\sigma$ error bars are shown. The means of the x- and y-components of the anisotropy are indicated.

$\vec{\xi}_{DIF}$

72/273-74/2
$0.01 < PLO < 0.3$
$270 < V_{SW} < 400$
$-90° < \phi_{SAT} < 90°$

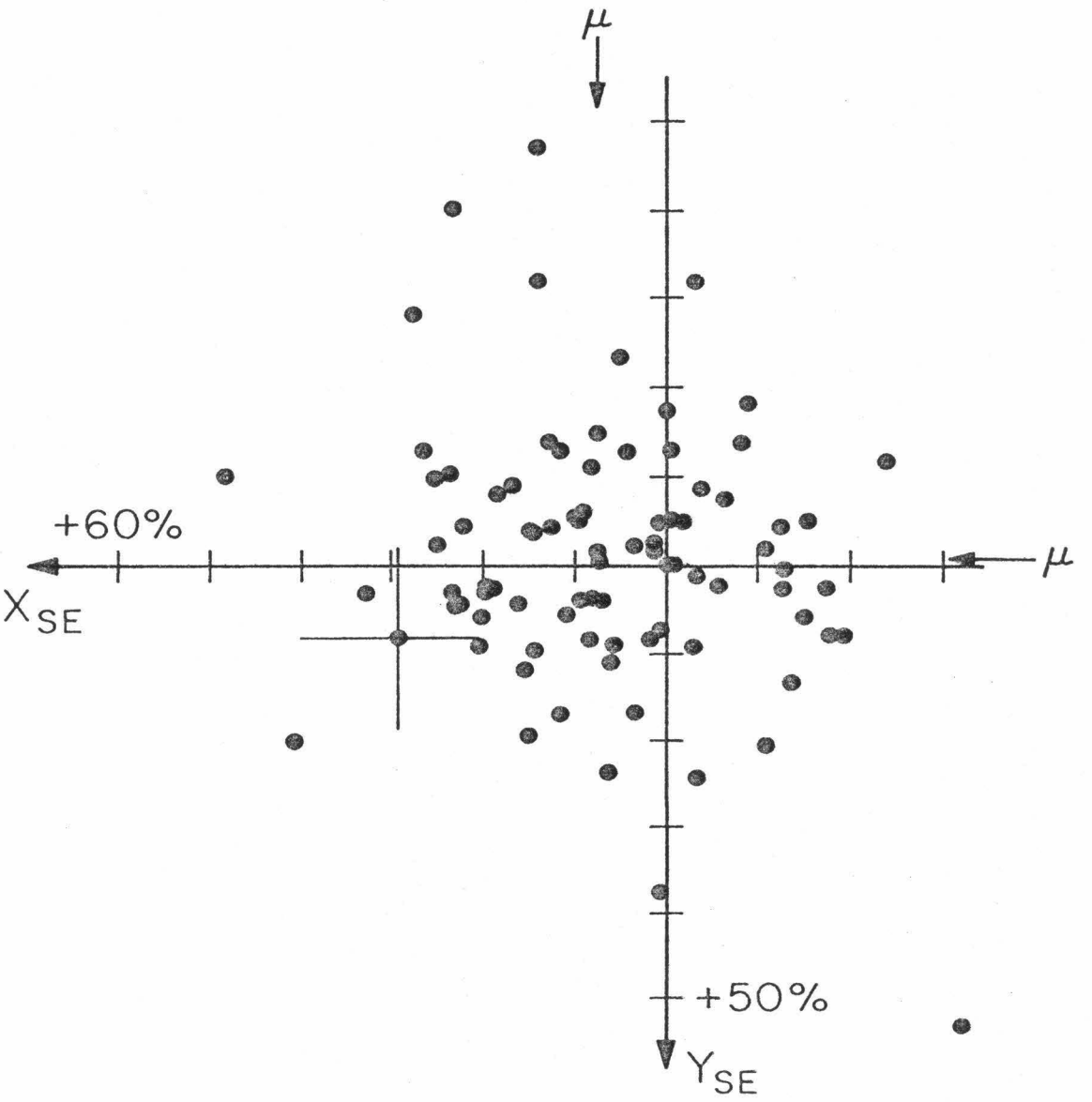

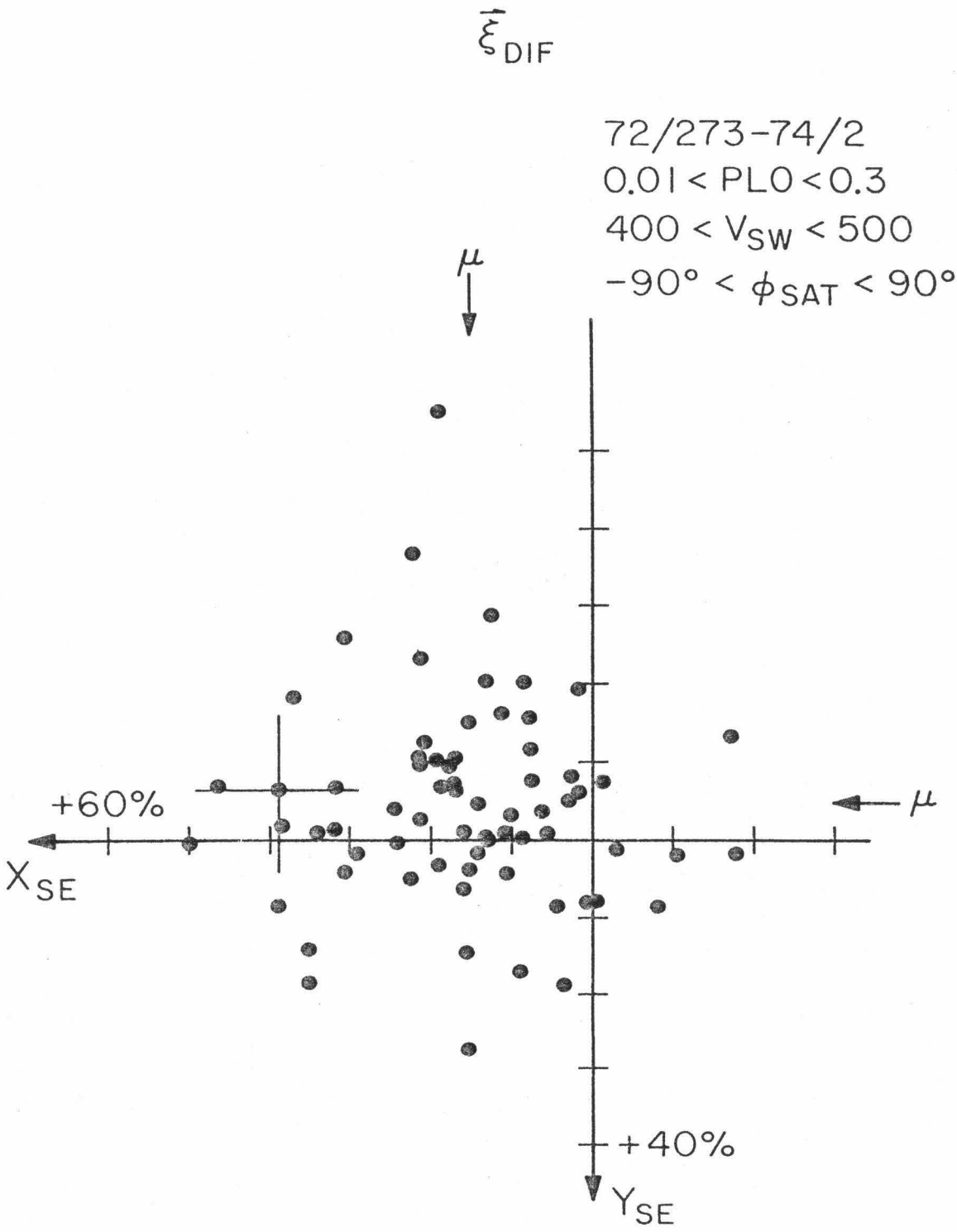
$\vec{\xi}_{DIF}$
72/273-74/2
0.01 < PLO < 0.3
400 < V_{SW} < 500
-90° < ϕ_{SAT} < 90°
μ
μ
+60%
X_{SE}
+40%
Y_{SE}

$\vec{\xi}_{DIF}$

72/273-74/2
$0.01 < PLO < 0.3$
$500 < V_{SW} < 600$
$-90° < \phi_{SAT} < 90°$

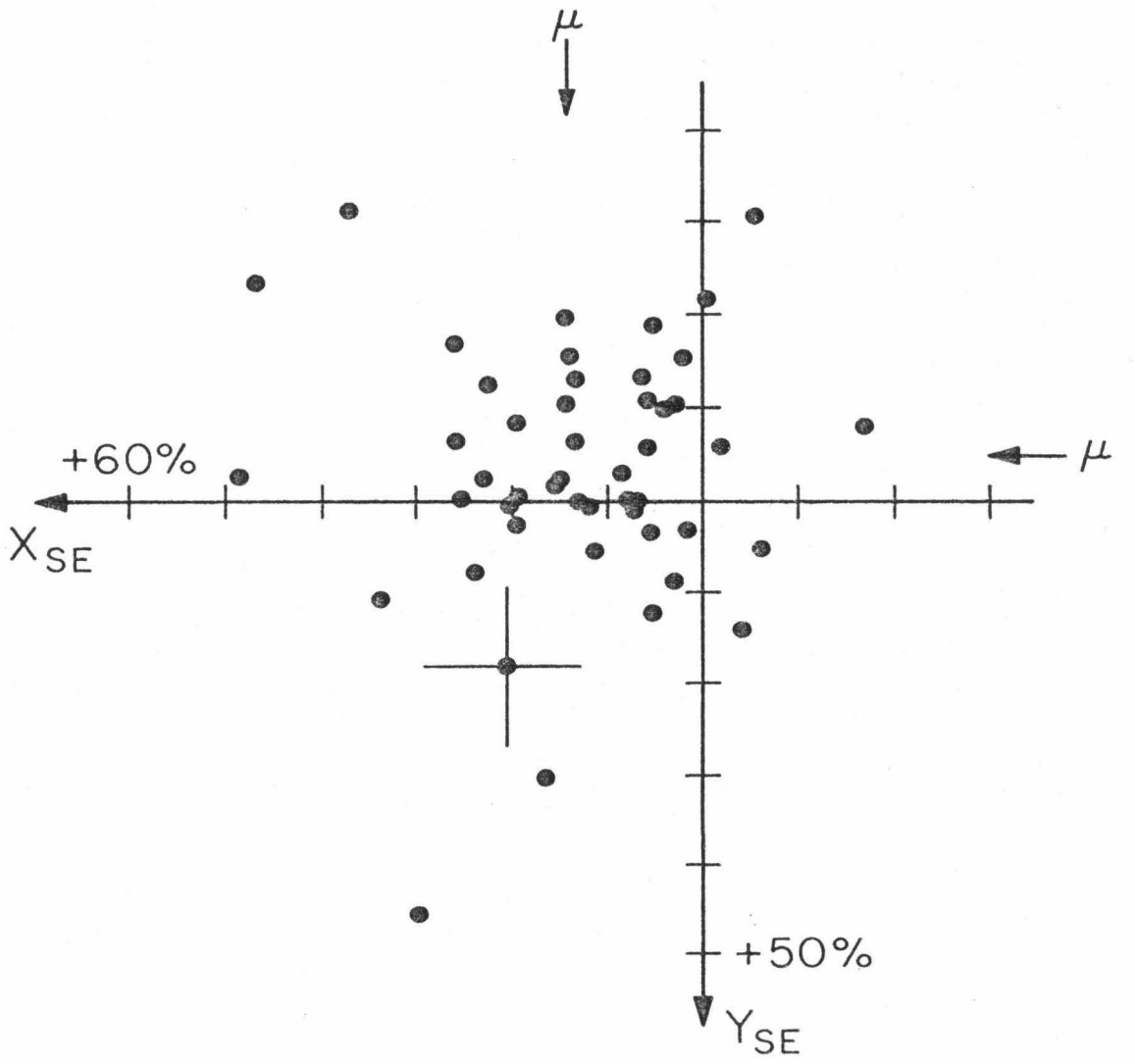

$\overrightarrow{\xi}_{DIF}$

72/273-74/2
$0.01 < PLO < 0.3$
$600 < V_{SW} < 700$
$-90° < \phi_{SAT} < 90°$

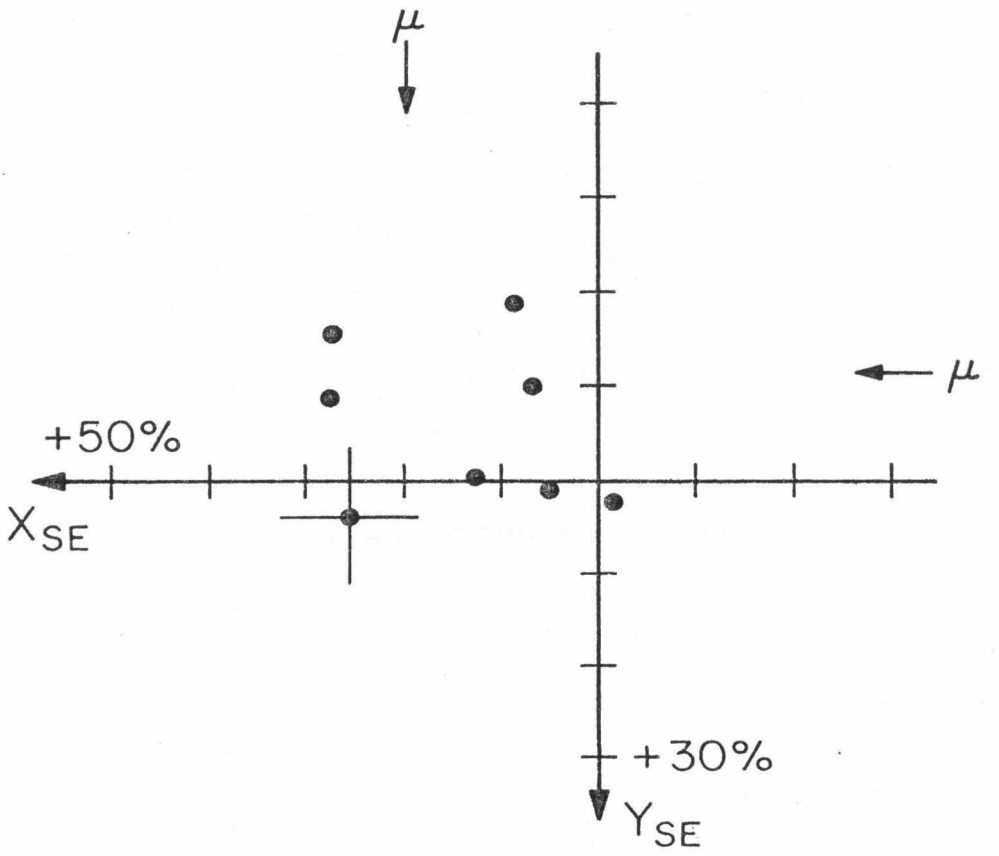

Figure VI-10

The distribution of the x-component of $\vec{\xi}_{particle}$. Positive values indicate particle flow toward the sun. The mean value, determined by weighting the individual values by PLO, is indicated.

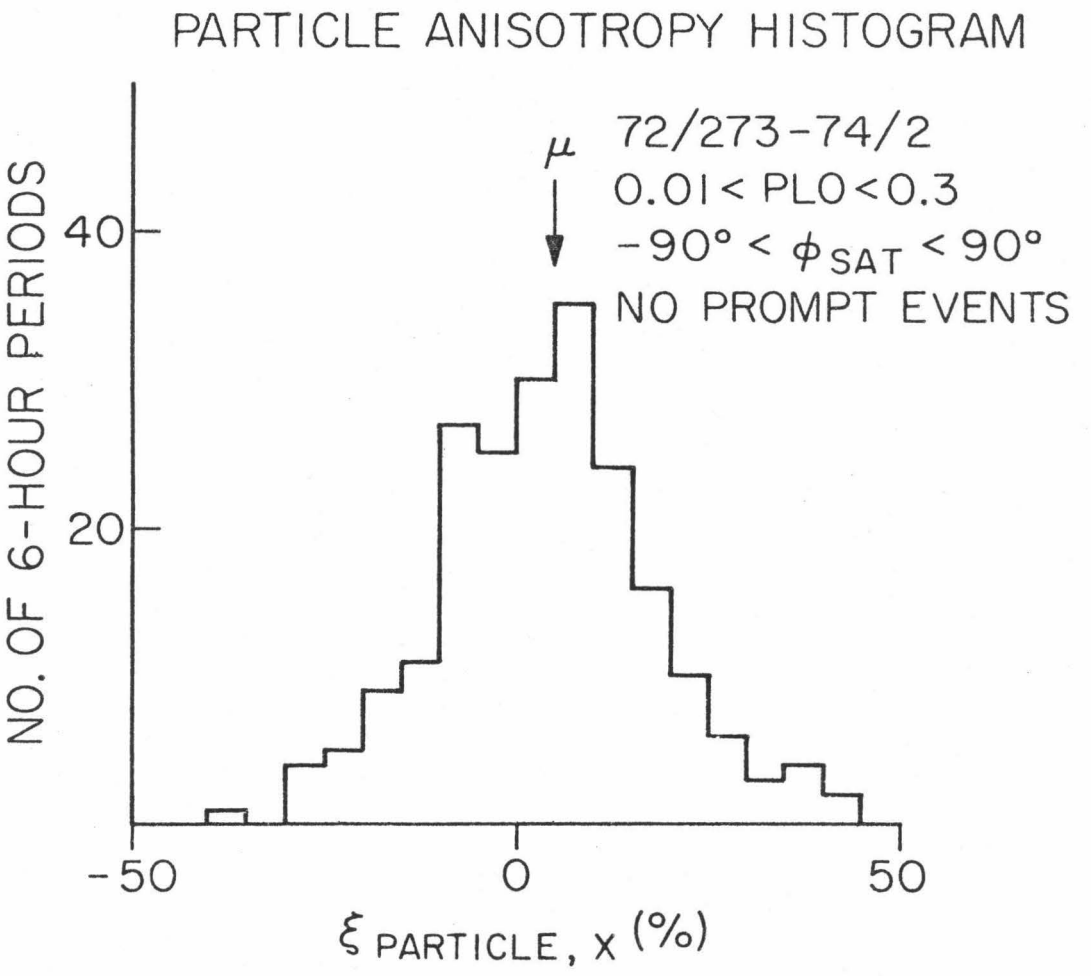
PARTICLE ANISOTROPY HISTOGRAM
μ
72/273-74/2
0.01 < PLO < 0.3
-90° < φ SAT < 90°
NO PROMPT EVENTS
NO. OF 6-HOUR PERIODS
40
20
-50
0
50
ξ PARTICLE, X (%)

$$\mu = \frac{\sum(\vec{\xi}_{part,x} \cdot PLO)}{\sum PLO} = 5.0\% \pm 0.5\% \ .$$

The average particle streaming is

$$\langle S_{part,x} \rangle = \frac{4\pi \langle (\xi_{part,x}) PLO \rangle}{3\,(\text{geometric factor})} = .052 \pm .005 \text{ particles/cm}^2\text{-sec}$$

between 1.2 and 2.4 MeV.

At an average particle energy of 1.6 MeV, this corresponds to an energy flux of 0.083 MeV/cm^2-sec flowing toward the sun.

For comparison, the energy flux in the bulk flow of the solar wind is $\sim 2 \times 10^5$ MeV/cm^2-sec. The energy flux in the interplanetary magnetic field is $\sim$ 1 per cent of this value. Thus, the energy flow of 1.2 to 2.4 MeV protons at 1 AU is only $\sim 4 \times 10^{-7}$ times as large as the solar wind bulk flow energy and $\sim 4 \times 10^{-5}$ times as large as the energy flux in the interplanetary magnetic field.

Interplanetary acceleration, perhaps at the interface of high- and low-speed solar wind streams, has been suggested by McDonald, et al. (1975) to explain increases in low-energy protons seen near 3 AU. Such acceleration could also be the source of the particles observed in this study. The relatively small energy flux of $\sim$ 1.6 MeV protons seen at 1 AU is consistent with the solar wind being the energy reservoir for the acceleration. A definitive energy balance study must await knowledge of the streaming at radial distances beyond the source of the particles as well as knowledge of the specific acceleration mechanism.

VII. DISCUSSION

A. Source

1. Spatial Gradient. The Caltech EIS experiment aboard IMP-7 has been used to measure the streaming of cosmic-ray protons in the energy interval 1.3 - 2.3 MeV during selected periods from September 1972 to January 1974. As discussed in Chapter V, the 6-hour periods were selected to study the times between prompt solar particle events. Statistically significant anisotropies could not be measured for individual periods at the lowest flux levels observed, so the periods used are during enhancements of the flux above quiet time levels. For 112 6-hour periods when the PLO rate was between 0.03 and 0.3/second, the amplitude of the average $\vec{\xi}_{OBS}$ was $\sim$ 7 per cent. The particles were observed to be streaming from the sun in a direction slightly counterclockwise from radial. The diffusive anisotropy has been determined by subtracting the convective anisotropy from the observed anisotropy. The average $\vec{\xi}_{DIF}$ had an amplitude of $\sim$ 12 per cent, with the flow toward the sun along the observed magnetic field direction. The flow along the field was toward the sun in $\sim$ 80 per cent of these periods. This flow back toward the sun was found to be typical of all the PLO rates used in this study -- from 0.003/second to 0.3/second.

The previously proposed models of delayed events seen near 1 AU, which were reviewed in Chapter I, involve continuous injection of $\sim$ 1 MeV particles into the interplanetary medium near the sun, thereby producing flow away from the sun.

Flow back toward the sun implies a positive radial gradient in

the particle density. Evidence of the existence of such a radial gradient, at least during certain periods, has been presented by McDonald, et al. (1975) on the basis of the average relative size of delayed events seen at 1 AU and at ~ 3 AU from November 1973 to April 1974. Whether the delayed events seen near 3 AU and the increases of the present study are the same phenomena has yet to be determined. The determination is made difficult by the small overlap in observing time and the separation in azimuthal position of the two spacecraft. In any case, some of the models proposed to explain the increases near 3 AU may be relevant to the anisotropies reported herein.

2. Interplanetary Acceleration. McDonald, et al. (1975) considered interplanetary acceleration the most likely explanation of the growth of delayed events with increasing radial distance. Fisk (1976) has developed numerical solutions to the Fokker-Planck propagation equation involving interplanetary acceleration to explain the observed increases. The particles are injected at low energies ($\ll$ 1 MeV) near the sun and are accelerated as they propagate through the interplanetary medium. Acceleration is assumed to take place throughout the solar cavity. The rate of acceleration is adjusted to produce an increase in the intensity by a factor of ~ 10 between 1 and 3 AU. Two acceleration processes are considered. The rate of the first process, Fermi-acceleration, is determined by the diffusion coefficient $\varkappa_{\parallel}$; a $\varkappa_{\parallel}$ of $\sim 1.8 \times 10^{19}$ cm^2/sec was needed to produce the desired radial gradient. Such a $\varkappa_{\parallel}$ produces a diffusive anisotropy at 1 AU of ~ 0.25 per cent. This value is ~ 50 times smaller than the typical anisotropy found in the present work. Thus,

the model is not consistent with the observations. The second acceleration process, transit-time damping, does not depend on $\kappa_{\|}$ and so cannot be tested by the anisotropy results reported in this work.

Acceleration may be taking place in localized regions rather than throughout the solar cavity. Pesses, et al. (1976) have presented evidence that the acceleration of protons in co-rotating shocks at the boundary between two solar wind streams is a common feature of interplanetary space at distances $\gtrsim$ 2.6 AU. Propagation along the boundary could spread the azimuthal extent of the particles as proposed by Gold and Roelof (1976) for Jovian electrons. Quantitative studies are needed to determine if such an acceleration mechanism can produce enough particles to account for the increases seen at 1 AU in 1973. A qualitative study of the energy requirements was discussed in Chapter VI. The energy flux in the solar wind was found to be $\sim 2 \times 10^6$ larger than the energy flux in particles at 1.2 to 2.4 MeV streaming toward the sun, indicating the solar wind to be a possible energy reservoir for interplanetary acceleration.

3. Out of the Ecliptic. Another mechanism to create a positive radial gradient is solar injection of protons at high solar latitude, propagation out of the ecliptic to beyond 1 AU, and eventual diffusion back toward the sun in the ecliptic plane. Since little is known about out of the ecliptic processes, this possibility cannot be eliminated.

4. Solar Flares. Another possible source for the increases seen by the Caltech experiment is solar flares, such as those which produce the prompt events but which, because of their different solar longitude, are not seen as prompt events. As discussed in Chapter I, the anisotropy observed late in prompt events is consistent with a

diffusive streaming back toward the sun. Thus, if early in the prompt event the observer were poorly connected to the source of particles, the characteristic sharp rise with streaming from the sun might not be observed. Then if later the observer became better connected to the event due to rotation of the sun, for example, the event could be in its decay phase with the diffusive streaming back toward the sun.

A simple model to produce this scenario divides particle-producing flares into two groups: those near 60^{o} West solar longitude which are directly connected to the observer and produce the prompt events, and those to the east which do not become well-connected until later in the event and produce delayed events. The model must be able to account for the relative number of prompt and delayed events. Twenty-five prompt events have been identified for the period included in the present study; they are listed in Table V-1. The diffusive anisotropy could be determined during the onset of 13 of these events. $\xi_{\parallel}$ was negative, indicating flow from the sun, for 10 of the 13 with values from -10 per cent to -100 per cent. For one period $\xi_{\parallel}$ was consistent with 0; for the two remaining periods there was a large flow toward the sun (40 per cent and 100 per cent). Thus, for the majority of these events, the diffusive anisotropy is consistent with the solar source hypothesized. Eleven of the 25 prompt events could be associated with a specific site of activity on the sun (Hurford, 1974). The site of the activity ranged from $E57^{o}$ to $W80^{o}$ solar longitude. Eight of the 11 were west of the central meridian. A typical maximum PLO rate for the 25 prompt events is ~ 0.5/second (i.e., $\sim 2/cm^{2}$-sec-sr-MeV).

The identification of delayed events is more subjective due to the lack of a sharp onset, so the determination of the number of such events is necessarily somewhat arbitrary. Let the threshold of a delayed event be a PLO rate of 0.01/second. The increases typically last several days, so that an estimate of the number of delayed events is the number of orbits from which at least one 6-hour period is included in the final data set. Such periods are identified in Figure V-1. There are 26 orbits with at least one period. Another method is to count the number of transitions from PLO rates less than 0.01/second to PLO rates greater than 0.01/second which are not associated with identified prompt solar events. There are 36 such transitions from 72/273 - 74/2. The typical maximum PLO rate for these delayed events is ~ 0.05/second. Thus, there are somewhat more delayed events than prompt events, and the prompt events are typically 10 times larger than the delayed events.

Whether solar flares can produce the delayed events depends on how much separation there must be from the flare site to the directly connected longitude of $\sim 60^{\circ}$W in order for the flare not to be seen as a prompt event. If the separation is comparable to the HWHM of 60° for the distribution in solar longitude of prompt solar events summarized by McCracken and Rao (1970), then, to produce a comparable number of delayed and prompt events, the average position of a delayed event will be $\sim 60^{\circ}$E. It will take $\sim$ 5 days before such an event becomes well-connected to earth, and by this time the event will have decayed to $\lesssim 0.01$ times the size of a typical prompt event compared to the observed ratio of ~ 0.1.

If, on the other hand, the required separation distance in order for an event not to be seen as a prompt event is only the 20^{o} HWHM of the azimuthal spread of an event near 1 AU as deduced by McCracken, et al. (1971), delayed events will be directly connected after $\sim$ 2 days and thus be nearly as large as prompt events. The current understanding of the azimuthal propagation of prompt solar events does not indicate what the required separation is, so this solar flare model of delayed events remains as a possible explanation for the increases reported in this study.

5. A Propagation Model. If the intensity increases observed in 1973 are due to particles being injected into the ecliptic plane at $\sim$3 AU either from out of the ecliptic or by local acceleration, their propagation back to 1 AU is closely analogous to galactic modulation. A numerical solution to the Fokker-Planck propagation equation including diffusion, convection, and adiabatic energy loss has been developed using certain simplifying assumptions which are thought to be approximately correct.

i) A steady state exists. Such a situation is suggested by the lack of dependence of $\xi_{\parallel}$ on $\frac{dU/dt}{U}$ shown in Figure VII-1.

ii) Any injection is taking place beyond a distance L $\sim$ 3 AU such as in shocks or connection to an out of the ecliptic source.

iii) Only the radial dependence is examined, and the radial diffusion coefficient κ_{rr} is assumed independent of energy and radius. This dependence of κ has been successfully used

Figure VII-1

The dependence of $\xi_{\|}$ on (dU/dt)/U. (dU/dt)/U is approximated using finite differences in the PLO rate. Only 6-hour periods for which the PLO rate is known for the previous and subsequent 6-hour periods are included. The dashed line is the least squares fit to the data.

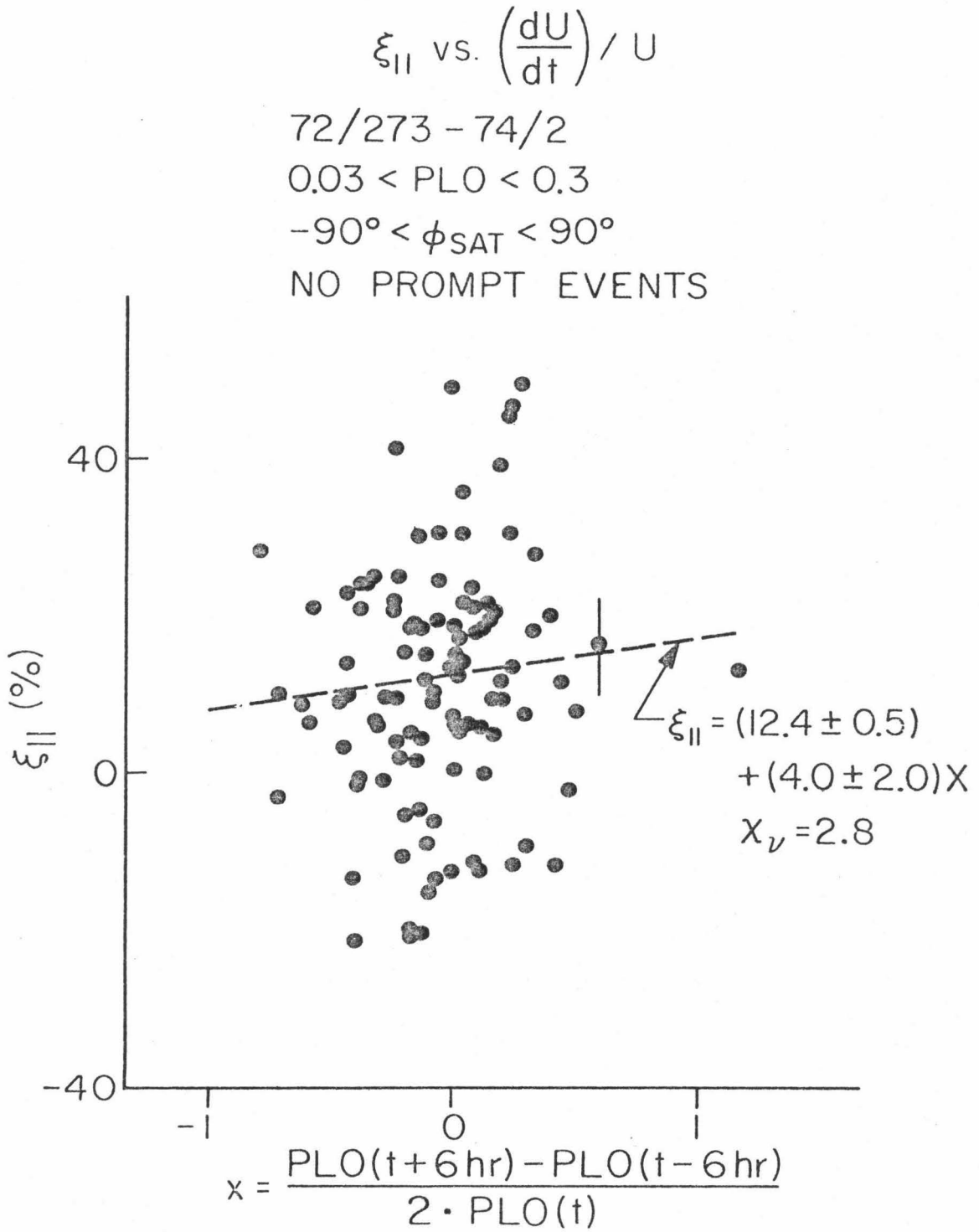
ξ_{II} vs. $\left(\frac{dU}{dt}\right)/U$
72/273 - 74/2
0.03 < PLO < 0.3
$-90° < \phi_{SAT} < 90°$
NO PROMPT EVENTS
40
0
-40
ξ_{II} (%)
$\xi_{II} = (12.4 \pm 0.5) + (4.0 \pm 2.0)X$
$\chi_\nu = 2.8$
-1
0
1
$X = \frac{PLO(t+6hr) - PLO(t-6hr)}{2 \cdot PLO(t)}$

by Lupton and Stone (1973) to fit the temporal development of prompt solar particle events.

Details of the numerical solution are presented in Appendix C. The solution has the form

$$U(r) = A\, e^{f(V/\kappa, C, r)\, V\, r/\kappa} \qquad (7\text{-}1)$$

where f is a monotonic function of r varying from C at r = 0 to 1 at large r. Thus, the solution grows approximately exponentially with r with a scale length of $\sim \kappa/V$. Using the typical solar wind velocity of 440 km/second, C = 2.77 (corresponding to $\gamma = -3.15$), and a κ of 10^{21} cm^2/second, the model produces a radial diffusive anisotropy and a modulation given by

$$\xi_{DIF,x} = 17 \text{ per cent}, \qquad U(3 \text{ AU})/U(1 \text{ AU}) = 11 .$$

This diffusive anisotropy is comparable to the value of $\sim$ 14 per cent found in this work. The modulation of 11 is consistent with the observations of McDonald, et al. (1975). Smaller values of κ can produce much larger modulation since the scale length is approximately proportional to κ. These modulation factors can be reduced substantially by having the injection of particles occurring between 2 and 4 AU, and thus the gradient implied by eq. (7-1) would only hold out to 2 AU. An increasing κ with radius would also reduce the modulation.

The model is also consistent with other characteristics of the diffusive anisotropy found in this study. As shown in Appendix C, the diffusive anisotropy is approximately independent of κ but proportional to V. κ is not directly observable, but is thought to depend on the fluctuations in the magnetic field. No significant dependence of the dif-

fusive anisotropy on the fluctuations in the magnetic field was found. As shown in Figure VII-2, the diffusive anisotropy did increase with increasing solar wind velocity, approximately as predicted by the model.

Thus, there is a simple model for propagating particles injected at $\sim$ 3 AU which explains the size of the diffusive anisotropy found at 1 AU, produces a radial gradient such as those indicated by the measurements of McDonald, et al. (1975) for a reasonable size of the diffusion coefficient, and whose predictions of the dependence of the diffusive anisotropy on κ and the solar wind speed are consistent with the observations.

6. Role of Continuous Solar Injection. The new measurements reported herein indicate that continuous solar injection is not necessary to produce increases in the low-energy proton flux such as those seen during 1973. The strongest direct evidence that some events are due to continuous solar injection is found in the observations of Krimigis, et al. (1971) and the detailed analysis of these data by Roelof and Krimigis (1973). The observations covered 3 solar rotations in 1967. Three delayed events are discussed in which there is a large anisotropy throughout the event due to particles coming from the sun, indicating continuous solar injection. These data are at energies $\geq$ 0.3 MeV.

At energies nearer the 1.3 - 2.3 MeV used in the present study, the direct evidence consists of anisotropy measurements made by Fan, et al. (1968) using two periods, each of $\sim$ 6 hours. The 0.8 - 2.0 MeV protons were found to be streaming from the sun in a direc-

Figure VII-2

The average x-component of the diffusive anisotropy as a function of the solar wind speed. The solid curves are calculated using the propagation model discussed in Section VII-A-5 for the parameters indicated.

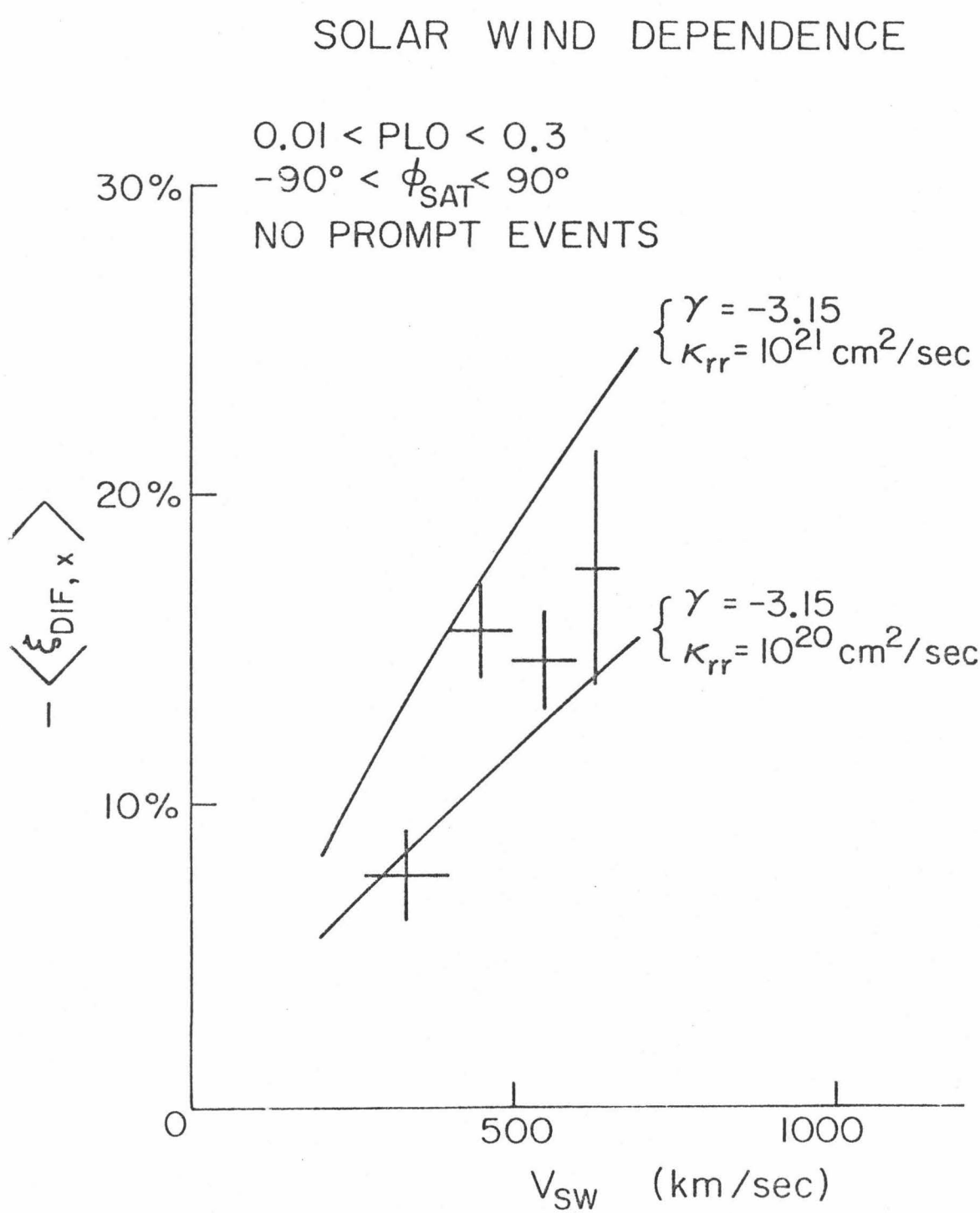
SOLAR WIND DEPENDENCE
0.01 < PLO < 0.3
-90° < ϕ_{SAT} < 90°
NO PROMPT EVENTS
γ = -3.15
κ_{rr} = 10^{21} cm^2/sec
γ = -3.15
κ_{rr} = 10^{20} cm^2/sec
30%
20%
10%
0
500
1000
$\langle \xi_{DIF,x} \rangle$
V_{SW} (km/sec)

tion close to the long-term average magnetic field direction. These data indicate occasional solar injection, but do not require continuous injection.

Consequently, at least at energies $\gtrsim$ 1 MeV, continuous solar injection may not be the predominant source over the solar cycle of the proton increases seen between prompt solar events; rather, some other mechanism, such as those discussed above to explain the increases seen in 1973, may be the usual source.

B. Quiet-Time Measurements of Rao, et al. (1967b)

The anisotropy measurements of Rao, et al. (1967b) were taken during the periods between observed increases. About 66 days of data from the UTD experiments on Pioneer 6 and 7 during 1965 and 1966 were used. As noted in Chapter I, the flux during these periods, when extrapolated to the energies used in the current study, is within the range of fluxes used in the present study. In contrast to the typical observed anisotropy of 7 per cent reported in Chapter VI, Rao, et al. reported an anisotropy of 0.19 % ± 0.05 %. Forman and Gleeson (1975) have discussed the difficulties in reconciling this small anisotropy with current understanding of propagation. A possible explanation of this result is that the observations included a large isotropic background. This possibility is consistent with the fact that the smallest flux seen by the University of Chicago experiment (Fan, et al., 1968) at the same energies during 1966 was ~ 30 times smaller than that seen by Rao, et al. Even lower fluxes have been seen at these energies by the Caltech EIS experiment on IMP-7 during 1973 (Mewaldt, et al., 1975b). This background in the UTD instruments

will minimally affect anisotropy measurements reported by the UTD group at higher fluxes such as those seen during prompt solar particle events.

C. Magnetic Field Direction

The interplanetary magnetic field has long been thought to play a dominant role in low-energy proton propagation. McCracken, et al. (1968) investigated the dependence of the observed anisotropy on the magnetic field direction using 1-hour averages during the early part of prompt solar particle events. A strong dependence was found, and was interpreted by the authors as consistent with an observed anisotropy consisting of two parts: an invariant convective part and a field-aligned diffusive part. This picture of the diffusive anisotropy being field-aligned has been used by many authors, e.g. McCracken, et al. (1971), McKibben (1973), Wibberenz (1974). Recent observations have raised questions about this simple picture. Allum, et al. (1974) found that during the easterly anisotropy observed late in the decay of solar particle events, the observed anisotropy direction was independent of the observed magnetic field direction. Six-hour averages were used. The authors noted that this unexpected result could be explained in terms of field-aligned diffusion if the diffusion coefficient along the magnetic field direction had the dependence:

$$\kappa_{\parallel} \propto 1/\cos^2(\phi-\overline{\phi})$$

where $\overline{\phi}$ is the long-term average of the magnetic field direction. No justification for this dependence was presented. Pesses and Sarris (1975) have reported periods when they deduced the diffusive anisotropy could not be field-aligned, using 15-minute averages by

examining periods when the magnetic field was radial.

The previous observations have used the direction of the observed anisotropy which includes the convective anisotropy, which is unrelated to the magnetic field direction. For a direct determination of the dependence of the diffusive anisotropy direction on the magnetic field direction, $\vec{\xi}_{CON}$ must be subtracted from $\vec{\xi}_{DIF}$, as was done in the present study.

If the diffusive anisotropy were field-aligned, the following functional dependence is expected:

$$\phi_{\xi_{DIF}} = a + b\,\phi_B \ ,$$

with a consistent with 0 and b consistent with 1. If diffusion were isotropic, b would be consistent with 0.

The best least-squares fit to the data was found for

$$a = -10.2^{\circ} \pm 2.9^{\circ} \ , \qquad b = 0.71 \pm 0.06 \ .$$

Thus, a strong dependence of the diffusive anisotropy direction on the magnetic field direction has been found, indicating $\varkappa_{\perp}$ to be typically less than $\varkappa_{\parallel}$ for these 212 periods. The difference from the dependence expected for field-aligned diffusion is consistent with a finite $\varkappa_{\perp}/\varkappa_{\parallel}$. The size of this ratio depends on the relative sizes of the spatial gradients perpendicular and parallel to the magnetic field. Since information from only one satellite is available, these gradients are not known.

APPENDIX A. ANISOTROPY MEASUREMENTS

1. Introduction

This appendix describes the determination of anisotropies used in this study and discusses the statistical uncertainties of such measurements. The IMP-7 instrument accumulates counts separately for each of 8 sectors. An anisotropy is calculated using the accumulated counts, and the statistical uncertainties associated with the accumulated counts produce statistical uncertainties in the computed anisotropy. Ideal instruments are assumed which require no corrections for dead times. Roelof (1974) has discussed dead time effects. The correction for finite opening angles will be discussed in Section A-4. Only first order anisotropies are considered.

2. Calculation of the Observed Anisotropy

A cosine expansion is fit to the accumulated counts for the different sectors. Let Y_i be the number of counts for sector i , σ_i the statistical uncertainty associated with Y_i , and ϕ_i be the average angle of sector i. The angles ϕ_i for IMP-7 are given in Figure II-2. Then the Y_i's can be approximated by the function

$$f_1(\phi_i, A, \xi, \phi) = A(1 + \xi \cos(\phi_i - \phi)) \ . \qquad (A-1)$$

Following the method of Zwickl and Webber (1974), a least-squares fit is made to an equivalent function

$$f_2(\phi_i, A, \alpha, \beta) = A + \alpha \cos \phi_i + \beta \sin \phi_i \ . \qquad (A-2)$$

The least-squares fit has been done using $\sigma_i = (Y_i)^{\frac{1}{2}}$. The parameters of eqs. (A-1) and (A-2) are related by

$$\xi = (\alpha^2 + \beta^2)^{\frac{1}{2}} / A \ , \qquad (A-3)$$

$$\phi = \tan^{-1}(\beta/\alpha) \ . \qquad (A-4)$$

Although weighted averages have been used to determine A, α, and β, the approximation that all σ_i's are equal has been used to determine the uncertainty in the fit parameters. The approximation is a good one for small anisotropies. Using this approximation, the best fit is made for

$$A = (1/s)\Sigma\, Y_i \,, \qquad \text{where } s \text{ is the number of sectors}$$

$$\alpha = (2/s)\Sigma\, Y_i \cos\phi_i$$

$$\beta = (2/s)\Sigma\, Y_i \sin\phi_i$$

The observed anisotropy amplitude is

$$\xi_{OBS} = w\xi \,, \qquad \text{where } w = w_s w_a$$

The smoothing factor w_s, which equals $(\pi/s)/\sin(\pi/s)$, corrects for the reduction in the anisotropy due to the finite number of sectors (Chapman and Bartels, 1940). w_a is the smoothing factor correcting for the finite opening angle of the instrument, and is discussed in Section A-4.

3. Statistical Significance

To understand the significance of an observed anisotropy, the likelihood of possible true anisotropies must be determined. The probability of the true anisotropy, given an observed anisotropy, is determined using Bayes' Theorem:

$$P(\psi_{true}|\psi_{obs}) = \varkappa P(\psi_{true})\cdot P(\psi_{obs}|\psi_{true}) \quad \text{(A-5)}$$

where $\varkappa$ is normalization. It is assumed that the true anisotropy distribution is of the form given by eq. (A-1) or equivalently eq. (A-2). Certain approximations are made which are valid only for small anisotropy amplitudes.

Let the true distribution be given by eq. (A-2) and character-

ized by A_o, α_o, and β_o. Let

$$\xi_{true} = \frac{(\alpha_o^2 + \beta_o^2)^{\frac{1}{2}}}{A_o}$$

and $\phi_o = \tan^{-1}(\beta_o/\alpha_o)$. The distributions of Y_i's sampled from this distribution are approximated as Gaussians, each having an equal standard deviation σ. For the present work, $\sigma \equiv (s/\Sigma\ 1/\sigma_i^2)^{\frac{1}{2}}$. Each sample distribution is characterized by A, α, and β. The approximation is made that the relative uncertainty in A is negligibly small compared to the uncertainties in α and β, which will be the case for $\xi \ll 1$. α and β then have Gaussian distributions with means of α_o and β_o respectively, and standard deviations of $\sigma(2/s)^{\frac{1}{2}}$. Define a scale factor for the anisotropy amplitude:

$$z = w\,(2/s)^{\frac{1}{2}}\,\sigma/A_o\ .$$

Let

$$r = \xi_{obs}/z\ ,$$

$$x = \xi_{true}/z\ .$$

z is approximately the anisotropy amplitude expected to be measured if the true distribution is isotropic. Hence, r is a measure of the statistical significance of an observation -- the larger r, the more significant the observation.

Equation (A-5) becomes

$$P(x, \phi_o \,|\, r, \phi) = k_1 P(x, \phi_o) P(r, \phi \,|\, x, \phi_o)\ , \qquad \text{(A-6)}$$

and from the Gaussian distributions at α and β,

$$P(r, \phi \,|\, x, \phi_o) = (r/2\pi)\, e^{-(r^2+x^2-2rx\cos(\phi-\phi_o))/2}\ . \qquad \text{(A-7)}$$

Integrating over angle gives the probability of measuring r given a

true distribution characterized by x:

$$P(r|x) = r e^{-\frac{1}{2}r^2} e^{-\frac{1}{2}x^2} I_o(xr) , \qquad (A-8)$$

where I_o is the zero-order modified Bessel function. The mode and 68.2 per cent and 95.4 per cent confidence intervals of this probability function are plotted in Figure A-1 as a function of x. There is a 68.2 per cent (95.4 per cent) probability that an observed r will be within the 68.2 per cent (95.4 per cent) confidence interval. The intervals are chosen to minimize their lengths. Note that as $x \to 0$ (i.e., small true anisotropies) the most likely measured anisotropy approaches z, not 0.

In order to compute $P(x, \phi_o|r, \phi)$, an assumption must be made about the a priori probability of different anisotropies, $P(x, \phi_o)$. The assumption has been made that $P(x, \phi_o)$ is independent of x and ϕ_o. Other assumptions are possible, however. Another assumption might be that all points in the α-β plane are equally likely, i.e., $P(x, \phi_o) \sim x$. This a priori assumption would be appropriate if the two orthogonal directions corresponded to two independent sources of particles. The assumption which is used of a priori equally likely amplitudes corresponds to a single particle source in an arbitrary direction, and so is considered more appropriate to interplanetary propagation.

So now

$$P(x, \phi_o|r, \phi) = k_2 P(r, \phi|x, \phi_o) . \qquad (A-9)$$

Integrating eq. (A-9) over ϕ_o gives the probability that the true distribution has an anisotropy amplitude of x given an observation of r:

Figure A-1

The 68.2% and 95.4% confidence intervals for observing an anisotropy amplitude given a true anisotropy amplitude. Both the observed and true anisotropy amplitudes have been normalized by z, where

$$z = w\ (2/s)^{0.5}\ \sigma/A_o\ .$$

w is the smoothing factor, usually ≈1., which depends on the number of sectors s and the angular response of the detector system. σ is the statistical uncertainty in the number of counts in a sector (assumed to be independent of sector). A_o is the average number of counts per sector.

CONFIDENCE INTERVALS OF OBSERVED ANISOTROPY

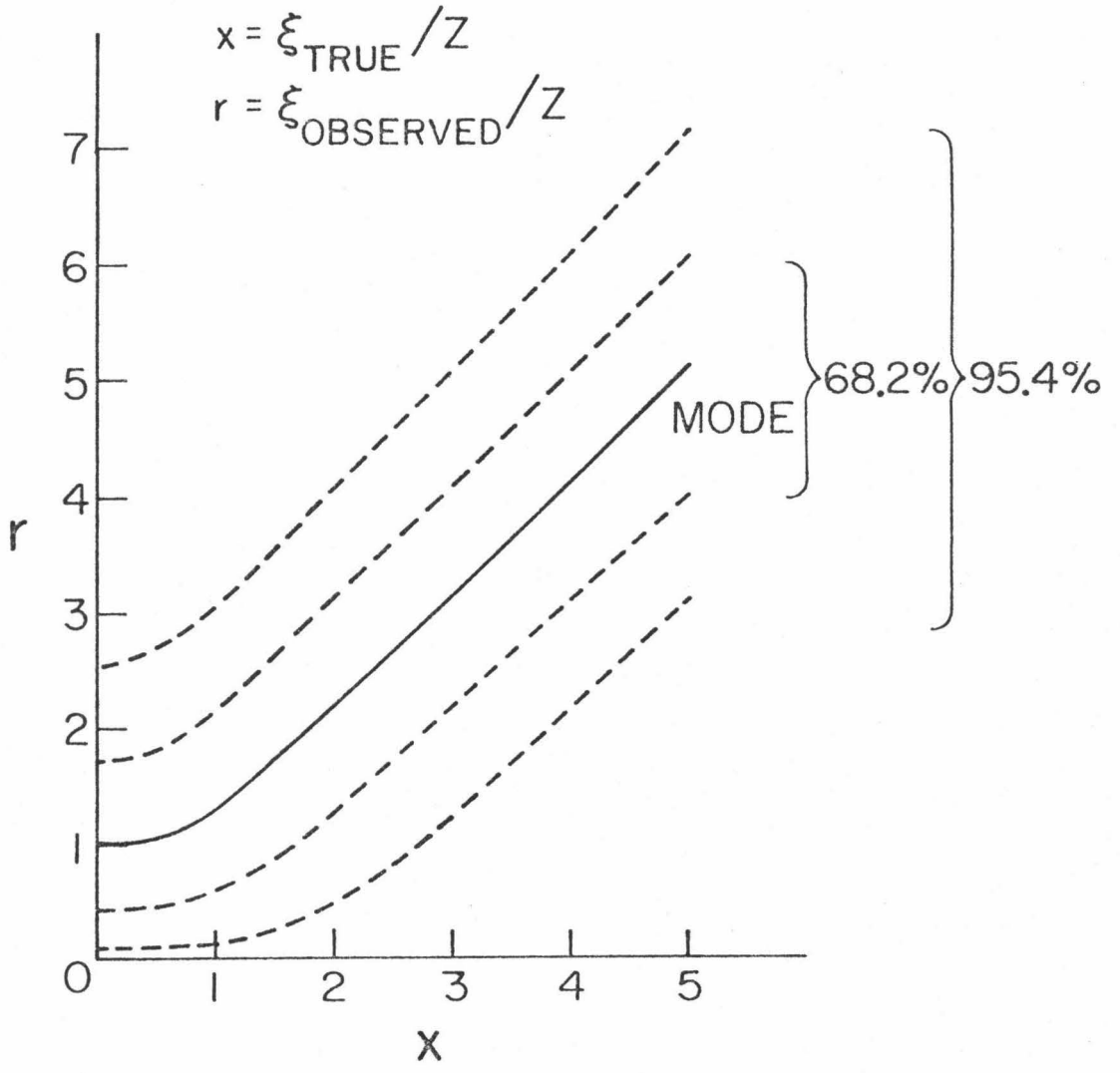

$$P(x|r) = (2/\pi)^{\frac{1}{2}} e^{-r^2/4} e^{-\frac{1}{2}x^2} I_o(xr)/I_o(r^2/4) \quad . \qquad \text{(A-10)}$$

This probability distribution is plotted for $r = 0$, 2, and 3 in Figure A-2. The 68.2 per cent and 95.4 per cent confidence intervals are also indicated. The most likely x and the 68.2 per cent and 95.4 per cent confidence intervals are plotted as a function of r in Figure A-3. For $r \leq \sqrt{2}$ the most likely true anisotropy amplitude is 0. For $r \gtrsim 3$ the most likely true amplitude is nearly the observed amplitude with a standard deviation of nearly z.

Integrating eq. (A-9) over the anisotropy amplitude x gives probability of the true direction being ϕ_o given an observation of r and ϕ:

$$P(\phi_o|r, \phi) = k_3 e^{-r^2 \frac{\sin^2 \Delta\phi}{2}} \left[1 + \text{erf}\left(\frac{r \cos \Delta\phi}{\sqrt{2}}\right)\right] \qquad \text{(A-11)}$$

where $\Delta\phi = \phi_o - \phi$, and k_3 is a normalization constant. The distribution is symmetric with respect to $\Delta\phi$ and the most likely $\Delta\phi$ is 0. For large r, that is, for statistically significant observations,

$$P(\phi_o|r, \phi) \cong k_3 e^{-\frac{1}{2}r^2 \Delta\phi^2} \qquad \text{(A-12)}$$

so that the probability distribution for the true angle approaches a Gaussian distribution with a standard deviation in radians of $1/r = z/\xi_{OBS}$.

Figure A-4 shows the half-width - half-maximum for eq. (A-11) as a function of $1/r$. For $r < 0.431$ the HWHM is not defined because the distribution is too broad. The figure shows that the HWHM of $(2 \ln 2)^{\frac{1}{2}}/r$ appropriate for large r [eq. (A-12)] is a good approximation for r as small as 0.5.

Figure A-2

The probability distribution for the normalized true anisotropy amplitude for three values of the normalized observed anisotropy amplitude. Also shown are the 68.2% and 95.4% confidence intervals for each distribution. The normalization factor z is defined in the caption of Figure A-1.

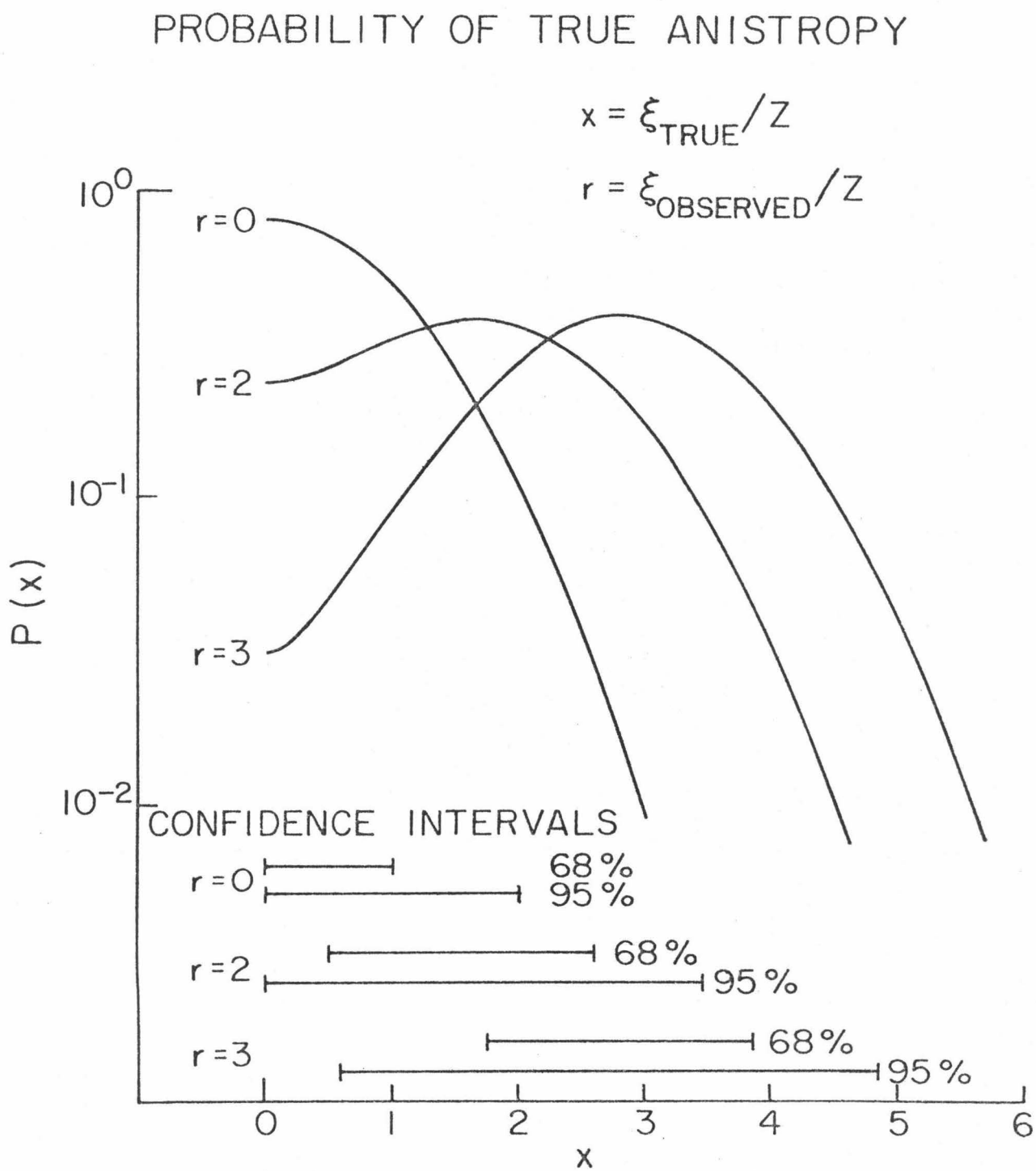
PROBABILITY OF TRUE ANISTROPY
x = ξTRUE/Z
r = ξOBSERVED/Z
10^0
10^-1
10^-2
P (x)
r=0
r=2
r=3
CONFIDENCE INTERVALS
r=0
68%
95%
r=2
68%
95%
r=3
68%
95%
0
1
2
3
4
5
6
x

Figure A-3

The 68.2% and 95.4% confidence intervals for the normalized true anisotropy amplitude given a normalized observed anisotropy amplitude. The normalization factor z is defined in the caption of Figure A-1.

CONFIDENCE INTERVALS OF TRUE ANISOTROPY

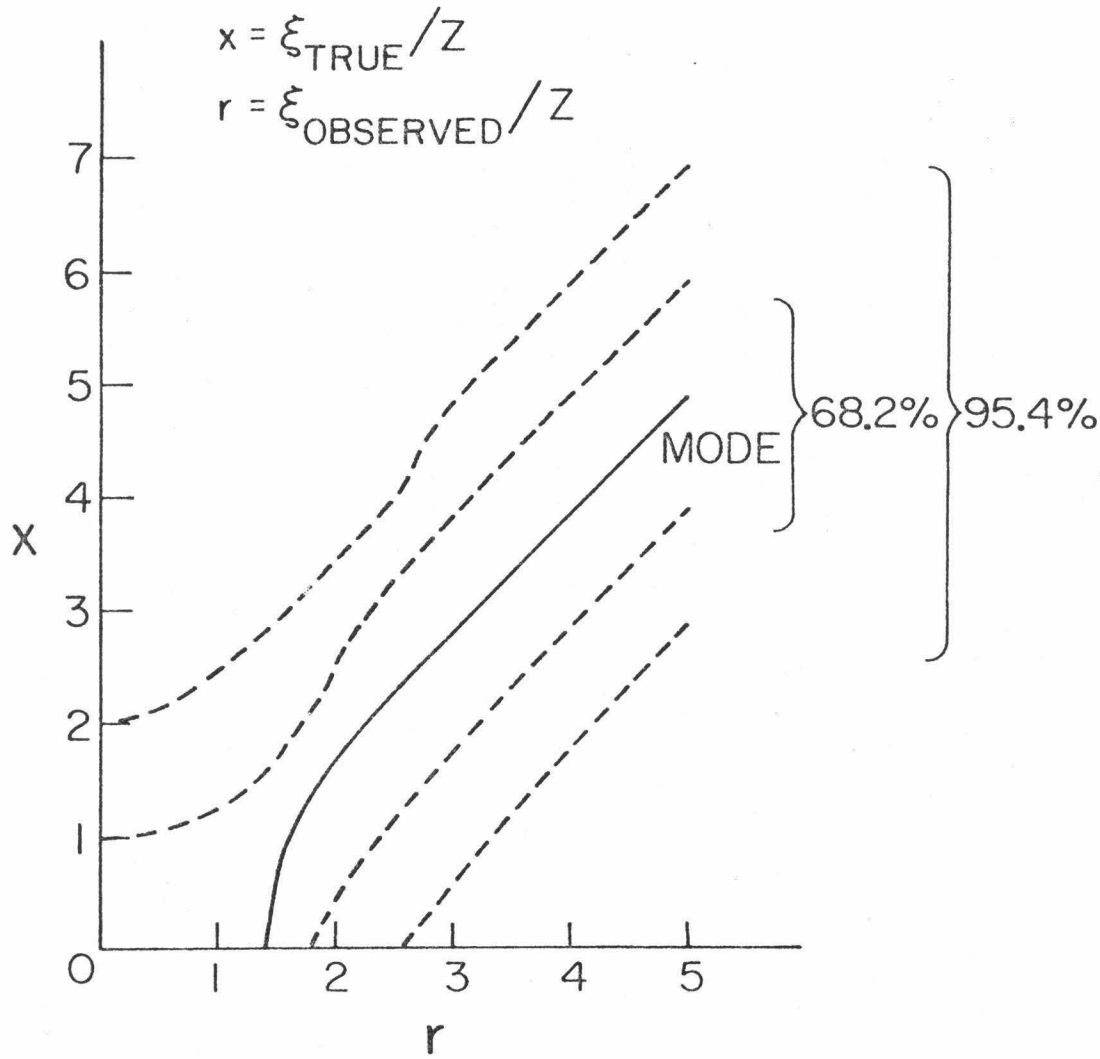

Figure A-4

The half-width-half-maximum of the probability distribution of the difference in the direction of the observed anisotropy and the direction of the true anisotropy as a function of the normalized observed anisotropy amplitude, r. The HWHM cannot be defined for $r < 0.43$.

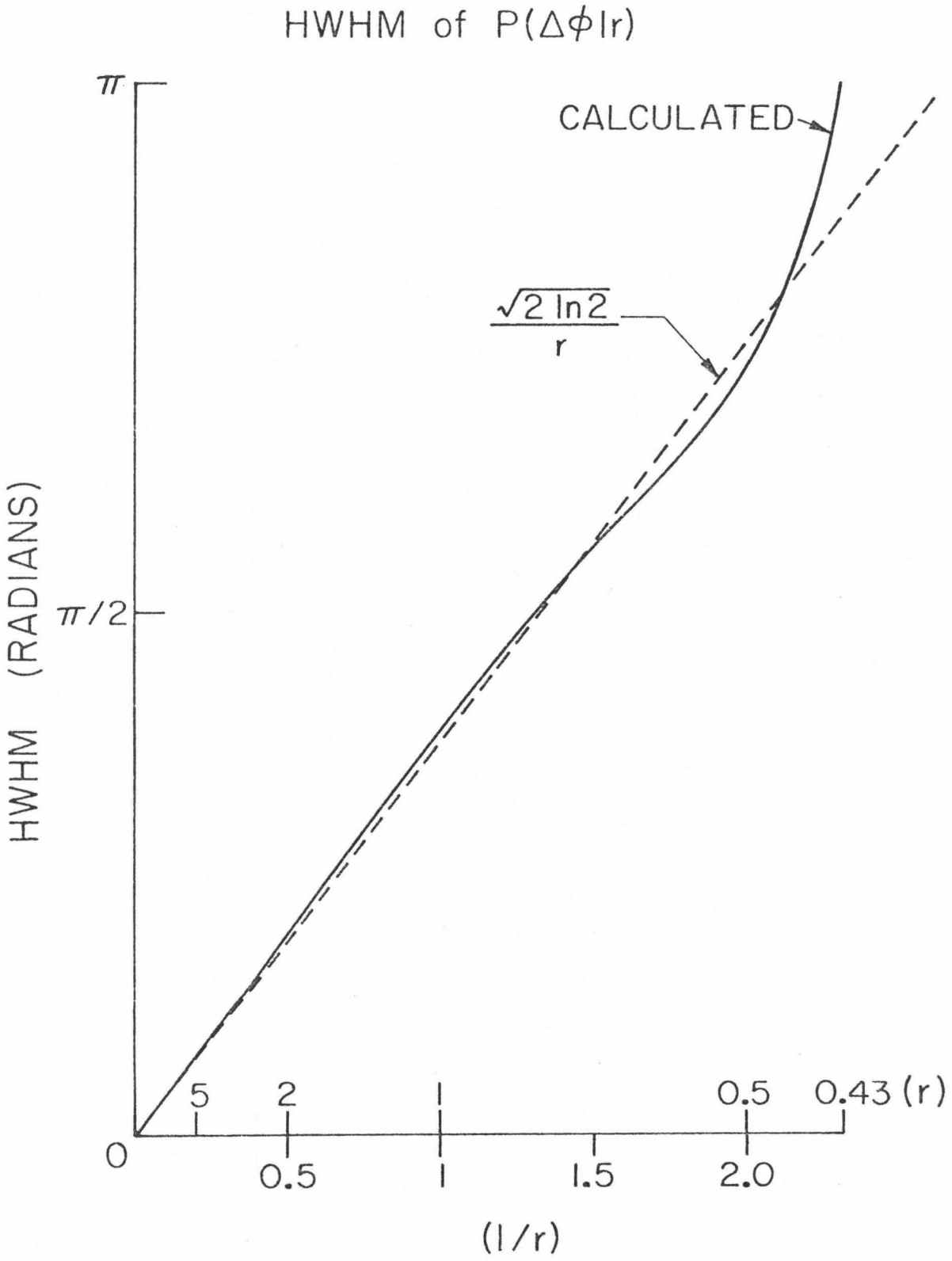
HWHM of P(Δφ|r)
π
π/2
0
HWHM (RADIANS)
CALCULATED
√2 ln2
r
5
2
1
0.5
0.43 (r)
0.5
1
1.5
2.0
(1/r)

4. Finite Opening Angle

Sentman and Baker (1974) have shown that the observed counting rate is given by

$$C(\gamma) = 4\pi \sum_{\ell} \frac{1}{2\ell+1} D_\ell S_\ell P_\ell(\cos\gamma) \ ,$$

where P_ℓ are Legendre polynomials, D_ℓ are the coefficients in Legendre polynomial expansion of the pitch angle distribution, S_ℓ are the coefficients in the expansion of the detector angular response, and γ is the angle between the direction of the anisotropy and the symmetry axis of the detector telescope.

The first order anisotropy ($\ell = 1$) is reduced by

$$\frac{1}{w_a} = \frac{\int_0^\pi S(\theta)\cos\theta \sin\theta \, d\theta}{\int_0^\pi S(\theta) \sin\theta \, d\theta} \cdot \cos(\theta_o) \ ,$$

where θ_o is the elevation of the direction of the anisotropy above the plane of rotation of the telescope. For the Caltech instrument this plane is the ecliptic plane. θ_o is assumed to be 0 for this study, so the measured anisotropies are the projection of the true anisotropy vector onto the ecliptic plane.

$S(\theta)$ has been determined for the Caltech EIS experiment on IMP-7 using Monte-Carlo simulation. w_a is found to be 1.0/0.951.

APPENDIX B. DETERMINATION OF ENERGY SPECTRA

1. Method

The procedure used for calculating proton energy spectra has been discussed by Hurford (1974). This appendix discusses the particulars of the procedure used in this work.

The range of D2 pulse heights for protons stopping in D2 has been divided into 9 bins and the number of analyzed events with the corresponding pulse heights accumulated for each of the 6-hour periods used in this study. Corrections, which are discussed below, are made to the accumulated counts:

$$N_i = C_i - A_i - f_i(P25_i + P256_i) \qquad (B-1)$$

where N_i is the corrected number of counts for the i^{th} bin, C_i is the observed number of counts, A_i is the alpha contamination, f_i is the foldback correction factor, and $P25_i$ and $P256_i$ are the number of particles which penetrate D2 and trigger D5 and D56 respectively, and have a D2 pulse height corresponding to the i^{th} bin. The energy interval of incident protons for each of the pulse height bins is determined, and a least-squares fit is made to the function

$$dN/dT = A\,T^{\gamma} ,$$

where T is the incident kinetic energy of the proton.

During the period 73/86 to 73/154 the offset of the D2 pulse-height analyzer differed from the nominal value by $\sim$ 4 channels -- the nominal channel 16 becoming channel 20. This offset was determined using the D2 pulse height for D5 single events. The nominal electronic calibrations given by Mewaldt and Vidor (1976) have been adjusted by 4 channels for this period. In addition, the lowest two D2

pulse height bins have not been used in order to maintain the same incident energy threshold.

2. Incident Energy Intervals

The D2 pulse heights and the corresponding incident particle energies are listed for the 9 proton bins and 3 alpha bins (see below) in Table B-1. The incident energy is determined by adding the energy loss in D2 to the calculated energy loss in the thin aluminized mylar window covering the detector stack. The energy loss in D2 is determined from the D2 pulse height using the results of the electronic calibration of the instrument (Mewaldt and Vidor, 1976). The equivalent thickness of the aluminized mylar window is 2.4 mg/cm^2 of lucite as measured using 6.051 MeV and 8.785 MeV α-particles from $^{212}_{Pb}$. Since $\langle \sec\theta \rangle$, where θ is the angle of incidence with respect to the symmetry axis of the detector stack, is 1.054 as determined by a Monte-Carlo simulation of the detector stack response, the effective thickness of the window for particles stopping in D2 is 2.53 mg/cm^2. From this effective thickness and the known residual energy loss in D2, the incident energy is calculated using the range-energy tables by Janni (1966). Alpha energies are determined using the relationship:

$$R_\alpha(T) = (m_\alpha/4) R_p(T/m_\alpha) \qquad \text{(B-2)}$$

where R_α is the alpha range, R_p the proton range, T the alpha kinetic energy, and m_α the alpha mass.

Errors in the determination of the effective window thickness produce errors in the determination of γ and hence in $\vec{\xi}_{CON}$. Statistical errors in the measurement of the thickness or determination

TABLE B-1

Bin No. protons	D2 Pulse Height channels	Incident Energies MeV/nucleon nominal	73/86 - 73/154
1	16 - 16	1.185 - 1.204	not used
2	17 - 19	1.204 - 1.261	not used
3	20 - 24	1.261 - 1.379	1.185 - 1.282
4	25 - 29	1.379 - 1.515	1.282 - 1.406
5	30 - 34	1.515 - 1.667	1.406 - 1.544
6	35 - 39	1.667 - 1.829	1.544 - 1.698
7	40 - 44	1.829 - 1.999	1.698 - 1.861
8	45 - 49	1.999 - 2.172	1.861 - 2.031
9	50 - 53	2.172 - 2.315	2.031 - 2.172
alphas			
10	87 - 119	1.44 - 1.69	1.41 - 1.66
11	120 - 149	1.69 - 1.93	1.66 - 1.91
12	150 - 198	1.93 - 2.37	1.91 - 2.34

TABLE B-2. Alpha Energies Which Contaminate Proton Bins

Bin No.	Nominal		73/86 - 73/154	
	Mean ($\frac{\text{MeV}}{\text{nucleon}}$)	Width ($\frac{\text{MeV}}{\text{nucleon}}$)	Mean ($\frac{\text{MeV}}{\text{nucleon}}$)	Width ($\frac{\text{MeV}}{\text{nucleon}}$)
1	1.081	0.002	not used	
2	1.086	0.008	not used	
3	1.097	0.014	1.086	0.012
4	1.113	0.019	1.100	0.016
5	1.132	0.019	1.116	0.016
6	1.153	0.022	1.132	0.020
7	1.176	0.024	1.158	0.023
8	1.201	0.026	1.181	0.024
9	1.223	0.019	1.204	0.021

of $\langle \sec \theta \rangle$ are quite small (~ 0.2 per cent). However, there may be systematic errors in the range-energy table, in the approximation of mylar as lucite, or in eq. (B-2). An estimate of these systematic errors is made by using the range-energy tables of Northcliffe and Schilling (1970) for alpha particles in mylar to determine the window thickness. A thickness of 2.47 mg/cm^2 is determined, compared to 2.4 mg/cm^2 for the previous calculation. If the thickness were 2.47 instead of the 2.4 used, a γ of -3.00 would be measured as a γ of -3.04, producing an error in $\vec{\xi}_{CON}$ of only $\sim$ 0.2 per cent. Consequently, possible errors in the determination of the window thickness have at most negligible effect on the anisotropies of this study.

3. Alpha Correction

Some of the counts in the 9 proton bins are due to stopping alphas. An estimate of this contamination is provided by the number of particles that lose too much energy in D2 to be stopping protons. A least-squares fit of the form

$$dN/dT = A\,T^{\gamma}$$

where T , alpha incident energy, is in MeV/nucleon, is made to the three alpha bins shown in Table B-1. This alpha spectrum is then extrapolated to lower energies to compute the number of counts that are subtracted from the observed counts in the 9 proton bins, which are designated A_i in eq. (B-1). The average alpha incident energy and bin width corresponding to each of the 9 proton bins are shown in Table B-2.

4. Foldback Correction

Some of the particles contributing to the 9 proton bins pene-

TABLE B-3. D5 Pulse Heights Used to Bin D256 Events

Bin No.	D5 Pulse Height Nominal	73/86 - 73/154
1	234 - 400	not used
2	165 - 233	not used
3	102 - 164	149 - 400
4	65 - 101	89 - 148
5	44 - 64	61 - 88
6	31 - 43	42 - 60
7	19 - 30	28 - 41
8	10 - 18	17 - 27
9	3 - 9	7 - 16

TABLE B-4. Foldback Correction Factors (f_i)

Bin No.	Nominal	73/86 - 73/154
1	0.10	not used
2	0.20	not used
3	0.36	0.20
4	0.87	0.46
5	1.50	0.98
6	2.05	1.60
7	2.20	2.08
8	1.81	2.13
9	2.90	1.90

trate D2 and stop in the thin dead layers on the inside of the annulars D3 and D4. The size of this correction depends on the spectrum of penetrating particles and the efficiency with which penetrating particles are rejected by D3, D4, or D5.

The spectrum of penetrating particles is determined by accumulating $P25_i$ -- the number of D25 events whose D2 pulse height corresponds to one of the 9 proton bins listed in Table B-1. Due to an instrumental anomaly, D25 events are occasionally read out as D256 events with the D2 pulse height lost. Such events are recognized by their zero D6 pulse height. Such events have been binned according to the average D2 pulse height appropriate for the observed D5 pulse height, as shown in Table B-3. The accumulated counts are designated $P256_i$.

The sum of $P25_i$ and $P256_i$ is then multiplied by a foldback correction factor f_i which is the ratio of the geometric factor of D25 events to the effective geometric factor of particles stopping in the dead layer of D3 or D4. The efficiency of D3 or D4 in rejecting particles depends on the particle's energy, so there is a different f_i for each of the 9 bins. The f_i were determined by comparing the energy spectrum of the Caltech experiments on IMP-7 and IMP-8 during 0 UT to 1200 UT 75/234. This period was chosen because both IMP-7 and IMP-8 were outside the magnetosphere and the relative number of penetrating to stopping particles in D2 was large. The energy spectrum observed by IMP-8, which needs no foldback correction, was well fit by a power law. The size of the foldback correction for IMP-7 was chosen to make the corrected spectrum equal to the extrapola-

tion of the observed IMP-7 D25 power law energy spectrum. The f_i are given in Table B-4. The uncertainty of the f_i is estimated by comparing the values determined using the above period to the values determined using 12:00 to 24:00 UT 75/235. The two sets of f_i agreed to within $\sim$ 20 per cent except f_9 was $\sim$ 50 per cent high for 75/235, and f_1 and f_2, which differed by a factor of $\sim$ 3, but have negligible effect on the spectra.

5. Example

The results of applying the procedure described in this appendix to data from 73/345 are shown in Figure B-1. The uncorrected spectrum, the corrected spectrum, and the corrections due to alpha contamination and penetrating particles are indicated. The alpha contamination is comparable to typical contamination. The foldback correction is somewhat smaller than typical, as seen by the γ of -3.67 compared to mean γ of -3.15.

Figure B-1

The determination of the spectral index γ for 73/345. The observed D2 counts, the correction due to α-contamination, the correction due to the foldback of protons which penetrate D2, and the corrected D2 counts are shown as a function of energy.

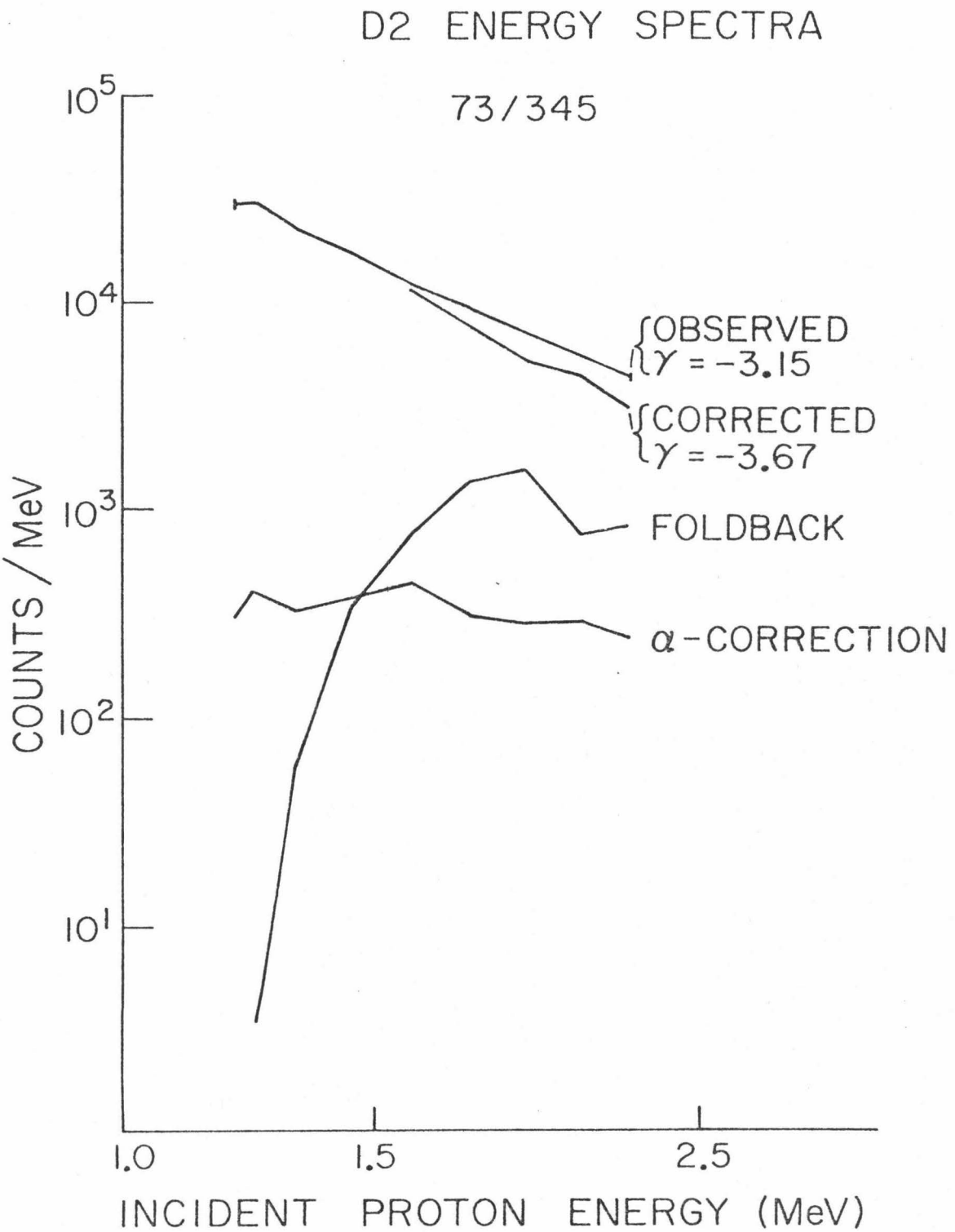
D2 ENERGY SPECTRA
73/345
10^5
10^4
10^3
10^2
10^1
COUNTS / MeV
OBSERVED
$\gamma = -3.15$
CORRECTED
$\gamma = -3.67$
FOLDBACK
α-CORRECTION
1.0
1.5
2.5
INCIDENT PROTON ENERGY (MeV)

APPENDIX C. PROPAGATION MODEL

The propagation of cosmic rays in interplanetary space is described by the Fokker-Planck equation:

$$\frac{\partial U}{\partial t} = \nabla\cdot(\underline{\underline{\kappa}}\cdot\nabla U)-\nabla\cdot(U\vec{V})+\frac{1}{3}\nabla\cdot\vec{V}\left(\frac{\partial}{\partial T}(\alpha(T)TU)\right) . \qquad (C-1)$$

This equation includes the effects of diffusion, convection, and adiabatic energy change. The equation is solved for $r\in[0, L]$ using certain simplifying assumptions:

1) all variables and parameters are independent of time;
2) the solar wind velocity $\vec{V}$ is radial and independent of position;
3) the energy spectrum of U is a power law;
4) $\alpha = 2$;
5) U remains finite as $r \to 0$;
6) no source of particles for $r < L$;
7) $\underline{\underline{\kappa}}$ is diagonal in reference frame aligned with the radial direction; $\kappa_\theta = \kappa_\phi = 0$ and $\kappa_{rr} = \kappa$ is independent of energy and position.

Let

$$U(r, \theta, \phi, T) = R(r)Q(\theta, \phi)T^{\gamma-\frac{1}{2}} . \qquad (C-2)$$

Equation (C-1) separates and R is given by

$$R'' + \left(\frac{2}{r} - \frac{V}{\kappa}\right)R' - \frac{2CV}{\kappa r}R = 0 . \qquad (C-3)$$

Let

$$R(r) = y(r)e^{Vr/\kappa} . \qquad (C-4)$$

Then

$$y'' + y'\left(\frac{2+V/\kappa r}{r}\right) - y\,\frac{(C-1)2(V/\kappa)r}{r^2} = 0 . \qquad (C-5)$$

This equation is solved using power series solution,

$$y = r^s \sum_{n=0}^{\infty} a_n r^n \quad . \tag{C-6}$$

The indicial equation for s has roots $s = 0, -1$, so one solution is obtained of the form

$$y_1(r) = \sum_{n=0}^{\infty} a_n r^n \quad . \tag{C-7}$$

Substitution of eq. (C-7) into (C-5) determines the coefficients a_n:

$$\begin{aligned} a_1 &= a_o(C-1)V/\varkappa \\ a_2 &= a_1^2/(3a_o) \\ a_n &= a_{n-1}\left[\frac{(V/\varkappa)(2C-n)}{n^2+n}\right] \qquad \text{for } n = 3, \ldots, \infty \end{aligned} \tag{C-8}$$

where a_o is arbitrary.

An independent solution exists with form

$$y_2(r) = Ay_1(r)\ell n\, r + r^{-1} \sum_{n=0}^{\infty} b_r r^n \quad .$$

y_2 is infinite at the origin and so is discarded. Thus, the desired solution is given by

$$R(r) = e^{Vr/\varkappa} \sum_{n=0}^{\infty} a_n r^n \quad .$$

a_o is determined by the value of R(L).

Physically, the density at $r = L$ is set by the source of particles at $r \geq L$. The solution then shows the radial distribution that will be established by the propagation of these particles.

The solution, normalized to 1 at $r = 0$, is plotted for several values of the Compton-Getting factor in Figure C-1. The radial distance has been scaled using $x = r/(\varkappa/V)$. For $\varkappa = 10^{21}$ cm^2/sec and $V = 440$ km/sec, $\varkappa/V = 1.5$ AU.

Figure C-1

The radial solution as a function of x for four values of the spectral index γ. The solutions are normalized to a value of 1.0 at x = 0. The Compton-Getting factor, C, corresponding to each γ is given.

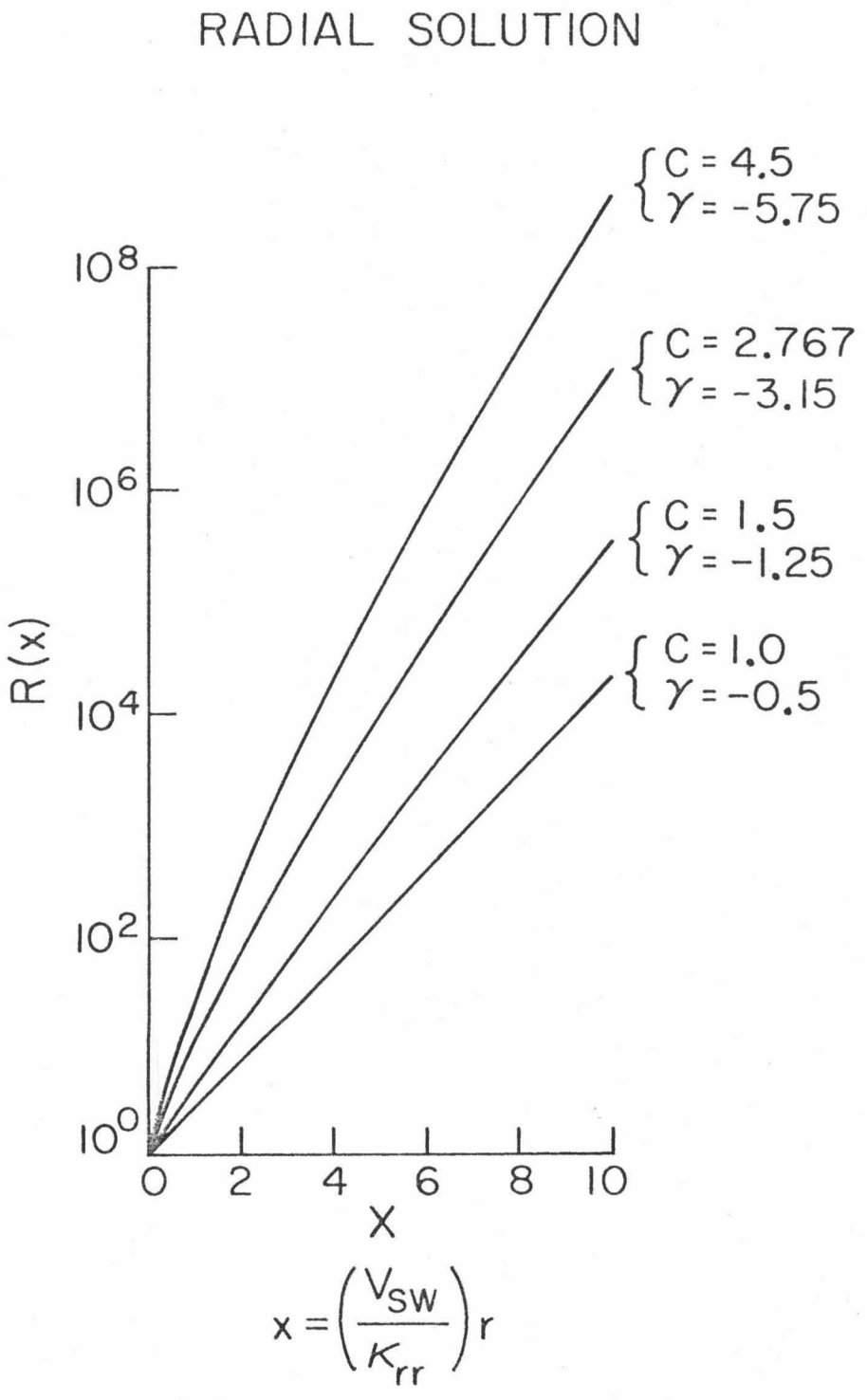
RADIAL SOLUTION
C = 4.5
γ = -5.75
C = 2.767
γ = -3.15
C = 1.5
γ = -1.25
C = 1.0
γ = -0.5
10^8
10^6
10^4
10^2
10^0
R(x)
0
2
4
6
8
10
X
x = (V_SW / K_rr) r

$$\xi_{DIF} = \frac{-3\kappa}{w}\left(\frac{dR}{dr}\right)\Big/R = \frac{-3V}{w}\ \frac{d\ell n\, R}{dx} \quad , \qquad (C\text{-}9)$$

so that the slope of a solution plotted in Figure C-1 is proportional to the diffusive streaming. At $x = 0$, $\frac{d\ell n\, R}{dx} = C$ and $\xi_{DIF} = \frac{-3CV}{w}$. For large x, $\frac{d\ell n R}{dx} \to 1$ and $\xi_{DIF} \to \frac{-3V}{w}$.

The dependence of ξ_{DIF} computed using eq. (C-9) on V and κ is shown in Figure C-2. The anisotropy is computed at 1 AU for 1.675 MeV protons with $\gamma = -3.15$. These values are typical of the data used in this work. ξ_{DIF} is relatively independent of κ, increasing by less than a factor of 2 when κ increases by a factor of 40. In contrast, ξ_{DIF} is nearly proportional to V. A qualitative picture is that the diffusive streaming approximately offsets the convective streaming in this steady-state model. Hence, increasing V and thus the convective streaming also increases the diffusive streaming. On the other hand, increasing κ does not increase the convective streaming so the radial gradient adjusts to keep the diffusive streaming approximately unchanged.

Figure C-2

The dependence of calculated diffusive anisotropy amplitude ξ on the radial diffusion coefficient κ_{rr} and the solar wind speed V_{SW}. For the upper panel V_{SW} is set and κ_{rr} varied. The asymptotic limits on ξ for large and small κ_{rr} are indicated. For the lower panel κ_{rr} is set and V_{SW} varied.

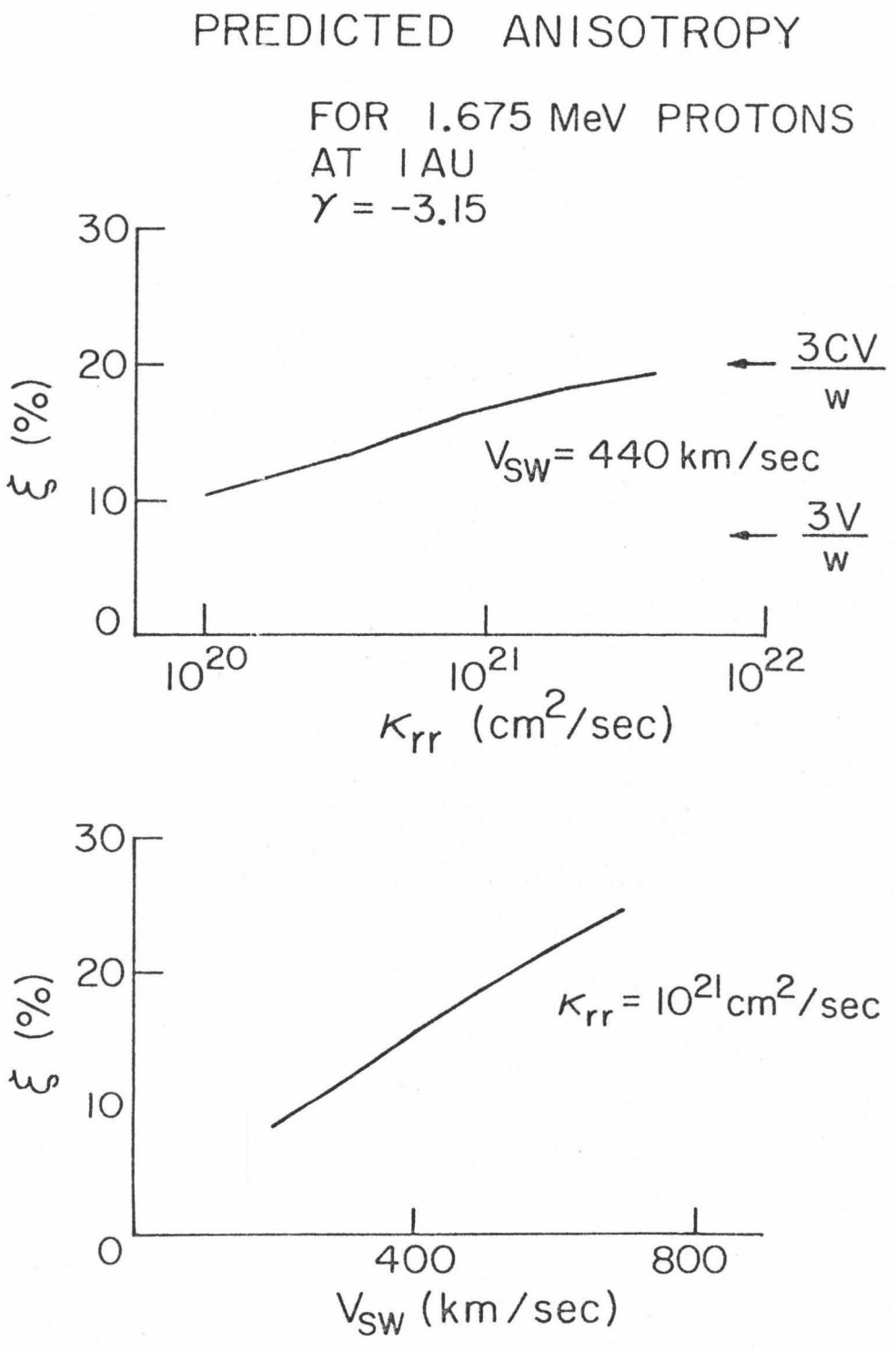
PREDICTED ANISOTROPY
FOR 1.675 MeV PROTONS
AT 1 AU
γ = -3.15
30
20
10
0
ξ (%)
3CV/w
V_SW = 440 km/sec
3V/w
10^20
10^21
10^22
κ_rr (cm^2/sec)
30
20
10
0
ξ (%)
κ_rr = 10^21 cm^2/sec
400
800
V_SW (km/sec)

APPENDIX D. DATA SET

Table D-1 lists the 6-hour periods used for the results of this study. The criteria used for their selection have been discussed in Chapter V. Each period is identified by yy ddd q , where yy is the year, ddd is the day number, and q is a number from 0 to 3 which specifies one of the four 6-hour periods of the day. In addition, the PLO rate in counts/second is given for each period.

TABLE D-1. Periods Used

TIME	PLO	TIME	PLO	TIME	PLO
72 285 0	0.0088	73 3 0	0.0044	73 53 3	0.0163
72 285 1	0.0150	73 3 1	0.0057	73 54 0	0.0157
72 285 2	0.0154	73 3 2	0.0072	73 92 0	0.0243
72 285 3	0.0153	73 3 3	0.0103	73 92 1	0.0206
72 294 0	0.0045	73 4 0	0.0163	73 92 2	0.0166
72 294 1	0.0048	73 4 1	0.0206	73 93 0	0.0096
72 294 3	0.0036	73 4 2	0.0313	73 93 1	0.0121
72 317 2	0.0232	73 4 3	0.0332	73 93 2	0.0122
72 317 3	0.0205	73 5 0	0.0265	73 93 3	0.0089
72 322 2	0.0031	73 5 1	0.0189	73 94 0	0.0057
72 342 2	0.0044	73 5 2	0.0139	73 94 1	0.0039
72 344 0	0.0031	73 5 3	0.0137	73 94 3	0.0061
72 345 1	0.0039	73 6 0	0.0115	73 95 0	0.0052
72 345 3	0.0051	73 6 1	0.0121	73 95 1	0.0072
72 346 0	0.0067	73 6 2	0.0224	73 117 0	0.0079
72 346 1	0.0151	73 6 3	0.0339	73 117 2	0.0033
72 346 2	0.0059	73 7 0	0.0547	73 117 3	0.0042
72 346 3	0.0054	73 7 1	0.0892	73 128 1	0.1102
72 355 1	0.0068	73 7 2	0.0968	73 128 2	0.0951
72 355 2	0.0058	73 7 3	0.0623	73 128 3	0.0781
72 355 3	0.0043	73 8 0	0.0678	73 129 0	0.0688
72 356 0	0.0037	73 19 3	0.0051	73 129 1	0.0680
72 356 1	0.0040	73 20 0	0.0056	73 129 3	0.2141
72 356 2	0.0049	73 20 1	0.0102	73 130 0	0.1677
72 356 3	0.0051	73 20 2	0.0052	73 130 1	0.1089
72 357 0	0.0041	73 20 3	0.0070	73 130 2	0.0747
72 357 1	0.0057	73 31 0	0.0036	73 130 3	0.0535
72 357 2	0.0086	73 31 1	0.0072	73 131 0	0.0611
72 357 3	0.0054	73 31 2	0.0171	73 131 1	0.0686
72 359 2	0.0040	73 31 3	0.0197	73 131 3	0.0623
72 359 3	0.0100	73 32 0	0.0274	73 132 0	0.0742
72 360 0	0.0085	73 32 1	0.0172	73 132 1	0.0920
72 360 1	0.0082	73 32 2	0.0093	73 132 2	0.1350
72 360 2	0.0298	73 32 3	0.0190	73 133 0	0.2553
72 360 3	0.0234	73 33 0	0.0155	73 133 1	0.2424
72 361 0	0.0174	73 33 1	0.0307	73 133 2	0.1604
72 361 1	0.0140	73 33 2	0.0344	73 141 0	0.1482
72 361 2	0.0143	73 53 0	0.0686	73 141 2	0.0261
73 2 2	0.0031	73 53 1	0.0518	73 141 3	0.0165
73 2 3	0.0052	73 53 2	0.0236	73 143 3	0.0277

TABLE D-1. Periods Used (continued)

TIME	PLO	TIME	PLO	TIME	PLO
73 144 0	0.0312	73 221 0	0.0291	73 248 1	0.0281
73 144 1	0.0238	73 221 1	0.0266	73 256 1	0.2961
73 144 3	0.0235	73 221 2	0.0184	73 256 2	0.2774
73 145 0	0.0062	73 221 3	0.0186	73 257 2	0.2828
73 145 1	0.0081	73 222 0	0.0202	73 257 3	0.2433
73 145 2	0.0076	73 222 2	0.0179	73 258 0	0.1793
73 145 3	0.0071	73 222 3	0.0151	73 258 1	0.1417
73 146 0	0.0085	73 223 0	0.0162	73 258 2	0.0922
73 146 1	0.0076	73 229 1	0.0175	73 258 3	0.0588
73 146 2	0.0121	73 229 2	0.0136	73 259 0	0.0198
73 146 3	0.0204	73 229 3	0.0154	73 259 1	0.0079
73 157 0	0.0427	73 230 0	0.0125	73 259 2	0.0060
73 159 1	0.0254	73 230 2	0.0058	73 259 3	0.0059
73 159 2	0.0224	73 230 3	0.0033	73 260 0	0.0037
73 166 3	0.2044	73 231 0	0.0046	73 260 1	0.0033
73 167 0	0.0952	73 231 2	0.0034	73 260 2	0.0030
73 167 1	0.0690	73 233 2	0.0064	73 260 3	0.0050
73 167 3	0.0612	73 234 3	0.0066	73 267 1	0.0467
73 168 0	0.0476	73 235 0	0.0086	73 267 2	0.0289
73 168 1	0.0381	73 235 1	0.0126	73 267 3	0.0426
73 168 2	0.0486	73 235 2	0.0436	73 268 0	0.0484
73 168 3	0.0388	73 242 1	0.0350	73 268 1	0.0659
73 169 0	0.0214	73 242 2	0.0366	73 268 2	0.0413
73 169 1	0.0050	73 242 3	0.0380	73 268 3	0.0065
73 192 0	0.0210	73 243 0	0.0417	73 273 0	0.0587
73 192 1	0.0386	73 243 1	0.0377	73 273 1	0.0226
73 192 2	0.0553	73 243 2	0.0376	73 273 2	0.0223
73 192 3	0.0579	73 243 3	0.0407	73 280 0	0.1117
73 193 0	0.0710	73 244 0	0.0399	73 280 1	0.0767
73 193 1	0.0997	73 244 1	0.0342	73 280 2	0.0499
73 193 2	0.1209	73 244 2	0.0292	73 280 3	0.0362
73 193 3	0.1406	73 244 3	0.0293	73 281 0	0.0219
73 194 0	0.1538	73 245 0	0.0271	73 281 1	0.0177
73 196 1	0.0560	73 245 1	0.0255	73 281 2	0.0157
73 219 2	0.0331	73 245 2	0.0301	73 282 0	0.0084
73 219 3	0.0269	73 245 3	0.0177	73 282 1	0.0070
73 220 0	0.0237	73 247 0	0.0081	73 282 2	0.0091
73 220 1	0.0243	73 247 2	0.0049	73 282 3	0.0092
73 220 2	0.0366	73 247 3	0.0048	73 284 3	0.0052
73 220 3	0.0350	73 248 0	0.0062	73 295 0	0.0849

TABLE D-1. Periods Used (continued)

TIME	PLO	TIME	PLO	TIME	PLO
73 295 1	0.0487	73 323 1	0.0041	73 344 0	0.0350
73 295 2	0.0395	73 323 2	0.0073	73 344 1	0.0683
73 295 3	0.0411	73 323 3	0.0152	73 344 2	0.0735
73 296 0	0.0402	73 324 0	0.0137	73 344 3	0.0968
73 296 1	0.0304	73 329 2	0.2179	73 345 0	0.1391
73 296 2	0.0173	73 331 1	0.0525	73 346 1	0.0072
73 297 0	0.0163	73 331 3	0.0500	73 346 2	0.0100
73 297 1	0.0038	73 332 0	0.0450	73 346 3	0.0077
73 297 2	0.0100	73 332 1	0.0534	73 347 0	0.0082
73 297 3	0.0336	73 332 2	0.0611	73 347 1	0.0125
73 298 0	0.0268	73 332 3	0.0648	73 347 2	0.0147
73 298 3	0.1091	73 333 0	0.0736	73 347 3	0.0156
73 299 0	0.0960	73 333 1	0.0642	73 348 0	0.0120
73 304 3	0.0136	73 333 2	0.0711	73 348 1	0.0138
73 305 0	0.0131	73 335 1	0.0080	73 348 2	0.0140
73 305 1	0.0109	73 335 2	0.0074	73 356 3	0.0041
73 305 2	0.0112	73 335 3	0.0089	73 357 0	0.0055
73 305 3	0.0080	73 336 1	0.0134	73 357 3	0.0108
73 317 0	0.0067	73 336 2	0.0131	73 358 0	0.0066
73 317 1	0.0123	73 336 3	0.0154	73 358 1	0.0071
73 317 2	0.0051	73 342 2	0.1328	73 358 2	0.0048
73 322 0	0.0032	73 342 3	0.0804	73 358 3	0.0031
73 322 1	0.0091	73 343 0	0.0402	73 359 0	0.0042
73 322 2	0.0073	73 343 1	0.0336	73 359 1	0.0049
73 322 3	0.0045	73 343 2	0.0359	73 360 0	0.0034
73 323 0	0.0032	73 343 3	0.0264		

REFERENCES

Allum, F. R., R. A. R. Palmeira, K. G. McCracken, and U. R. Rao, "Cosmic Ray Anisotropies Observed Late in the Decay Phase of Solar Flare Events," Solar Physics, 38, 227, 1974.

Anderson, K. A., "Electrons and Protons in Long-Lived Streams of Energetic Solar Particles," Solar Physics, 6, 111, 1969.

Balogh, A., S. Webb, and M. A. Forman, "Higher Order Compton-Getting Anisotropies," Planet. Space Sci., 21, 1802, 1973.

Behannon, K. W., "Mapping the Earth's Bow Shock and Magnetic Tail by Explorer 33," J. Geophys. Res., 73, 907, 1968.

Birmingham, T. J. and F. C. Jones, "Cosmic Ray Diffusion -- Report of the Workshop in Cosmic Ray Diffusion Theory," NASA TN D-7873, 1975.

Bryant, D. A., T. L. Cline, U. D. Desai, and F. B. McDonald, "Continual Acceleration of Solar Protons in the MeV Range," Phys. Rev. Lett., 14, 481, 1965.

Chapman, S. and J. Bartels, Geomagnetism, Oxford University Press, London, 1940.

Fan, C. Y., M. Pick, R. Pyle, J. A. Simpson, and D. R. Smith, "Protons Associated with Centers of Solar Activity and Their Propagation in Interplanetary Magnetic Field Regions Corotating with the Sun," J. Geophys. Res., 73, 1555, 1968.

Fisk, L. A., "On the Acceleration of Energetic Particles in the Interplanetary Medium," GSFC Preprint X-660-76-25, 1976.

Fisk, L. A., M. L. Goldstein, A. J. Klimas, and G. Sandri, "The Fokker-Planck Coefficient for Pitch-Angle Scattering of Cosmic Rays," Ap. J., 190, 417, 1974.

Forman, M. A., "The Compton-Getting Effect for Cosmic-Ray Particles and Photons and the Lorentz-Invariance of Distribution Functions," Planet. Space Sci., 18, 25, 1970.

Forman, M. A. and L. J. Gleeson, "Cosmic-Ray Streaming and Anisotropies, Astrophysics and Space Sciences, 32, 77, 1975.

Garrard, T. L., "Caltech Energetic Particles Experiments on IMP's H & J," Space Radiation Laboratory Internal Report #50, Calif. Inst. of Technology, 1974.

Gold, R. E. and E. C. Roelof, "Propagation of Relativistic Jovian Electrons to Pioneers 10 and 11 via Solar Wind Stream-Stream Interaction Regions," JHU/APL Preprint 76-08, 1976.

Hartman, S., "Geometrical Factors for IMP-H," Space Radiation Laboratory Internal Report #45, Calif. Inst. of Technology, 1973.

Hovestadt, D. and M. Scholer, "Radiation Belt Produced Energetic Hydrogen in Interplanetary Space," to be published in J. Geophys. Res., 1976.

Hurford, G. J., "Observations of Hydrogen and Helium Isotopes in Solar Cosmic Rays," Ph. D. Thesis, Calif. Inst. of Technology, 1974.

Hurford, G. J., R. A. Mewaldt, E. C. Stone, and R. E. Vogt, "The Energy Spectrum of 0.16 to 2 Mev Electrons during Solar Quiet Times," Ap. J., 192, 541, 1974.

Janni, J. F., "Calculations of Energy Loss, Range, Pathlength, Straggling, Multiple Scattering, and the Probability of Inelastic Nuclear Collisions for 0.1 - to 1000-MeV Protons," Technical Report No. AFWL-2R-65-150, 1966.

Jokipii, J. R., "Cosmic-Ray Propagation, 1, Charged Particles in a Random Magnetic Field," Ap. J., 146, 480, 1966.

Jokipii, J. R., "Propagation of Cosmic Rays in the Solar Wind," Reviews of Geophysics and Space Physics, 9, 27, 1971.

Jokipii, J. R. and E. N. Parker, "Stochastic Aspects of Magnetic Lines of Force with Application to Cosmic-Ray Propagation," Ap. J., 155, 777, 1969.

Kinsey, J. H., "Identification of a Highly Variable Component in Low-Energy Cosmic Rays at 1 AU," Phys. Rev. Lett., 24, 246, 1970.

Krimigis, S. M., E. C. Roelof, T. P. Armstrong, and J. A. Van Allen, "Low-Energy (> 0.3 MeV) Solar Particle Observations at Widely Separated Points (> 0.1 AU) during 1967," J. Geophys. Res., 76, 5921, 1971.

Krimigis, S. M., J. W. Kohl, and T. P. Armstrong, "The Magnetospheric Contribution to the Quiet-Time Low Energy Nucleon Spectrum in the Vicinity of Earth," Geophys. Res. Lett., 2, 457, 1975.

Lin, R. P., S. W. Kahler, and E. C. Roelof, "Solar Flare Injection and Propagation of Low-Energy Protons and Electrons in the Event of 7 - 9 July, 1966," Solar Physics, 4, 338, 1968.

Lupton, J. E. and E. C. Stone, "Measurements of Electron Detection Efficiencies in Solid State Detectors," Nucl. Instrum. Methods, 98, 189, 1972.

Lupton, J. E. and E. C. Stone, "Solar Flare Particle Propagation--Comparison of a New Analytic Solution with Spacecraft Measurements," J. Geophys. Res., 78, 1007, 1973.

McCracken, K. G. and U. R. Rao, "Solar Cosmic Ray Phenomena," Space Science Reviews, 11, 155, 1970.

McCracken, K. G., U. R. Rao, and N. F. Ness, "Interrelationship of Cosmic-Ray Anisotropies and the Interplanetary Magnetic Field," J. Geophys. Res., 73, 4159, 1968.

McCracken, K. G., U. R. Rao, R. P. Bukata, and E. P. Keath, "The Decay Phase of Solar Flare Events," Solar Physics, 18, 100, 1971.

McDonald, F. B. and U. D. Desai, "Recurrent Solar Cosmic Ray Events And Solar M Regions," J. Geophys. Res., 76, 808, 1971.

McDonald, F. B., B. J. Teegarden, J. H. Trainor, and T. T. von Rosenvinge, "The Interplanetary Acceleration of Energetic Nucleons," Ap. J., 203, L149, 1975.

McKibben, R. B., "Azimuthal Propagation of Low-Energy Solar-Flare Protons as Observed from Spacecraft Very Widely Separated in Solar Azimuth," J. Geophys. Res., 77, 3957, 1972.

McKibben, R. B., "Azimuthal Propagation of Low-Energy Solar Flare Protons; Interpretation of Observations," J. Geophys. Res., 78, 7184, 1973.

Mewaldt, R. A. and S. B. Vidor, "IMP H & J EIS Electronic Calibration," Space Radiation Laboratory Internal Report #60, Calif. Inst. of Technology, 1976.

Mewaldt, R. A., E. C. Stone, S. B. Vidor, and R. E. Vogt, "Isotopic Composition of the Anomalous Low Energy Cosmic Ray Nitrogen and Oxygen," Conf. Papers 14th Int. Cosmic Ray Conf. Munich, 1, 349, 1975a.

Mewaldt, R. A., E. C. Stone, and R. E. Vogt, "The Quiet Time Spectra of Low Energy Hydrogen and Helium Nuclei," Conf. Papers 14th Int. Cosmic Ray Conf. Munich, 2, 774, 1975b.

Northcliffe, L. C. and R. F. Schilling, "Range and Stopping Power Tables for Heavy Ions," Nuclear Data Tables, A7, 233, 1970.

Pesses, M. E. and E. T. Sarris, "On the Anisotropies of Interplanetary Low-Energy Proton Intensities," Geophys. Res. Lett., 2, 349, 1975.

Pesses, M. E., C. K. Goertz, J. A. Van Allen, E. T. Sarris, and S. M. Krimigis, "Energetic Proton Events Observed between 1 - 5 AU by Pioneer 11," Trans. Amer. Geophys. U., 57, 304, 1976.

Rao, U. R., K. G. McCracken, and R. P. Bukata, "Cosmic-Ray Propagation Processes, 2, The Energetic Storm-Particle Event," J. Geophys. Res., 72, 4325, 1967a.

Rao, U. R.,K. G. McCracken, and W. C. Bartley, "Cosmic-Ray Propagation Processes, 3, The Diurnal Anisotropy in the Vicinity of 10 MeV/Nucleon," J. Geophys. Res., 72, 4343, 1967b.

Rao, U. R., K. G. McCracken, F. R. Allum, R. A. R. Palmeira, W. C. Bartley, and J. Palmer, "Anisotropy Characteristics of Low Energy Cosmic Ray Population of Solar Origin," Solar Physics, 19, 209, 1971.

Roelof, E. C., "On the Measurement of Energetic Particle Flux Anisotropies with a Class of Spinning Detectors," J. Geophys. Res., 79, 1535, 1974.

Roelof, E. C. and S. M. Krimigis, "Analysis and Synthesis of Coronal and Interplanetary Energetic Particle, Plasma, and Magnetic Field Observations over Three Solar Rotations," J. Geophys. Res., 78, 5375, 1973.

Sentman, D. and D. Baker, "Determination of Integrated Pitch Angle Distributions by Deconvolving Pioneer 10 Angular Distribution Data," unpublished manuscript, 1974.

Wibberenz, G., "Interplanetary Magnetic Fields and the Propagation of Cosmic Rays," J. Geophys. Res., 40, 667, 1974.

Wolfe, J. H., "The Large-Scale Structure of the Solar Wind," Solar Wind, edited by P. J. Coleman, C. P. Sonett, and J. M. Wilcox, NASA SP-308, 170, 1972.

Zwickl, R. D. and W. R. Webber, "Poisson Limitations Imposed on the Cosmic-Ray Anisotropy Cosine Fit," Trans. Amer. Geophys. U., 56, 1164, 1974.